Towards a 2-Terminal $Cu_2Zn(Sn, Ge)S_4$-on-Si Tandem Solar Cell

Fredrik Arnesen Stulen

Thesis submitted for the degree of
Master in Materials Science and Nanotechnology
60 credits

Department of Physics
Faculty of mathematics and natural sciences

UNIVERSITY OF OSLO

Spring 2019

Towards a 2-Terminal $Cu_2Zn(Sn,Ge)S_4$-on-Si Tandem Solar Cell

Fredrik Arnesen Stulen

© 2019 Fredrik Arnesen Stulen

Towards a 2-Terminal $Cu_2Zn(Sn,Ge)S_4$-on-Si Tandem Solar Cell

http://www.duo.uio.no/

Printed: Reprosentralen, University of Oslo

Abstract

Towards a 2-Terminal $\mathbf{Cu_2Zn(Sn,Ge)S_4}$-on-Si Tandem Solar Cell

Tandem solar cells based on silicon (Si) as the bottom cells utilize well-established manufacturing processes for Si, while exceeding the Shockley-Queisser limit for single-junction solar cells. The pursuit to find an inexpensive, non-toxic, Si compatible and potentially high efficiency top cell have received tremendous amount of attention, where a wide range of absorber materials have been proposed and explored. Cu_2ZnSnS_4 (CZTS) is one such promising candidate for a top cell absorber material, containing only abundant and non-toxic elements. Moreover, its band gap of 1.5 eV can be engineered by incorporation of Ge to match the optimum band gap for a top cell in a Si-based tandem structure. In the first part of the work presented here, Ge incorporation and a band gap gradient have been investigated by secondary ion mass spectrometry (SIMS) and glow-discharge optical emission spectroscopy (GDOES). However, to monolithically integrate the CZTS absorber with the Si bottom cell, a processing step at temperatures above 500 °C is required. Impurities present in the CZTS top cell may cause severe degradation of the Si bottom cell if they diffuse into the Si layer during the CZTS processing. A thin diffusion barrier of TiN has been proposed, and in the second part of this work the TiN diffusion barrier is investigated and proven capable of suppressing the interdiffusion of impurities from CZTS into the Si bottom cell. In combination with Si employing tunnel oxide passivating contacts (TOPCon), the TiN diffusion barrier suppresses interdiffusion and the TOPCon offer gettering sites for Cu in the Si structure. This has been revealed through a systematic study using SIMS and deep-level transient spectroscopy (DLTS). Moreover, minority carrier lifetime measurements ensured appreciable minority carrier lifetimes in the Si bottom to proceed with device-making. Based on these results, one of the first "proof-of-concept" tandem solar cells of CZTS-on-Si have been demonstrated. A record-high V_{oc}, for CZTS-on-Si, of more than 800 mV is achieved, higher than that of each cell individually, providing a strong motivation for further studies and development of a CZTS-on-Si tandem solar cell.

Sammendrag

Mot en 2-Terminal $Cu_2Zn(Sn,Ge)S_4$-på-Si Tandem Solcelle

Tandem solceller basert på silisium (Si) som bunncelle benytter veletablert industri, og samtidig overgår Shockley-Queisser grensen for enkel-overgang solceller. Jakten på en billig, ikke-giftig, Si-kompatibel og potensielt høy effektivitets-topcelle har fått stor oppmerksomhet, der en rekke materialer har blitt foreslått og utforsket. Cu_2ZnSnS_4 (CZTS) er et slikt lovende toppcelle materiale som kun inneholder lett tilgjengelige og ikke-giftige grunnstoffer. Dessuten har den et båndgap på 1.5 eV som kan økes gjennom Gelegering av CZTS, slik at båndgapet blir optimalt for bruk som toppcelle i Si-baserte tandemstrukturer. Den første delen av dette arbeidet tar for seg Ge-legering og en båndgapsgradient har blitt undersøkt ved sekundærionemassespektrometri (SIMS) og glimutladning optisk emisjonsspektroskopi (GDOES). For å integrere CZTS cellen med en Si bunncelle i en monolittisk struktur, kreves behandling over 500 °C. CZTS inneholder grunstoffer som kan virke som skadelige urenheter i Si bunncellen. Disse urenhetene kan føre til kraftig nedgradering av Si bunncellen hvis de diffunderer inn i Si substratet som følge av CZTS behandlingen. En tynn diffusjonsbarriere av TiN har blitt foreslått, og den andre delen av dette arbeidet har undersøkt en slik TiN diffusjonsbarriere og påvist at den er i stand til å motvirke diffundering av urenheter fra CZTS inn i Si bunncellen. I kombinasjon med Si som innehar tunnelering oksid passiviserte kontakter (TOPCon), motvirker TiN diffusjonsbarrieren diffundering og TOPCon gir en getteringeffekt for Cu i Si strukturen. Dette har blitt påvist gjennom en systematisk studie der SIMS og dypnivå transientspektroskopi (DLTS) har blitt brukt. Målinger av levetid til minoritetsladningsbærerere i Si etter CZTS behandling, indikerer en svært god minoritetsladningsbærerlevetid for å lage tandem solceller. Basert på disse resultatene har en av de første CZTS-på-Si tandem solcellene blitt demonstrert. En rekordhøy V_{oc}, for CZTS-på-Si, på over 800 mV ble oppnådd. Dette er høyere enn for CZTS og TOPCon Si solcellene individuelt og gir en sterk motivasjon for videre forskning og utvikling av en CZTS-på-Si tandem solcelle.

Acknowledgements

First, I would like to thank my day-to-day supervisor, Sigbjørn Grini, for all the time you have taken to answer my questions, proof reading drafts and your guidance at the lab. Also, thank you for your patience when teaching me how to operate the SIMS. I would also like to express my greatest gratitude to my main supervisor, Assoc. Prof. Lasse Vines. Your vast knowledge has been essential for this thesis and an inspiration to do good science.

I was introduced to the field of semiconductor physics during my bachelor by the great Bengt Gunnar Svensson. Thank you for sharing your passion and expertise in the field. May you forever rest in peace.

This thesis would never been realized if it was not for the collaboration with the Uppsala University and the Technical University of Denmark (DTU). Firstly, thank you to Prof. Charlotte Platzer-Björkman, Nishant Saini and Sven Englund at Uppsala for the interesting week I got to spend with you at the Ångström Laboratory. Thank you for the SEM images and your help with the fabrication. Secondly, thank you to Alireza Hajijafarassar and Filipe Martinho at DTU for sample preparation and shipping, μ-PCD measurements and skype meetings. I find our collaboration very fruitful and believe it has led to great results that I am proud to be a part of.

Thank you Viktor Bobal, Christoph Seiffert and Halvor Dolva for maintaining the MiNaLab facilities, and teaching me several experimental techniques. Thanks to Dr. Heine Nygard Riise for traning in XRD, spectrophotometer, ALD and e-beam evaporation. Also, thank you to Erlend Hall, and IFE, for help and letting me use their facilities to conduct device testing.

A great thanks also goes to everyone at LENS for making these two years so motivating and fun. A special thank you to my fellow master students for creating such an inspiring environment. Especially thank you to Kjetil Karlsen and Torbjørn Østmoe for continuing playing table tennis with me, even though I always beat you.

I would also say thank you to all my friends for support and all the good times. To my family, thank you for all endless love and support throughout my whole life. Finally, thank you to my beloved Martine for proof reading and making me happy every single day. I love you!

Contents

Abstract i

Sammendrag ii

Acknowledgements iii

Contents v

1 Introduction 1

2 Theory 3

2.1 Crystalline Materials . . . 3
2.1.1 Crystal Defects . . . 4
2.1.2 Diffusion . . . 5
2.2 Semiconductor Physics . . . 8
2.2.1 Electronic Energy Bands . . . 9
2.2.2 Charge Carrier Generation . . . 11
2.2.3 Charge Carrier Concentration . . . 13
2.2.4 Recombination and Trapping . . . 16
2.3 pn-Junction . . . 21
2.4 Solar Cells . . . 23
2.4.1 Operational Principles and Spectral Response . . . 23
2.4.2 Tandem Solar Cells . . . 26
2.4.3 Tunnel Oxide Passivated Contacts . . . 28
2.5 $Cu_2Zn(Sn, Ge)S_4$ for Si Tandem Applications . . . 28

2.5.1 Rationale 29
2.5.2 Growth of Cu_2ZnSnS_4 Films 30
2.5.3 Band Gap Engineering by Ge/Sn ratio 32
2.5.4 Monolithic Tandem Solar Cell of CZTS-on-Si 32

3 Experimental Methods - Fabrication 35
3.1 TOPCon on Si Processing 35
3.2 Chemical Vapor Deposition 36
3.2.1 Atomic Layer Deposition 36
3.3 Chemical Bath Deposition 37
3.4 Physical Vapor Deposition 37
3.4.1 Thermal- and Electron Beam Evaporation 38
3.4.2 Sputtering Deposition 38

4 Experimental Methods - Characterization 41
4.1 Secondary Ion Mass Spectrometry 41
4.1.1 The Physics of Sputtering and Ionization 42
4.1.2 Analysis 43
4.1.3 Quantification 44
4.1.4 Instrumentation 45
4.2 X-Ray Diffraction 45
4.3 Glow-Discharge Optical Emission Spectroscopy 48
4.4 μ-Wave Detected Photoconductance Decay 49
4.5 Capacitance-Voltage Measurements 50
4.6 Deep-Level Transient Spectroscopy 51
4.6.1 Principle of Operation 51
4.6.2 Generation of the DLTS Spectrum 53
4.6.3 Data Extraction and Physical Interpretation 55
4.7 Scanning Electron Microscopy 56

5 Results and Discussion 59
5.1 SIMS and GDOES as Tools to Study Ge Gradient in CZTGS . 59

5.1.1 Sample Preparation 60
5.1.2 SIMS Results 60
5.1.3 GDOES Results 62
5.1.4 Discussion 65
5.2 Interdiffusion From CZTS Synthesis and its Impact on Device Performance 68
5.2.1 Post-Deposition Etching of CZTS and/or TiN 69
5.2.2 Si with TOPCon - Lifetime Measurements 70
5.2.3 Si with TOPCon - SIMS Results 71
5.2.4 Si without TOPCon - SIMS Results 75
5.2.5 Si without TOPCon - DLTS Results 78
5.3 Fabrication of Monolithic Tandem Solar Cells 82
5.3.1 Experimental Details 82
5.3.2 Optimization of the CZTS Deposition on Si 83
5.3.3 Morphology and Crystallinity 84
5.3.4 Device Characterization 85
5.3.5 Discussion 87

6 Summary **89**
6.1 Conclusion 89
6.2 Suggestions for Further Work and Improvements 90

Bibliography **93**

A Elements Detected with SIMS **101**

B CZTS Synthesis in Tandem Fabrication **102**

CHAPTER 1

Introduction

The rising electricity demand is causing great challenges for mankind. In terms of energy production, there is a severe need for renewable energy for a sustainable production. Due to the predicted growth of 1.7 billion people, the New Policies Scenario predicts the energy demand will increase by more than a quarter by 2040 [1]. In the period 2014-2016, CO_2 emissions stagnated. Nevertheless, a record emission of global energy-related CO_2 was reached in 2018 with a growth of 1.7 %. The past years have seen big price reductions in photovoltaics (PV) and the number of grid-connected solar systems grew by almost 30 % [2]. Silicon (Si) wafer-based technology accounts for more than 90 % of the total PV production. Due to its indirect band gap and low absorption, Si wafers require a thickness above 100 μm to absorb most of the sunlight. Thin films solar cells, such as Cu_2InGaS_4 (CIGS) and CdTe, have achieved efficiencies above 21 % [3] (close to Si solar cells), requiring only approximately 1 μm of material. However, the thin films mentioned above contain scarce, expensive and/or toxic elements. The Cu_2ZnSnS_4 (CZTS) thin film solar cell is therefore a promising alternative, as it consists of only earth-abundant and non-toxic elements. Further, it is a direct band gap material with excellent absorption and a band gap of 1.5 eV [4].

A considerable amount of research is being put into exceeding the efficiency limit of single-junction solar cells. A promising technology for this, simultaneously maintaining Si manufacturing technology, is tandem solar cells based on Si as the bottom cell. Here, CZTS is a potential candidate

to be integrated as a solar cell on top of Si. By alloying with germanium (Ge), $Cu_2ZnGe_xSn_{1-x}S_4$ (CZTGS), the band gap can be engineered to match the optimal band gap for a top cell in Si-based tandem solar cells. Hence, the first part of this thesis is investigating tools for studying Ge gradients in CZTGS.

Defects are always present in materials and may have severe effects on materials properties and device performance depending on type and placement in the device. The fabrication of tandem solar cells usually involves heat treatment(s) at relatively high temperatures. This may induce migration of atoms resulting in an introduction of impurities to unwanted locations inside the material. Therefore, the second part of this thesis was dedicated to study interdiffusion of detrimental impurities in CZTS-on-Si tandem structures, and their electrical activity and effect on device performance.

Full tandem devices were fabricated and characterized in terms of structure and electrical performance. Hence, the final part of this thesis is a "proof-of-concept" of CZTS as a compatible top cell in Si-based tandem solar cells.

CHAPTER 2

Theory

In this chapter, the theoretical background, which is a prerequisite for understanding the experimental methods and results, are presented. It starts off with an introduction of basic materials science and semiconductor physics, before introducing important principles and new concepts of solar cells. In the last section, one of the two solar cell materials studied in this thesis, Cu_2ZnSnS_4 (CZTS), is presented. It is assumed that the reader to some extent is familiar with silicon (Si) as a semiconductor and/or solar cell material. Thus, throughout this chapter, silicon will be used in examples when appropriate.

2.1 Crystalline Materials

This section is based on the books by Tilley [5], Kittel [6] and Campbell [7].

Crystalline solids have atoms arranged in a periodic manner. The atoms are bonded together by ionic-, metallic- or covalent bonds, where a balancing of attractive and repulsing forces determine the interatomic spacing. The periodicity of atoms make up a crystal structure. Solids with no periodicity at all are called amorphous, while polycrystalline solids have several regions of crystals with different direction called grains.

The periodicity in a crystal is defined by an infinite pattern of mathematical points making up the lattice, illustrated in Fig. 2.1a. Attached to each lattice point are identical groups of atoms (yet it may also just be one

single atom) called a basis (Fig. 2.1b). By choosing an arbitrary lattice point as origin, the position of any other lattice point is given by the translation vector

$$\mathbf{R} = u\mathbf{a} + v\mathbf{b} + w\mathbf{c}, \tag{2.1}$$

where **a**, **b** and **c** are basis vectors and u, v and w are integers. The basis vectors are chosen to be small and reveal the underlying symmetry of the lattice, and forms the unit cell. This is the smallest repeating unit sharing the symmetry of the crystal structure, with a spacing of a, b and c between cell edges and an angle between them of α, β and γ. Combinations of these lengths and angles build up 7 different lattices. Taking into account cubic units with lattice points in the center (body-center) and at the faces (face-center), 14 different lattices are possible. These lattices are called Bravais lattices, and in combination with a basis, all possible crystal structures are to be created.

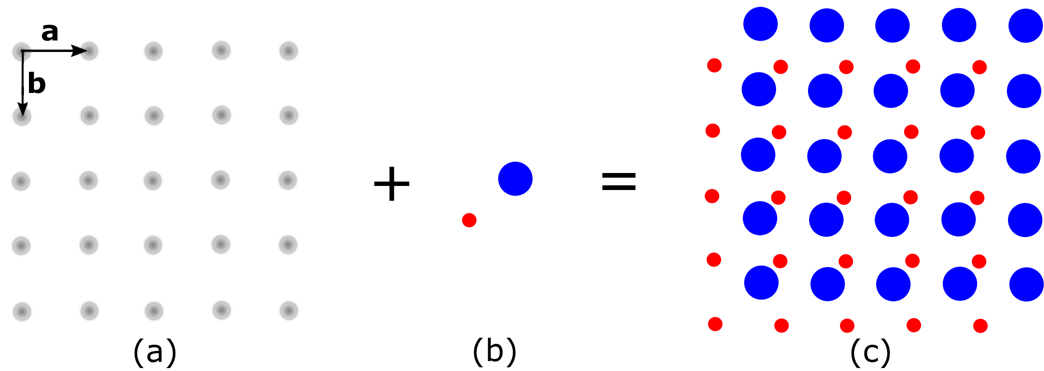

Figure 2.1: The crystal structure (c) is constructed of a basis (b) occupying every lattice point (a). Two basis vectors can be seen in (a).

2.1.1 Crystal Defects

All crystals contain defects, and these are detrimental for the material's properties. One fundamental type of defects is a site missing an atom. This is called a vacancy and is an example of a point defect which are defects with zero dimensionality. It is thermodynamically favourable for a crystal at a given temperature to contain a certain amount of vacancies, as this will

lower its Gibbs' free energy. The formation of a vacancy may induce the formation of other point defects, e.g. the host atom leaving its site takes a position in between lattice sites, referred to as self-interstitial. Vacancies and self-interstitials are examples of intrinsic defects and they are very likely to move around in the lattice, especially at high temperatures.

Extrinsic defects belong to a second type of point defects, which are extremely important in semiconductor technology. Here, an impurity atom will occur either at an interstitial site or a lattice site. Some impurities are unwanted and may cause severe device degradation (e.g. Cu, Fe and other metallic elements in Si), while others are intentionally introduced as dopants (e.g. B, P and As). In the latter case substitutional impurities (impurity occupying a lattice site) are introduced to alter the semiconductor's electrical conductivity. This process will be explicitly described when considering the physics of semiconductors. A schematic illustration of the different point defects are shown in Fig. 2.2.

Defects which extend in one dimension are called line defects, and the most common example is a dislocation, meaning an extra line of atoms is inserted between two other lines of atoms. Two-dimensional defects are called area defects, where one example is simply the boundary between grains in polycrystalline solids. Some defects also extend in all three directions called bulk defects, whereas the most common is a precipitate. Precipitates of Cu are often observed in Si due to the low solubility of Cu in a Si matrix.

2.1.2 Diffusion

After introducing impurities to a wafer, they will redistribute due to e.g. thermal processes. Diffusion is the net movement of material that occur near a concentration gradient as a result of random thermal motion. The migration tend to reduce the concentration gradient, meaning that impurities will move away from the concentration maximum. This phenomena is not only limited to semiconductors, as this is also used to describe e.g. heat transfer, motion of electron and gas transport. Solid-state diffusion can often be described by Fick's first law [8], where the net flux of material, J is given

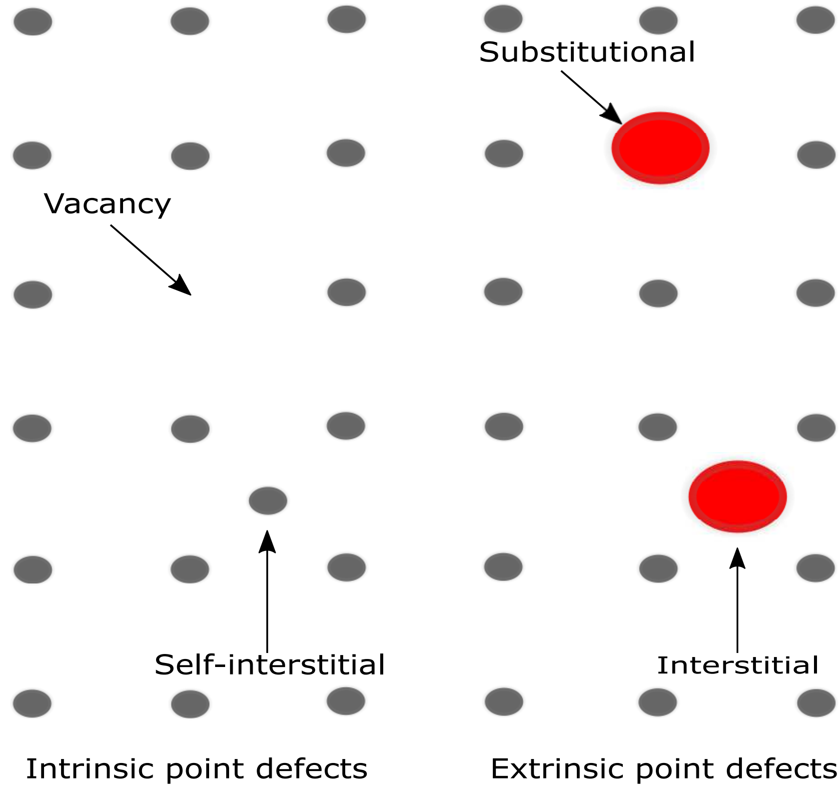

Figure 2.2: Illustration showing various point defects.

as

$$J = -D\frac{\partial C(x,t)}{\partial x}, \tag{2.2}$$

where D is the diffusion coefficient (also referred to as diffusivity) and C is concentration as a function of time and position. The diffusion coefficient is an important parameter that describe how easy the material transport in the media. It is temperature-dependent and often expressed by an Arrhenius equation

$$D = D_0 e^{-E_A/kT}, \tag{2.3}$$

where D_0 is a constant and called a pre-exponential factor (also referred to as frequency factor), k is the Boltzmann's constant, T is the absolute temperature and E_A is the activation energy. The activation energy is the energy required for an atom to overcome the potential set up by neighbouring lattice sites and make a transition (jump) to a new site in the lattice. The

probability that an atom will overcome the potential barrier is proportional to the exponential term in Eq. 2.3, meaning it increases with temperature.

The mechanisms of atomic movement depends on various factors such as size, diffusivity, chemical composition and crystal defects. A schematic overview of the different mechanisms behind atomic migration is presented in Fig. 2.3. Impurities with smaller atomic radius than the host atom tend

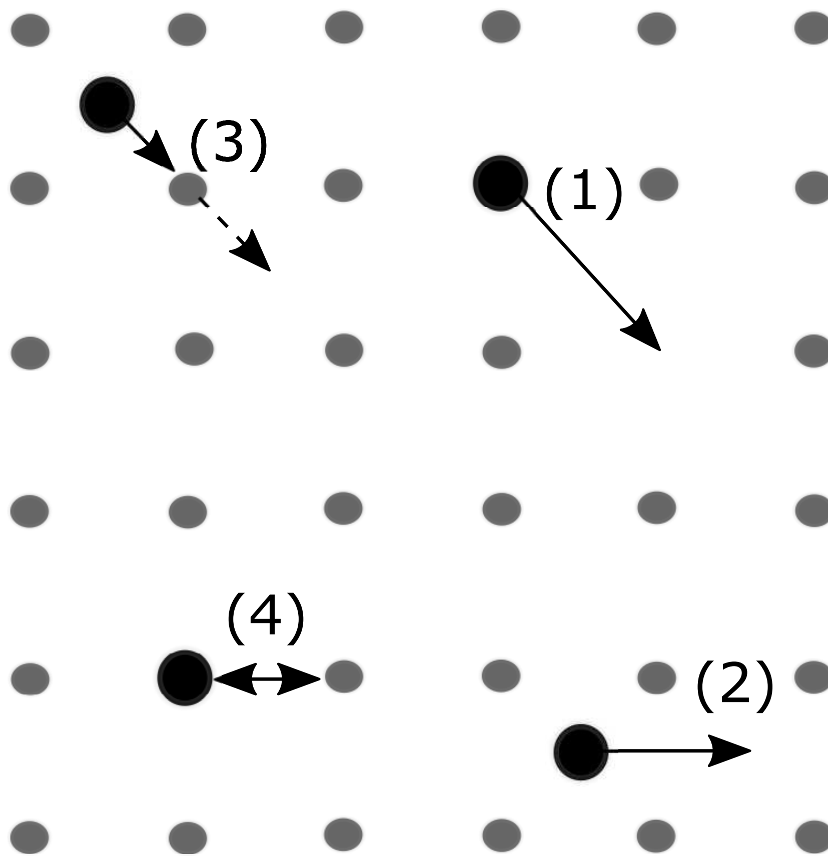

Figure 2.3: Schematic overview of some diffusion mechanisms: (1) vacancy mechanism, (2) interstitial mechanism, (3) interstitialcy and (4) direct exchange.

to diffuse in interstitial sites via an interstitial mechanism (2). This results in high diffusivity which only moderately decreases with decreasing temperature due to a low activation energy. When interstitial atoms are of similar size as the host atom, an indirect interstitial mechanism (3), also called interstitialcy mechanism, is often followed. Here a host atom become a self-interstitial simultaneously as an impurity jump to a substitutional site. Matrix and

substitutional atoms often tend to diffuse via a vacancy mechanism where the diffusing atom jump to a neighbouring vacancy (1). Neighbouring atoms may switch place in a direct exchange diffusion mechanism (4).

Defects have a significant impact on diffusion, e.g. vacancies mediates diffusion in solids. Impurities often tend to diffuse to defects such as dislocations and grain boundaries, which are acting as sinks. This principle, which is called gettering, is used in the industry to remove device-degrading impurities in semiconductor wafers. In materials containing very few impurities, e.g. high-purity monocrystalline semiconductors, fast diffusing materials often tend to migrate to surface as this is more thermodynamically stable. Grain boundaries have often much higher diffusivity than inside the grains and are important when evaluating diffusion in polycrystalline materials. Grain boundary diffusion is the dominating mechanism for many elements in CZTS (and other related materials) and is important in the consideration of grain boundary passivation by alkali diffusion, which have shown a positive effect on chalcogenides device performance [9, 10, 11, 12, 13, 14].

2.2 Semiconductor Physics

This section is based on the books by Kittel [6], Streetman [15] and Schroder [16].

Semiconductors are a group of materials with electrical conductivities intermediate between metals and insulators. Their electrical conductivity change significantly with temperature, optical excitation and impurity content (where the latter case will be explained in detail later). In elemental semiconductors (Si, Ge), each atom have four valence electrons, which are shared with neighbouring tetravalent atoms. It is this particular sharing of electrons which make up the covalent bonds between the atoms, whereas no free electrons should be present and contributing in electrical conductivity. However, this is an idealized situation similar to the behaviour of a perfect lattice at absolute zero temperature (0 Kelvin). Electrons can be thermally and/or optically excited out of a covalent bond and become a conducting electron.

2.2.1 Electronic Energy Bands

A single atom holds discrete energy levels, where some may be filled by electrons. When many atoms are brought together (e.g. in solids) a continuous band of energy levels will form and be separated by a forbidden interval called the band gap, E_g, which will be explained in detail later in this section.

In a solid, the presence of many atoms in a periodic lattice form a periodic potential, $U(\mathbf{r})$. The time-independent Schrödinger equation with a periodic potential can be expressed as

$$H\Psi(\mathbf{r}) = \left[-\frac{\hbar^2}{2m}\nabla^2 + U(\mathbf{r})\right]\Psi(\mathbf{r}) = E\Psi(\mathbf{r}), \tag{2.4}$$

where H is the Hamilton operator, $\Psi(\mathbf{r})$ is the electron wave function, E is the energy eigenvalue of the particular potential, $\hbar$ is Planck's constant (h) over 2π and m is the electron mass. The solution of Eq. 2.4 gives energy eigenvalues $E_n(\mathbf{k})$, where n is the band index ($n = 1, 2, 3, ...$), which will be discrete and vary with $\mathbf{k}$. A typical band structure is shown in Fig. 2.4, where the band gap (E_g) is highlighted. The band gap is the energy difference between the highest energy state in the highest occupied band at 0 K (valence band, E_v) and the lowest energy state in the lowest unoccupied band at 0 K (conduction band, E_c).

In order to yield electrical conduction, an energy $\geq E_g$ must be supplied to electrons in the valence band (VB) for them to be excited to the conduction band (CB). The magnitude of the band gap distinguish semiconductors from insulators. At 0 K, semiconductors have more or less the same structure as insulators, where the VB is filled and CB is empty. The band gap of semiconductors is in the range such that only a reasonable amount of thermal or optical energy is required to excite electrons across the band gap. In metals, the VB is either partly filled or overlaps with the CB meaning that many states with similar energies are available, hence the high electrical conductivity of metals.

The maximum and minimum of the band energies may or may not occur at the same $\mathbf{k}$, as seen in Fig. 2.5, which allows for a classification of dif-

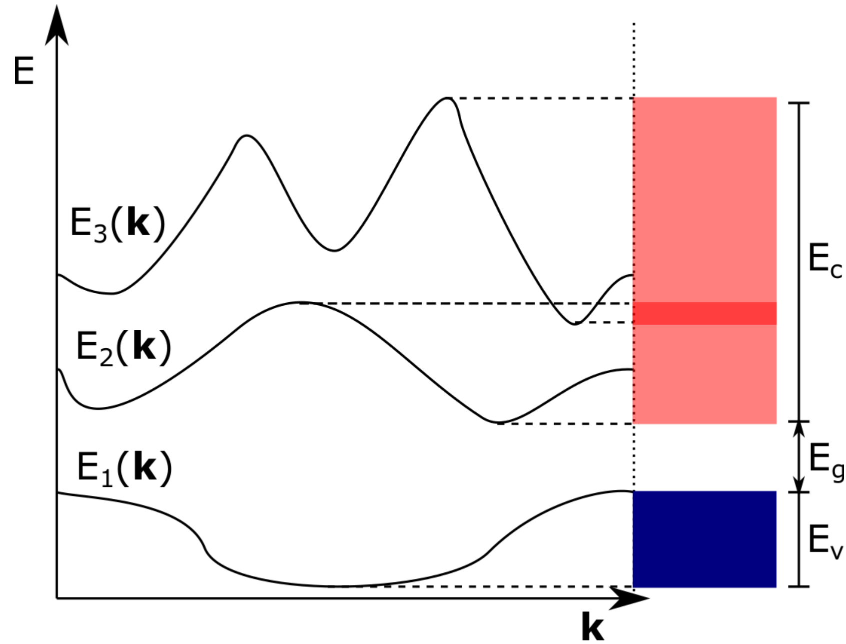

Figure 2.4: A typical band structure showing how the energy eigenvalues E_n vary with $\mathbf{k}$. On the right hand side is a simplified picture of energy bands, where variations in $\mathbf{k}$ are ignored.

ferent semiconductors. If the minimum of the VB and the maximum of the CB share the same wavevector, it is called a direct band gap material (e.g. CZTGS). In the case where the minimum and maximum occur at different $\mathbf{k}$, a direct transition between the two bands are not allowed and a change in momentum, $\Delta\mathbf{p} = \hbar\Delta\mathbf{k}$, is required in order for an excitation to take place. This momentum change can be provided by the creation of a phonon (lattice vibration) with the correct wavevector. Semiconductors where the excitations holds this intermediate transition are called indirect band gap materials (e.g. Si) and exhibit lower absorption coefficients than direct band gap materials. Hence, a thicker absorption layer is required for indirect band gap materials compared to direct band gap materials for solar cell devices, e.g. few hundred microns for Si compared to a few microns for CZTGS.

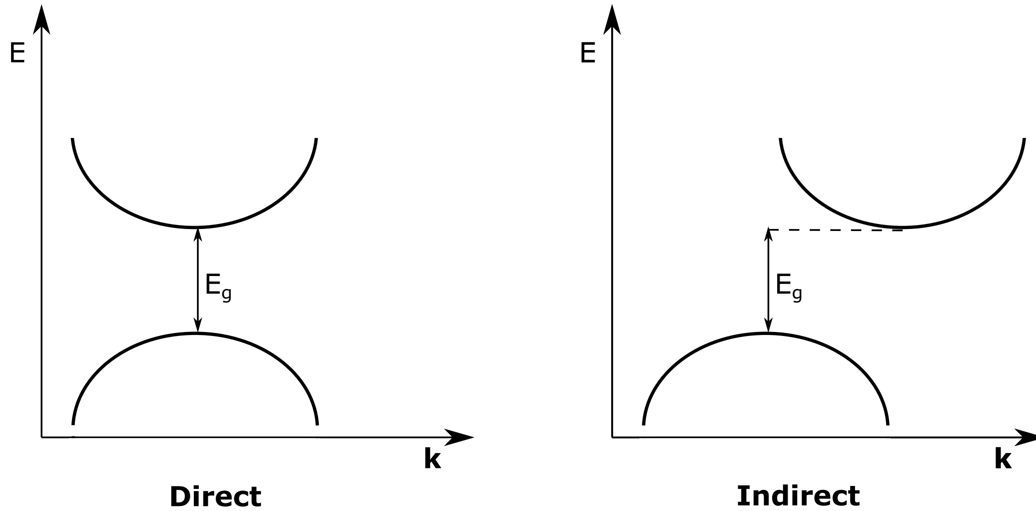

Figure 2.5: Simplified band structures illustrating the difference between direct- and indirect band gaps. In the $(E, \mathbf{k})$ relation on the right hand side, the CB minimum is located a step of $\Delta\mathbf{k}$ relative to the maximum of the VB.

2.2.2 Charge Carrier Generation

Charge carrier conduction in metals are often describes as a "sea" of electrons which are "free" to move under the influence of an electric field. The free electron model, often considered an oversimplification, holds surprisingly well when deriving important conduction properties. As described in the previous section, the number of conducting electrons increase with temperature in semiconductors due to thermal excitation. In addition, after an excitation of an electron we are left with an empty state in the VB called a hole, which also may contribute in the conduction process. It is called an electron-hole pair (EHP) when the CB electron and the hole are created by an excitation of a VB electron to the CB. Electrons/holes (charge carriers) in a crystal do not move completely free, but interact with the periodic potential of the lattice. This can be accounted for by altering the electron mass relative to the shape of energy bands from the dispersion relation between E and $\mathbf{k}$ which, in the

Γ point ($\mathbf{k} = 0$), can be approximated to be

$$E = \frac{\hbar^2}{2m}\mathbf{k}. \quad (2.5)$$

The effective mass of a charge carrier, with a given energy-wavevector relation, is then given by[1]

$$m^*_{\mathrm{n,h}} = \frac{\hbar^2}{d^2E/d\mathbf{k}^2}, \quad (2.6)$$

where the subscript denotes electron and hole, respectively. As seen in Eq. 2.6 the effective mass is inversely proportional to the curvature of the energy bands. Considering the valence band, the curvature bends downwards giving a negative second derivative meaning that holes will have a negative effective mass. This is a consequence of holes moving in opposite direction of that of electrons when exposed to an electric field.

A perfect semiconductor crystal containing no lattice defects or impurities is called an intrinsic semiconductor. Here the EHP generation is balanced, thus the electron concentration must equal the hole concentration and namely the intrinsic carrier concentration

$$n = p = n_i. \quad (2.7)$$

The generation of EHPs at a given temperature, in steady-state, must equally be balanced by a recombination rate, R_i of EHPs at the same rate as the generation, G_i, such that

$$R_i = G_i. \quad (2.8)$$

Recombination is a very important aspect of semiconductor physics, especially for solar cell applications and it will be described in detail in the next section.

Semiconductor properties may drastically change by introducing certain impurities into the crystal. One may introduce impurities intentionally in order to increase the equilibrium concentration of either electrons (n) or

[1]The effective mass is actually dependent on direction in the lattice, and therefore should be expressed as a tensor, but in this particular case we assume an isotropic lattice.

holes (p), thus changing the electrical conductivity. This process is called doping, where

$$n \neq p \neq n_i, \tag{2.9}$$

and the semiconductor is called an extrinsic semiconductor, which is either n-type (electrons dominate the conductivity) or p-type (holes dominate the conductivity). However, certain semiconductors are extrinsic as-grown, e.g. CZTS is p-type where the dopant is Cu vacancies (V_{Cu}). Impurities in semiconductors introduce new energy levels, often located inside the band gap. This may have severe impact on electrical properties depending on what kind of impurity. An n-type semiconductor is usually doped with impurities from column V of the periodic table, which will introduce an energy level close to the CB called a donor level, as illustrated in Fig. 2.6a. In the case of acceptor doping (column III), an energy level (acceptor level) close to VB is introduced (Fig. 2.6b), and the semiconductor will be p-type. Because of the small energy difference between the CB/VB and donor/acceptor level, only a small amount of energy is needed to excite electrons from the donor level/VB to the CB/acceptor level.

In doped semiconductors there will be one type of charge carriers dominating. The dominating carrier is referred to as majority carrier, while the minority carriers often are several of magnitudes lower in concentration. E.g. in an n-type semiconductor, electrons are the majority carriers and holes the minority carriers, and vice versa for a p-type semiconductor.

2.2.3 Charge Carrier Concentration

Electrons in a solid obey Fermi-Dirac statistics in how they occupy energy states. This model takes the indistinguishability and wave nature of electrons, and the Pauli exclusions principle into consideration. The probability of an electron occupying an energy state E at a given temperature T is given as

$$f(E) = \frac{1}{1 + e^{(E-E_F)/kT}}, \tag{2.10}$$

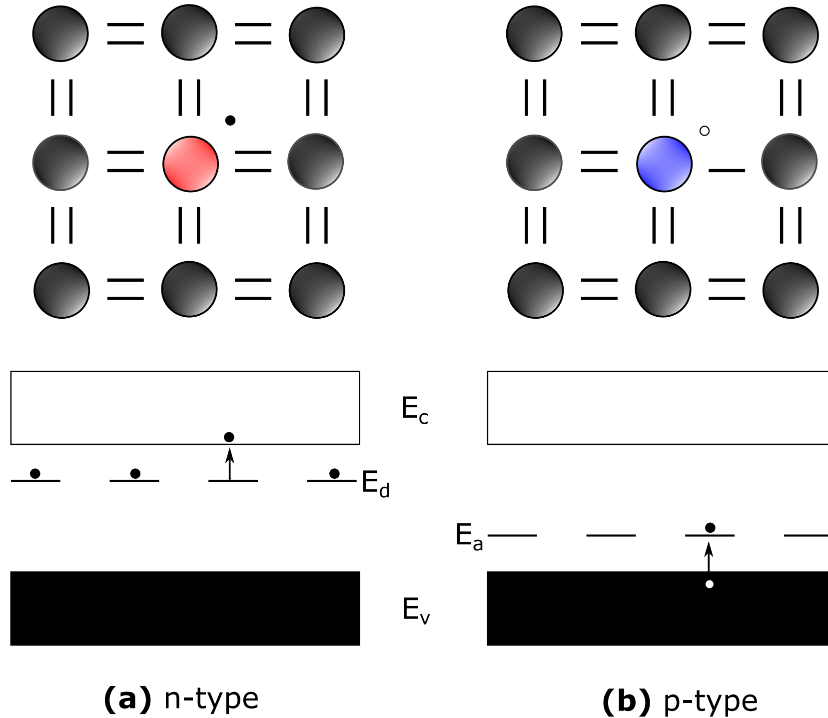

Figure 2.6: Upper part: Illustration of how n-type doping (red) introduce an electron (•), and p-type doping (blue) a hole (∘) by having fewer valence electrons than the host atom. Bottom part: Simplified band diagram showing how doping introduce new energy levels close to the band edges.

where k is the Boltzmann's constant and E_F is the Fermi level. The distribution function, $f(E)$ is illustrated in Fig. 2.7 for different temperatures. At the absolute zero temperature, the probability of an electron occupying an energy state is 1 up to the Fermi level energy and 0 for $E > E_F$. By increasing the temperature, the probability for an electron occupying a state above the Fermi level increase, as illustrated in Fig. 2.7. The probability of a hole filling a state is simply the probability that a state is **not** occupied by an electron: $[1 - f(E)]$. For an intrinsic semiconductor the Fermi level is found in the middle of the band gap, while in doped semiconductors the Fermi level lies closer to the band edge with the highest concentration of charge carriers (i.e. close to the CB for n-type, and close to the VB for p-type).

The Fermi-Dirac distribution function in combination with the density of states, $DOS(E)$, allows one to calculate the concentration of electrons in the

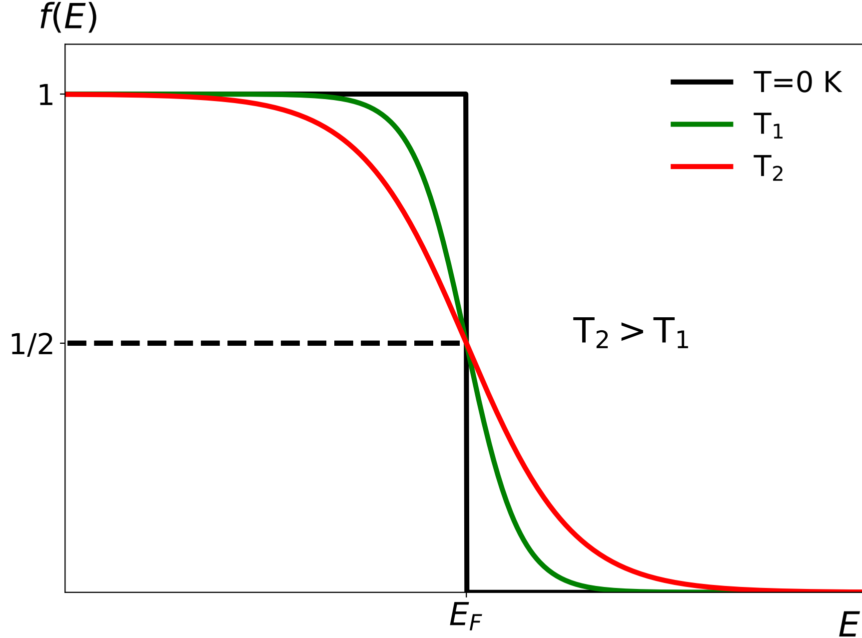

Figure 2.7: The Fermi-Dirac distribution function for different temperatures.

CB

$$n = \int_{E_c}^{\infty} f(E)DOS(E)dE, \tag{2.11}$$

while the concentration of holes in the valence band is given as

$$p = \int_{-\infty}^{E_v} [1 - f(E)]DOS(E)dE, \tag{2.12}$$

where E_c is the CB edge and E_v the VB edge. As very few electrons occupy states far from the CB edge, the density of states can be expressed as an effective density of states N_c, with all states located at the CB edge

$$N_c = 2\left(\frac{2\pi m_n^* kT}{h^2}\right)^{3/2}, \tag{2.13}$$

where m_n^* is the effective mass of electrons. The same applies for the effective density of states in the valence band E_v by applying the effective mass for

holes.

A reasonable assumption is to assume that the Fermi level is found several kT below the CB, then the distribution function close to E_c simplify to

$$f(E_c) \simeq e^{-(E_c - E_F)/kT}, \tag{2.14}$$

and the electron concentration in the CB is given as

$$n = N_c f(E_c) = N_c e^{-(E_c - E_F)/kT}. \tag{2.15}$$

A similar procedure for finding concentration of holes in the valence band lead to the expression

$$p = N_v[1 - f(E_v)] = N_v e^{-(E_F - E_v)/kT}. \tag{2.16}$$

When considering an intrinsic semiconductor, where Eq. 2.7 is true, the square of the intrinsic carrier concentration is found by combining Eq. 2.15 and 2.16

$$n_i^2 = np = N_v N_c e^{-(E_c - E_v)/kT} = N_v N_c e^{-Eg/kT}, \tag{2.17}$$

and is constant at a given temperature in a semiconductor, irrespective of the doping since Eq. 2.17 is not dependent of the Fermi level.

The constant relation between the product of the charge carrier concentrations and intrinsic carrier concentration in Eq. 2.17 is called the mass action law[2], and makes it easy to calculate charge carrier concentrations and Fermi level positions at a given temperature by only knowing the doping concentration, N_a if acceptor doping (p-type) or N_d if doping with donors (n-type).

2.2.4 Recombination and Trapping

In semiconductors, the process of recombination causes a loss of charge carriers. Recombination is an event where an electron falls to a lower energy state causing a decrease of mobile carriers, and takes place at a rate R. The

[2] In electronics, not to be confused for the mass action law in chemistry.

mechanism behind this recombination can be distinguished into unavoidable processes, due to physical processes in intrinsic materials, and avoidable processes caused by an imperfect crystal. Spontaneous emission of photons as a result of an electron directly relaxing from the CB to the VB is called radiative recombination (Fig. 2.8a), and is one of two unavoidable processes. The second one is called Auger recombination and takes place when an electron collides with another electron, and then falls down to the VB (Fig. 2.8c).

Avoidable processes are the most important in semiconductors as this is something that can be minimized by engineering. The most common process is called Shockley-Read-Hall recombination where an EHP recombine via a deep-level state, localized near the middle of the band gap, as illustrated in Fig. 2.8b. A deep-level state is characterized by its energy level E_T and its recombination rate is dependent on the concentration of trapping impurities N_T and capture cross section $\sigma_{\mathrm{n,p}}$. Deep-level states with its characteristics and thermodynamics will be explained in more detail later in this section.

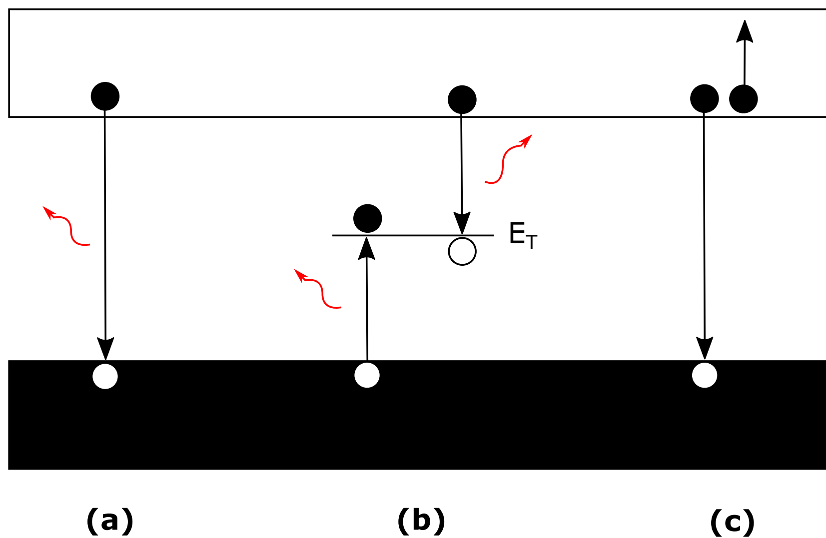

Figure 2.8: Schematic overview of the different recombination processes: (a) Radiative, (b) Shocley-Read-Hall and (c) Auger.

The average time a minority charge carrier spends in an excited state,

after generation, before recombining is defined as

$$\tau \equiv \frac{\Delta n}{R}, \tag{2.18}$$

where Δn is the excess carrier concentration, and is called the minority carrier lifetime. The total minority carrier lifetime, which is typically the one experimentally measured, is the effective minority carrier lifetime because it is a combination of the surface carrier lifetime τ_{sur}, and bulk carrier lifetime τ_{bulk}

$$\frac{1}{\tau_{eff}} = \frac{1}{\tau_{sur}} + \frac{1}{\tau_{bulk}}. \tag{2.19}$$

In semiconductors, and all crystalline materials in general, defects are more likely to occur at surfaces and in grain boundaries (if polycrystalline material). The surface recombination velocity S_{RV}, represents the recombination at the surface, and much effort is put into reducing this, e.g. by passivating dangling bonds on the surface. Another approach is to create a back surface field preventing minority carriers to move towards the surface by higher doped areas close to surfaces/interfaces.

The bulk carrier lifetime in Eq. 2.19 is given as

$$\frac{1}{\tau_{bulk}} = \frac{1}{\tau_{rad}} + \frac{1}{\tau_{Aug}} + \frac{1}{\tau_{SRH}}, \tag{2.20}$$

where τ_{rad}, τ_{Aug} and τ_{SRH} represent the carrier lifetime from radiative, Auger and Shockley-Read-Hall recombination, respectively. The total bulk carrier lifetime is limited by the recombination process with the shortest carrier lifetime and is injection dependent. Minority carrier lifetime is an important property in terms of semiconductor device performance and in defect characterization of semiconductors as carrier lifetime measurements in principle do not have a detection limit when it comes to detecting defects reducing the carrier lifetime.

Deep-Level States in the Band Gap

This section describes the fundamental theory behind deep-level transient spectroscopy, and follows the approach of chapter 7 and 8 in the book from Blood and Orton [17].

As mentioned earlier, crystal defects described in Sec 2.1.1 might introduce energy levels inside the band gap. The levels may be localized states (point defects) or more band-like states which may originate from extended defects (e.g. dislocations, stacking faults or precipitates). Deep-level states may behave as a generation/recombination center (as illustrated in Fig. 2.8b) or as traps. In the latter case, charge carriers are captured in an energy state E_T and re-emitted to the same energy band. The four processes describing the dynamic electronic behaviour of a trap with energy position $(E_c - E_T)$ and concentration N_T is illustrated in Fig. 2.9. The capture rate of electrons c_n can be defined as

$$c_n = n\sigma_n v_n^{th}, \tag{2.21}$$

where σ_n is the capture cross section for an electron and the thermal velocity of electron, v_n^{th} is given as

$$v_n^{th} = \sqrt{\frac{3kT}{m_n^*}}. \tag{2.22}$$

The emission rate of electrons e_n is temperature and Fermi level dependent and can be given as

$$\begin{aligned} e_n &= c_n e^{-(E_c - E_T)/kT} = n\sigma_n v_n^{th} e^{-(E_F - E_T)/kT} \\ &= \sigma_n v_n^{th} N_c e^{-(E_c - E_T)/kT}, \end{aligned} \tag{2.23}$$

where Eq. 2.15 has been substituted for the electron concentration in the conduction band (n) in the last step. A similar approach can be followed to find the capture and emission rates of holes. The defect signatures, $\sigma_{n,p}$ and $(E_c - E_T)/(E_T - E_v)$, can be found from Eq. 2.23 if the emission rate is calculated for several temperatures. The activation energy required to excite an electron from the trap state to the conduction band can be related to the

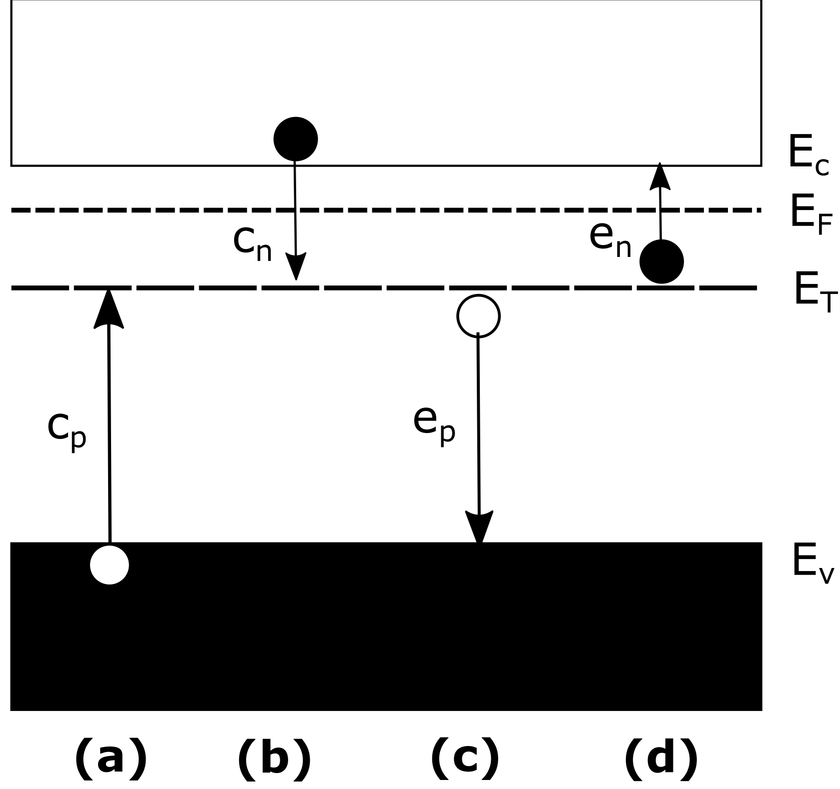

Figure 2.9: Schematic overview of the different capture and emission processes possible between an trap with energy level E_T and the energy bands: (a) Capture of hole from the valence band, (b) Capture of electron from the conduction band, (c) Emission of hole from the trap to the valence band and (d) Emission of electron from trap to the conduction band.

Gibbs free energy, hence the emission rate can be expressed as

$$\begin{aligned} e_n &= \sigma_n v_n^{th} N_c e^{-\Delta G/kT} = e^{-\Delta S/k} \sigma_n v_n^{th} N_c e^{-\Delta H/kT} \\ &= \sigma_{na} v_n^{th} N_c e^{-\Delta H/kT}, \end{aligned} \tag{2.24}$$

where $\Delta G = \Delta H - T\Delta S$ is Gibbs free energy with ΔH and ΔS being enthalpy and entropy variations respectively, and $\sigma_{na} = e^{-\Delta S/k}\sigma_n$ is the apparent capture cross section. In experimental measurements the apparent capture cross section and the enthalpy are the parameters found. By substituting Eq. 2.13 and Eq. 2.22 into 2.24 and extracting all temperature

independent factors into a constant β_n, one can obtain

$$\ln\left(\frac{e_n}{T^2}\right) = -\frac{\Delta H}{kT} + \ln(\beta_n \sigma_{na}), \tag{2.25}$$

where $\beta_n T^2 = v_n^{th} N_c$. A straight line is generated if plotting $\ln(e_n/T^2)$ vs. T^{-1}. From such an Arrhenius plot ΔH can be found from the slope of the line and σ_{na} as the intersect between an extrapolated line and the $\ln(e_n/T^2)$-axis.

The physical interpretation of the measured activation energy and apparent capture cross section will be revisited in Sec. 4.6 where an experimental technique for determining these quantities, deep-level transient spectroscopy (DLTS), will be explained.

2.3 pn-Junction

This section is based on Chapter 5, dedicated to electrostatic analysis of junctions, in the book by Streetman [15].

In order to utilize the generation of EHPs into electrical energy, charge separation is required. There are various conditions in which charge separation could be realized, e.g. a gradient in the band gap or a heterojunction, but the most common way of obtaining charge separation is by doping different regions of the same semiconductor differently. In particular, a structure containing an interface between p-type and n-type layers is called a pn-junction. The pn-junction is a fundamental feature in many electronic devices such as rectifiers, amplifiers, solar cells and so on.

When the n-type and p-type layers are brought together, charge carriers start to diffuse across the junction as results of concentration gradients, similar to atoms as seen in Sec. 2.1.2. This leaves behind uncompensated donor and acceptor ions in a layer called the space charge region[3] (SCR). An electric field, E, directed from the positive charge (near the n side) to the negative charge (near the p side), opposite of the diffusion current, arise from the presence of the uncompensated ions. At equilibrium, no current flow across the junction because the drift and diffusion current balance each

[3]Other common names are transition region or depletion layer.

other, and yield for both types of carriers. For example, the hole current density at equilibrium should give

$$J_p = \underbrace{q\mu_p pE}_{\text{drift current}} - \underbrace{qD_p \nabla p}_{\text{diffusion current}} = 0, \tag{2.26}$$

where q is charge, μ_p is hole mobility and D_p is the diffusivity of holes. The electron current density is obtained by substituting p with n in Eq. 2.26 and has opposite sign of the diffusion current. This causes steps in both the VB and the CB called the contact potential of magnitude V_0, as illustrated in Fig. 2.10, which deplete the SCR of carriers.

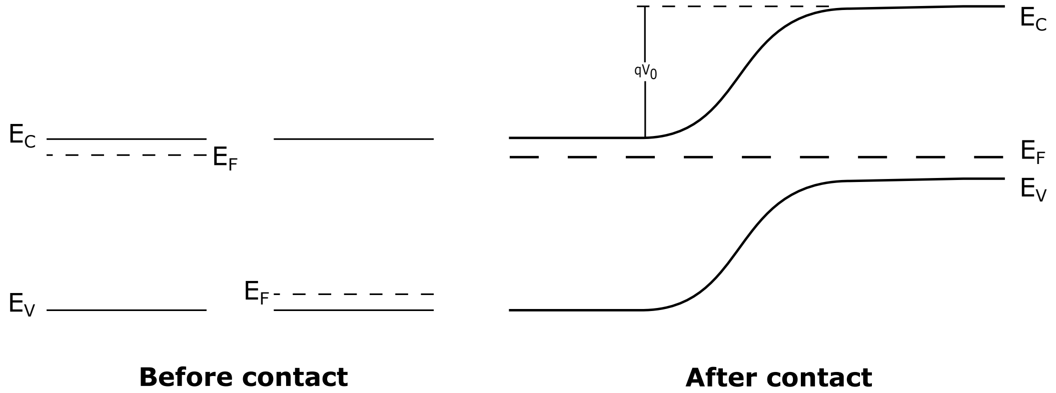

Figure 2.10: Band diagram showing the formation of the pn-junction. The Fermi levels will align after formation, causing the valence and conduction energy bands on the p-side to be qV_0 higher than on the n-side.

The potential barrier in Fig. 2.10 (qV_0) can be lowered or increased (depending on polarity) by applying an external bias. A forward bias (positive voltage) lower the potential barrier and increase the probability of a carrier to diffuse across the junction exponentially, as seen in the diode equation

$$J = J_0 \left(e^{qV/mkT} - 1 \right), \tag{2.27}$$

where $V = V_0 - V_j$ and V_j is the applied bias, J_0 is the leakage current density and m is the ideality factor which equals 1 for an ideal diode. The ideality factor is bigger than unity when generation and recombination in the junction and defects state in the band gap is present. In the next section,

the characteristics of Eq. 2.27 and its relation to operational principles of solar cells will be considered.

2.4 Solar Cells

This section is based on the chapters regarding solar cell characteristics and third-generetion solar cell concepts in the book by Nelson [18].

Solar cells are optoelectronic devices generating electrical energy from light. The photovoltaic effect was first documented almost 200 years ago, but it was the photoconductivity that excited the scientists at the time. Several decades later, the development of silicon electronics in the 1950s led to the discovery of pn-junctions showing really good rectifying properties and charge seperation in combination with photovoltaic behaviour. In 1954, the first silicon solar cell was reported by Chapin, Fuller and Pearson with 6 % efficiency [19]. However, due to high cost and lack of possibility for power generation in remote locations, these cells were not considered as possible energy sources.

Awareness of the need for alternative sources to electricity other than fossils, improvements of device efficiencies starting in the 90s and a significant price reduction, have made photovoltaics a hot topic. Today, silicon is still by far the most common solar cell material. However, with a maximum potential conversion efficiency of 29.4 % [20], much effort is put into developing new technologies and/or finding new materials to go beyond this limitation.

2.4.1 Operational Principles and Spectral Response

In order to achieve charge separation, solar cells consist of an asymmetric junction (described in Sec. 2.3). This results in a rectifying behaviour for most solar cells in the dark, expressed by Eq. 2.27. In order to express the current-voltage (JV) characteristics of a cell under illumination, we perform a superposition approximation expressing that the current is the sum of the

dark current (Eq. 2.27) and the short circuit current[4], such that

$$J = J_0 \left(e^{qV/mkT} - 1 \right) - J_{sc}, \tag{2.28}$$

where the maximum voltage is available at open circuit condition ($J = 0$) and given as

$$V_{oc} = \frac{mkT}{q} \ln \left(\frac{J_{sc}}{J_0} - 1 \right). \tag{2.29}$$

The short circuit current is found by integrating the incident spectral photon flux density, $\Phi_{in}(E)$ over all energies

$$J_{sc} = q \int_0^\infty \Phi_{in}(E) EQE(E) dE, \tag{2.30}$$

where $EQE(E)$ is the external quantum efficiency (EQE) and represent the probability that an incident photon will generate an EHP. In the ideal case where no light is reflected at the surface, every photon is absorbed and all generated carriers are collected, the EQE is

$$EQE(E) = \begin{cases} 1 & \text{when } E \geq E_g \\ 0 & \text{when } E < E_g, \end{cases} \tag{2.31}$$

and the short circuit current is simply given as

$$J_{sc,ideal} = \int_{E_g}^\infty \Phi_{in}(E) dE, \tag{2.32}$$

where we can see that the short circuit current is lower for high band gap materials. However, the case in Eq. 2.31 is not valid for real devices as the EQE will suffer from reflection, surface recombination, reduced absorption and more.

In order to understand the operation of solar cells, solar cell devices are often assumed to be equivalent to the electrical circuit in Fig. 2.11. Here, the resistances in the contacts are represented by the series resistance R_s, and leakage current resulting from shunting paths is included in the shunt

[4]Here we assume the photo generated current to equal the short circuit ($V = 0$) current.

resistance R_{sh}. By taking these parasitic resistances into consideration, the diode equation becomes

$$J = J_0 \left(e^{q(V - JR_s)/mkT} - 1 \right) - J_{sc} + \frac{V - JR_s}{R_{sh}}. \tag{2.33}$$

If we assume $R_s = 0$ and $R_{sh} = \infty$, which is known as the ideal 1-diode

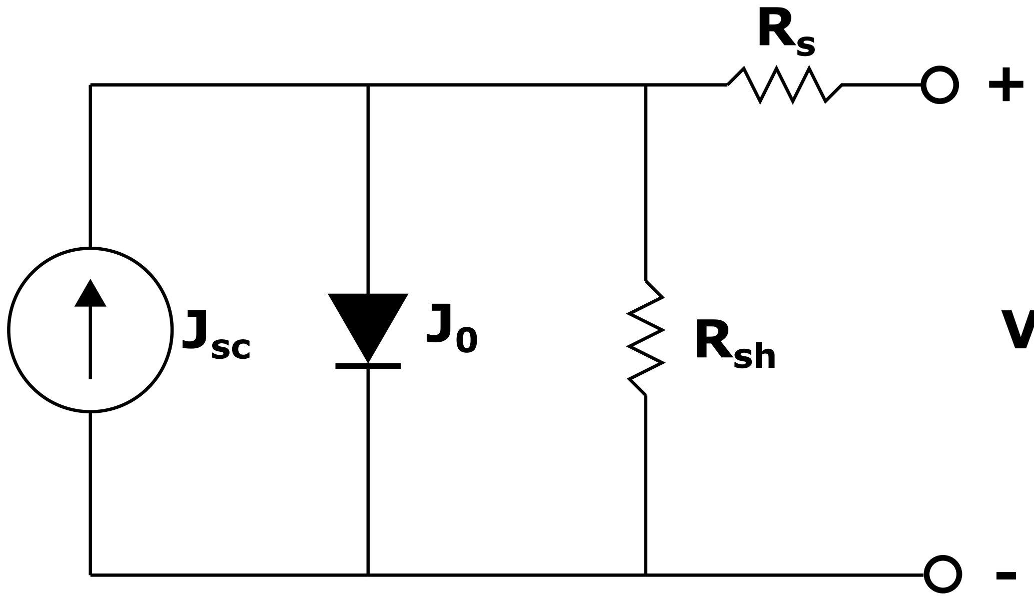

Figure 2.11: The electrical circuit of the 1-diode model often used to model the operational principle of a solar cell.

model, Eq. 2.33 reduces back to Eq. 2.28, and the resulting JV-characteristic is plotted in Fig. 2.12. The power density produced by a solar cell is

$$P = JV, \tag{2.34}$$

and reaches its highest value at the maximum power point (P_{mp}) where the voltage is V_{mp} and the current density is J_{mp}. The shape of the JV-curve is a good indication of how good the device is, where a square form is the ideal. The relation between an ideal (box-like shape) behaviour and the real curve is represented by the fill factor

$$FF = \frac{J_{mp} V_{mp}}{J_{sc} V_{oc}}, \tag{2.35}$$

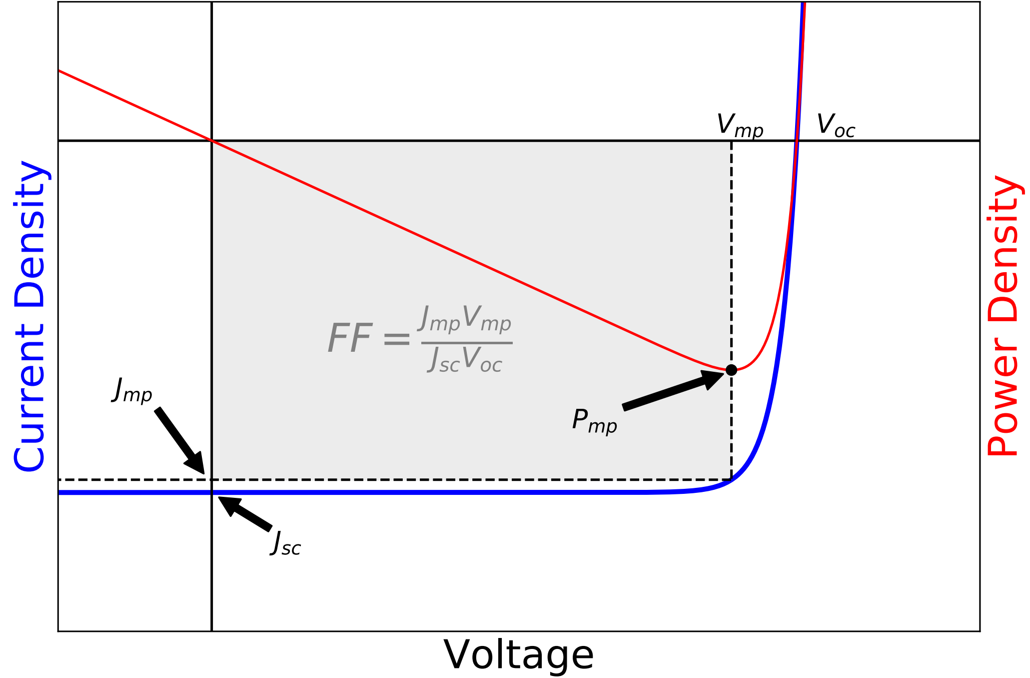

Figure 2.12: A typical JV characteristic for a solar cell under illumination also showing power density (red line). Important performance parameters are marked in the figure together with a shaded area illustrating the fill factor.

illustrated by the shaded area in Fig. 2.12. The maximum power conversion efficiency, η is given as the ratio between the power delivered at the maximum power point and the power of the incident photons, P_{in}. The efficiency is also related to the performance parameters defined in this section through

$$\eta = \frac{P_{mp}}{P_{in}} = \frac{J_{sc}V_{oc}FF}{P_{in}}. \tag{2.36}$$

2.4.2 Tandem Solar Cells

The maximum efficiency achievable for an optimum band gap single-junction solar cell, radiated by the standard solar spectrum, is $\sim 33\%$. This was calculated by Shockley and Queisser in 1961 [20], where an ideal solar cell model was assumed, known as the Shockley-Queisser limit. To obtain efficiencies close to the Shockley-Queisser limit for real devices, this require excellent

absorption, efficient charge separation and transport, and minimal parasitic resistance.

An approach to increase the absorption, thus improve the conversion efficiency, is stacking multiple pn-junctions with suitable band gaps in a structure making up a tandem solar cell. Such configuration allows the possibility to exceed the Shockley-Queisser limit. Placing the highest band gap cell on top allows it to absorb the most energetic photons, while the less energetic photons are transmitted to the next cell. The optimum power extraction is achieved by contacting the cells individually, allowing the different junctions to be optimized independent of each other. However, the fabrication of such a 4-terminal configuration (illustrated in Fig. 2.13a) is complex and require more processing step than monolithic integrated configuration. A more practical configuration is illustrated in Fig. 2.13b where contacts are attached only on the surface of the top cell and back of the bottom cell. In the latter

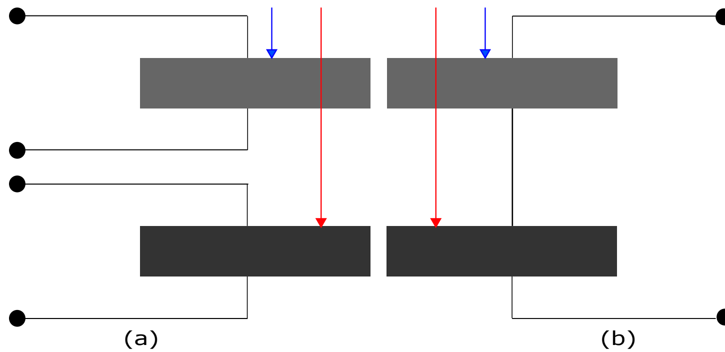

Figure 2.13: The 4-terminal configuration of a tandem solar cell is illustrated in (a), while the more simple 2-terminal design is shown in (b).

configuration, the current extraction is limited to the cell with the lowest J_{sc} and the voltages are additive. From theoretical calculations, an infinite stack of pn-junctions yield a maximum efficiency of 68% [21]. A tandem solar cell made up by two materials with optimum band gaps can theoretically reach a maximum efficiency of 42% [21]. In such a device based on Si as the bottom cell, the optimum band gap for the top cell is close to 1.7 eV.

2.4.3 Tunnel Oxide Passivated Contacts

The recent developments of single-junction Si solar cells have made surface and interface recombination the limiting factor. In order to overcome this, carrier-selective contacts have been purposed [22] and developed into an active research field.

A common strategy for reducing surface recombination is by forming a heavier doped layer, with equal conductivity, near the surface such that minority carriers are deflected by the surface field. Another much used approach is depositing a thin oxide layer on the front to passivate the Si surface while keeping a low density of interface trap states. In tunnel oxide passivated contacts (TOPCon) both procedures are employed. A highly-doped polycrystalline Si (poly-Si) layer at the surface(s) allows for extraction of majority carriers (here, majority refers to the conductivity of the poly-Si layer), while preventing minority carrier recombination due to field effect passivation. The n^+/p^+ poly-Si layer has a high density of trap states, therefore it is separated from the monocrystalline Si base by an ultra-thin ($\sim$ 1.5 nm) silicon dioxide (SiO_2) layer. The oxide layer stops minority carriers from reaching the poly-Si and prevents epitaxial regrowth during heat treatments [22]. The ultra-thin SiO_2 permits current flow by tunneling and/or, as suggested by Peibst et al. [23], through areas of reduced oxide thickness/pinholes formation.

Single-junction devices with a TOPCon configuration have been involved in several efficiency improvements for single-junction Si-based solar cells [24, 22, 25] with confirmed efficiencies upto 26.1 %. The TOPCon structure also has been successfully employed in Si-based tandem devices with GaAs [26] and perovskite [27] as the top cell.

2.5 $Cu_2Zn(Sn,Ge)S_4$ for Si Tandem Applications

This section introduces thin film chalcogenides as a potential top cell in silicon-based tandem solar cells. Materials properties, growth and some pre-

vious work will be addressed for a better understanding of the results to be presented.

2.5.1 Rationale

Si based technology are dominating the PV marked with its low price and established manufacturing. The efficiency of Si solar cells are approaching the Shockley-Queisser limit, and thus methods to exceed this limitation have developed into an active research field. Tandem solar cells with Si as the bottom cell are a strong candidate and have achieved efficiencies greater than that of single-junction Si with III-V and perovskites as top cells. However, these tandems are either cheap and/or unstable. Thin film semiconductors, e.g. CIGS and CdTe, are potential candidates for high-efficient Si-based tandem solar cells, but contain scarce and toxic elements.

The p-type semiconductor compound Cu_2ZnSnS_4 (CZTS) contains only abundant and non-toxic elements. This, and its direct band gap of 1.5 eV make it a promising absorber material in solar cell applications. Its band gap is within the optimal range as a single-junction solar cell, but not the optimal band gap as top cell with Si as the bottom cell. However, incorporation of Ge substituting Sn, $Cu_2ZnSn_{1-x}Ge_xS_4$ (CZTGS), will increase the band gap and eventually satisfy the optimal band gap for a top cell in a tandem device with Si. Kesterite absorbers also come in compounds where the chalcogen is substituted, i.e. selenide instead of sulphide (CZTSe). However, in this thesis we limit the scope to the pure sulphide compound (CZTS).

CZTGS crystallize in two different structures, kesterite and stannite, where the kesterite structure shown in Fig. 2.14 is the most stable from first-principle calculations [28] and neutron diffraction experiments [29]. Due to the similarity in cation size between Cu^+ and Zn^{2+}, they tend to switch place and change the crystal structure (stannite in the case of completely switching) or give a disordered kesterite structure. This Cu/Zn disorder has shown to give band gap fluctuations, thus causing voltage losses in CZTS solar cells [31].

The kesterite CZTGS holds several intruiging features for a top cell in

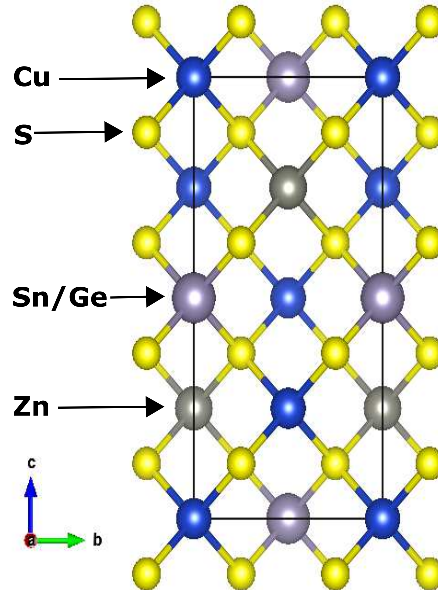

Figure 2.14: Illustration of the kesterite structure unit cell, the most stable crystal structure of CZTS. The tetragonal unit cell contains 16 atoms arranged by two zinc-blend unit cells stacked on top of each other. The illustration was made using VESTA software [30].

silicon-based tandem structures. In addition to containing mostly abundant elements, non-toxicity and band gap tuning, the ratio between the lattice constants of CZTGS and Si is close to unity. This close lattice-match makes it possible to grow CZTGS heteroepitaxially onto Si, which has also been proven experimentally [32, 33]. However, the deposition of CZTGS require one processing step above 500°C, as will be addressed in the next section. This may induce in-diffusion of metallic and chalcogen impurities to the bottom cell, which potentially will cause severe device degradation of the silicon cell.

2.5.2 Growth of Cu_2ZnSnS_4 Films

Deposition of CZTS are not limited to one technique. For example, CZTS have successfully been grown using sputtering [34], solid solution [35] and pulsed laser deposition [36]. One may also utilize different process approaches.

However, it is common, and believed to be the most successful route, to prepare kesterite thin films by a two-stage process. A precursor film is deposited onto a substrate at low temperature followed by an annealing step at high temperature. For example, the record CZTSSe cell was fabricated by a two-stage process, where the precursor was deposited by a hydrazine solution, which obtained a conversion efficiency of 12.6 % [37]. However, the CZTS films studied in this work are prepared from co-sputtering of precursors followed by a sulphurization step above 500°C to crystallize into solar grade material. Nevertheless, successful attempts of an one-stage process have been accomplished, yielding an efficiency of 5.5 % [38]. However, the substrate temperature during co-sputtering were held at 500°C, i.e. close to the sulphurization temperature.

Single-junction CZTS solar cell devices are usually deposited on molybdenum (Mo) coated soda-lime glass (SLG) substrates, where Mo is deposited as a back contact. The SLG substrate contains sodium (Na), which is considered a vital contributor to good device performance in CZTS. The incorporation of Na in chalcogenides passivate grain boundaries [39] and increase the FF, V_{oc} and hole density. Hence, the lack of Na when the Si bottom cell is used as the substrate may reduce the efficiency of the CZTS top cell.

The growth of solar grade CZTS comes with formation of several secondary phases. Various phases of copper sulphide are commonly found ranging from conductors to semiconductors with band gaps in the range of 1.2-2.53 eV [40]. Phases with band gaps lower than that of CZTS will decrease the V_{oc} of the solar cell, while conductors will act as shunting paths. Copper sulphides are unwanted in CZTS and often removed by surface treatments, e.g. KCN etching [41]. Furthermore, Cu-poor and Zn-rich conditions are preferred as this usually yield the best devices [42]. The Zn-rich condition results almost exclusively in formation of precipitates of ZnS, a semiconductor with a high band gap between 3.5-3.76 eV [43] causing an increase in series resistance. A very common secondary phase in single-junction CZTS is also MoS_2 located at the back contact interface, and formed during sulphurization. Nonetheless, a strength of CZTS and the related and more well known CIGS structure, is its resilience to degradation due to disorder, defects and secondary phases,

with appreciable device efficiencies even for highly distorted structures.

2.5.3 Band Gap Engineering by Ge/Sn ratio

Band gap grading is a potential route for increasing the efficiency of compound solar cells, which can be employed for CZTS. A compositional gradient towards the back creates a back surface field, thus reducing interface recombination. Band gap grading by S/Se substitution have been successfully employed in devices of $CZTS_{1-x}Se_x$ [44, 45]. The band gap of CZTSSe varies from 1.0 eV in the case of pure selenide, to 1.5 eV in the pure sulphide compound. For the implementation of a top cell in a silicon-based tandem structure, a band gap close to 1.7 eV is of interest. This can be accomplished for CZTS by incorporation of Ge substituting Sn, where the band band gap is found to vary non-linearly between 1.5 eV to 2.1 eV from first-principle calculations [46]. Chen *et al.* proved this experimentally in [47] by preparing five samples of $CZT_{1-x}G_xS$ with $x = 0$, 0.25, 0.5, 0.75 and 1. The band gaps were extracted from Tauc plots and found to follow the relation

$$E_g = 1.51 + 0.27x + 0.021x^2, \tag{2.37}$$

where x is the Ge/Sn ratio, $[Ge]/([Ge] + [Sn])$. According to these results the composition $CZT_{0.43}G_{0.57}S$ is optimal for integration in a silicon-based tandem solar cell.

2.5.4 Monolithic Tandem Solar Cell of CZTS-on-Si

In this work, monolithically integrated tandem devices of CZTS-on-Si have been investigated. Two-terminal tandem devices in a monolithic configuration are considered most feasible, of multi-junction configurations, in terms of industrial manufacturing. The silicon bottom cell preserve much of today's PV manufacturing technology, and a monolithic integration suppresses the number of processing steps. As previously addressed, the crystallization of chalcogenides usually require a high temperature annealing step, thus cause contamination and degradation of the Si bottom cell.

Here, a thin intermediate layer of titanium nitride (TiN) is investigated as a potential diffusion barrier to prevent in-diffusion of metallic and/or chalcogen impurities from the CZTS top cell. TiN, as a diffusion barrier, has previously been utilized for Cu metallization in integrated circuits [48, 49]. TiN is not the most effective material in stopping Cu diffusion, however, it has successfully been integrated as a intermediate layer in single-junction CZTSSe devices [50].

Substrates of Si with TOPCon have been used as bottom cells. This configuration offers high implied V_{oc} and devices with V_{oc} of 739 mV have been achieved [51]. The front poly-Si contact causes parasitic absorption of the blue light, hence a J_{sc} loss of 0.5 mA/cm^2 per 10 nm of polySi is expected [52]. However, this is not a limitation when applied in a tandem structure as the high energetic photons are absorbed in the top cell. In addition to excellent surface passivation and carrier selectivity, the TOPCon configuration offers gettering sites promising for preventing contamination from interdiffusion.

CHAPTER 3

Experimental Methods - Fabrication

This chapter describes the prosesses involved in the tandem device fabrication and is based on the books from Campbell [7], Kääriäinen *et al.* [53], and Majid and Bibi [54].

3.1 TOPCon on Si Processing

This section describes the processing of making tunnel oxide passivating contacts on Si. The physical principle of TOPCon is described in Sec. 2.4.3.

Double-side polished 100 mm diameter (100) n-type Cz-Si (1 Ωcm, 350 μm) wafers are used as silicon bottom cells. The ultra-thin ($\sim$ 1.5 nm) SiO_2 layer is wet-chemically grown. Here, the wafer is immersed into hot nitric acid (95 °C). Thereafter, amorphous Si (a-Si) is deposited on both sides by low-pressure chemical vapor deposition (LPCVD) at 650°C [1]. To obtain carrier selectivity opposite conductivities are required at the two interfaces, as explained in Sec. 2.4.3. The p-type layer at the back is formed by in-situ doping of B with B_2H_6 as precursor, while PH_3 is used as precursor for P doping to obtain n-type conductivity. Finally, the wafer undergoes a 20 minutes annealing at 850 °C. During this heat treatment the a-Si recrystallize to poly-Si and dopants are activated.

[1] A short description of this process can be found in the section to follow.

3.2 Chemical Vapor Deposition

Chemical vapor deposition (CVD) is a technique for deposition of thin films that rely on chemical reactions to take place at a substrate. Reactive gases are introduced into a quartz tube and decomposed by heat or plasma. The gas is then adsorbed on the surface of a heated substrate, where a surface chemical reaction are forming a solid thin film and by-products. The gas flow sweep away the by-products which then are removed as exhaust waste.

For improved film quality and uniform thickness, low-pressure CVD (LP-CVD) is used. Here, the pressure is lower ($\leq$ 1000 mTorr) causing less diffusion of gas to the substrate. In some cases, low temperatures are required to avoid melting, impurity diffusion, recrystallization etc. To enable this in lower temperature ambient, plasma is used to decompose the precursor gas. In plasma enhanced CVD (PECVD) systems the substrate temperature is well below 400 °C, allowing thin film deposition on substrates containing more volatile compounds.

3.2.1 Atomic Layer Deposition

Atomic layer deposition (ALD) is a subclass of CVD, where the film is grown monolayer by monolayer. ALD offers excellent uniformity, conformity and thickness control on the nanoscale. Here, the surface is subjected to atomic species rather than compounds. A first precursor gas is pulsed into the chamber saturating the substrate with a monolayer of the first reactant. The chamber is then purged with an inert gas, before introducing a second precursor gas into the chamber reacting with the first reactant and producing a monolayer of the desired film to be deposited. The second precursor gas is removed by a new inert gas purging. This cycle is repeated until the desired thickness is obtained.

The titanium nitride (TiN) diffusion barrier, in between the CZTS top cell and the TOPCon Si bottom cell, was deposited by PEALD at 500°C. Here, titanium tetrachloride ($TiCl_4$) is used as titanium source (first precursor), and ammonia (NH_3) is used as reducing agent (second precursor).

3.3 Chemical Bath Deposition

Chemical bath deposition (CBD) is a technique where thin films are deposited on a substrate in a precursor solution. The compound to be deposited is precipitated and condensed on the immersing substrate. Temperature, pH and concentration are carefully controlled in order to have nucleation at the substrate, and not at an arbitrary place in the solution.

CBD is commonly used to form the pn-junction in CZTS solar cells. Here, CdS is deposited as the n-type semiconductor making up a heterojunction with p-CZTS. The CBD solution is kept at 60 °C and the precursor is made up of 0.100 M thiourea (CH_4N_2S), 0.003 M cadmium acetate and 1.1 M ammonia. Sulphide ions are released by hydrolysis of thiourea in basic solution, and react with free cadmium ions to grow CdS. The growth mechanism involves (i) ion by ion growth and (ii) cluster by cluster growth. The beaker holding the samples were kept in the bath for 8 minutes, and stirred every minute. According to the colour of the film, and the baseline established at the Ångström laboratory, this yield a thickness of 50 nm.

3.4 Physical Vapor Deposition

Physical vapor deposition (PVD) is a technique where thin films are deposited by condensing the material to be deposited (charge), which first is brought into a vapor phase, onto a substrate. No chemical reactions between the vapor and substrate are required, unlike in CVD described in Sec. 3.2. Simple evaporator systems suffer of bad step coverage, but are still used to deposit metal layers onto planar substrates. In applications where smaller lateral dimensions are required, deposition by sputtering is often used. Evaporation also comes short when the desired thin film is an alloy, as this is more easily accomplished by sputtering.

3.4.1 Thermal- and Electron Beam Evaporation

In evaporator systems the charge is placed in a crucible which is heated, e.g. simply by a resistive heater element and an external power supply, such that the charge is evaporated. The substrate is placed above the crucible, containing the charge, in a vacuum chamber. The pressure is sufficiently low, which enables the atoms of the vapor to move in a straight line until hitting a surface where they will condense.

To reach even higher temperatures in the crucible, inductive heating can be used. However, this may lead to contamination from the crucible itself. A method to avoid this is by only heating the charge while the crucible is being cooled. This can be obtained by electron beam (e-beam) evaporation. An electron source, usually situated under the crucible, ejects a high energy electron beam. The beam is bent 270° by a strong magnetic field such that the beam is incident onto the charge. The charge is heated by energy transferred from the e-beam and hence evaporated.

All metallization of samples characterized were conducted by thermal evaporation in a Balzers BAE 250 coating system.

3.4.2 Sputtering Deposition

Sputtering deposition is a physical process where a plasma is created and used to extract material from a target and collected at the surface of a substrate to form a thin film. Sputtering offers better step coverage than thermal evaporation, and induce less radiation damage than e-beam evaporation. Multiple targets can be used, in so called co-sputtering, in order to deposit alloys or compounds.

An inert gas (Ar, in many cases) is introduced between two electrodes in a vacuum chamber. The material to be deposited (target) is placed at the cathode, while the substrate is placed at the anode. The inert gas is ionized and accelerated by an electric field resulting in a bombardment of positive ions, from the inert gas, at the target(s). The process of material being ejected from a target due to ion bombardment is explained in Sec. 4.1.1. In the case where conducting target(s) are used, direct current (DC) sputtering is

favoured due to its high deposition rate. If the target material is insulating, DC sputtering will cause surface charge build up which eventually stop the target bombarding. Here, an alternating current (AC) operated at radio frequency (RF) is utilized as this will alternate between bombarding the target with ions and secondary electrons maintaining the plasma. The secondary electron yield is increased by employing a magnetic field created by a magnetron, hence the technique is called magnetron sputtering. The magnetic field causes electrons to move in a helical path towards the anode resulting in a denser plasma, thus increasing the sputtering yield and deposition rate.

The CZTS precursors for tandem fabrication were co-sputtered in a Lesker CMS-18 system configured with three targets made of CuS, SnS and ZnS. All of them being 4 mm thick and 76 mm in diameter with purities of 99.99%. Pulsed DC sputtering was employed for CuS- and SnS-targets, while RF sputtering was used for the insulating ZnS-target. The substrate temperature was set to be $\sim$ 250 °C. The growth of CZTS absorbers is explained in more detail in Sec. 2.5.2.

After CdS deposition by CBD on top of the CZTS absorbers, the samples were placed in a Von Ardenne sputtering system for RF sputtering of the window layers. A layer of 80 nm resistive intrinsic ZnO (i-ZnO) and 210 nm Al-doped ZnO (AZO) together makes up the window layer. The i-ZnO layer is deposited on top of the CdS layer to prevent shunt paths across the CZTS absorber. The AZO is deposited as a transparent front electrode and should offer maximum lateral electrical conductivity.

CHAPTER 4

Experimental Methods - Characterization

In this chapter, the experimental methods used for characterization in this thesis will be presented.

4.1 Secondary Ion Mass Spectrometry

This section is to some extend based on the book by Heide [55] and describes the principles of dynamic secondary ion mass spectrometry.

Secondary ion mass spectrometry (SIMS) is a technique which can be used to characterize the surface and subsurface of solids. Energetic primary ions are focused onto the sample to sputter and ionize secondary ions from the sample surface. The secondary ions are accelerated using an electric field between the sample and the immersion lens to form a secondary ion beam. The ions in the secondary beam are separated by mass (and charge) in a mass spectrometer, before ion intensities are measured. SIMS is a widely used analytical technique to study impurities in solids. The main strengths of SIMS is its high sensitivity with detection limits below one part per million (ppm) for almost all elements, and down to part per billion (ppb) for some elements, high depth resolution and a dynamic range that spans over five orders of magnitude.

By scanning the mass range while sputtering the sample, a mass spectrum is produced. Alternatively, one can select one or more masses to be sequentially monitored while sputtering, producing a depth profile. SIMS

can also be used to create an image of lateral impurity distributions by synchronizing the focused primary beam with the ions collected at the detector. An extended illustration of the operating principle of the SIMS used in this thesis can be found in Fig. 4.1.

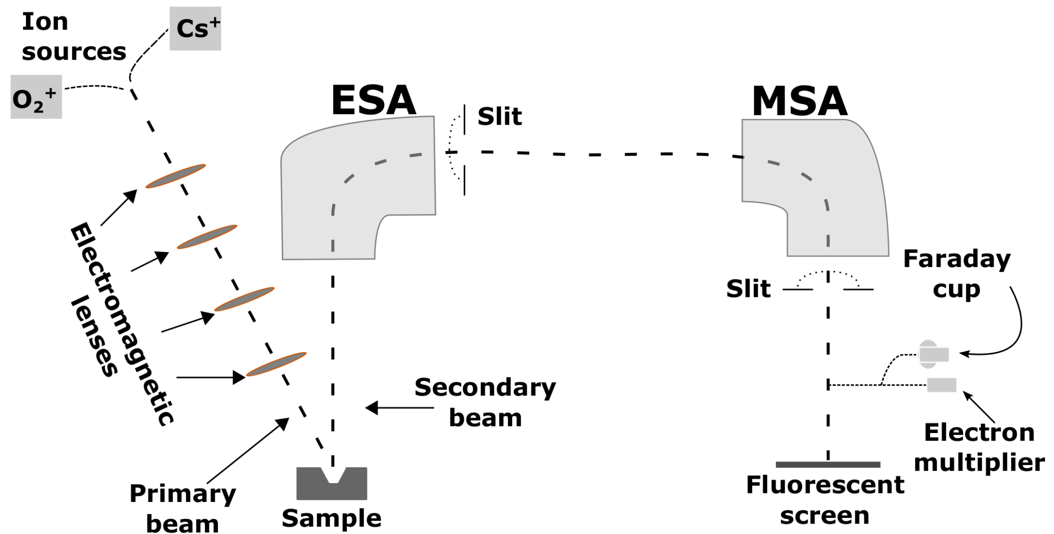

Figure 4.1: A schematic figure of the SIMS operated in this thesis. The primary beam (from either the $O_2{}^+$ or the Cs^+-source) are focused through four electromagnetic lenses before reaching the sample. The ejected secondary ions, which are forming the secondary beam, are separated by charge and mass. At last, the secondary ions can be observed on the fluorescent screen or counted by the electron multiplier. In case of high intensities, the ions are detected by a Faraday cup.

4.1.1 The Physics of Sputtering and Ionization

Bombarding the surface of a material with an energetic beam of ions can cause different scenarios depending on the energy of the impinging species. For very low energies, the ions are reflected off the surface. For slightly higher energies ($\sim$ 10 eV), ions may be adsorbed and give off its energy to phonons. Ions with energies exceeding tens of keV may be implanted into the crystal lattice. Here, the ions penetrate several atomic layers into the material and giving off its energy deep into the substrate[1].

[1]This is the principle of ion implantation a technique used e.g. for doping, fabricate reference samples for SIMS measurements and more.

The primary ion beam in SIMS is operated at 5-15 keV providing target atoms close to the surface with sufficient energy to eject off the material, a process known as sputtering. The sputtering yield (Y), the average number of ejected atoms per incident ion, depend on primary ion energy and mass, angle of incidence, surface binding energy and target atom mass. For the sputtered atoms to be analyzed, they must be ionized. The secondary ion yield (number of atoms that are ionized per emitted atom) is often considered as an ionization probability, γ. The number of sputtered atoms, and the fraction which are ionized depends heavily on the surface chemistry. Thus, the secondary ion yields of the same element may vary significantly for different matrices. Such a matrix effect can make the examination of compositional variations within the measured solid problematic. This is one of the reasons why SIMS is considered a qualitative technique. However, as discussed in Sec. 4.1.3, secondary ion counts may be quantified by measuring a calibrated reference sample.

4.1.2 Analysis

After the secondary ions have escaped the sample surface, they pass through an electrostatic energy analyzer (ESA) and magnetic sector analyzer (MSA) as shown i Fig. 4.1. The ESA acts as an energy filter to reduce chromatic aberrations. A voltage of opposite polarity is applied to the two curved electrodes forming the ESA, such that an electric field of E is present between the electrodes. The ions will experience a centripetal force F_E given as

$$F_E = qE, \tag{4.1}$$

where q is the elementary charge. The centripetal force acting on an ion with mass m moving through the ESA with a tangential speed v_E in a curvature of radius r_E is

$$F_E = \frac{mv_E^2}{r_E}, \tag{4.2}$$

leading to the following relation

$$qE = \frac{mv_E^2}{r_E}. \tag{4.3}$$

The ions with a kinetic energy allowing them to pass unobstructed through the ESA will enter the MSA, where they are exerted by a Lorentz force F_B

$$F_B = qv_M B, \tag{4.4}$$

where B is the magnetic field in the MSA. By following the same procedure which lead to the relation in Eq. 4.3, we end up with

$$qB = \frac{mv_M}{r_M}. \tag{4.5}$$

Now assume no energy loss ($v_E = v_M$). Then, by rearranging Eq. 4.3 and Eq. 4.5 one end up with

$$\frac{m}{q} = \frac{(r_M B)^2}{r_E E}. \tag{4.6}$$

From Eq. 4.6, with r_E, r_M and E constant, the magnetic field can be varied to determine which mass-to-charge that pass through the MSA-exit slit and will be detected. In addition to filter ions by energy, the ESA prevents undesirable charged species to reach the detectors, e.g. molecular ions. However, when analyzing SIMS spectra one need to be aware of possible mass interferences with ionized molecules which have escaped through the ESA.

4.1.3 Quantification

The intensity from secondary ions of element i can be quantified as

$$I_i = I_P Y \gamma_i T C_i, \tag{4.7}$$

where I_P is the primary ion beam intensity, Y is the sputtering yield, T an instrument transmission function, γ_i the ionization probability and C_i the concentration of element i. The four proportionality constants in front of the

concentration of element i in Eq. 4.7 are often referred to as the sensitivity factor (SF_i)

$$(\mathrm{SF_i})^{-1} = \mathrm{I_P Y} \gamma_\mathrm{i} \mathrm{T} = \frac{\mathrm{I_i}}{\mathrm{C_i}}. \tag{4.8}$$

By measuring a reference sample implanted with a known dose of element i, a conversion from secondary ion intensity to concentration of i is feasible.

As pointed out earlier, secondary ion intensities of elements of interest are recorded as a function of time. However, in order to convert from time to depth, the crater depth of the sputtered area need to be determined. The crater depths sputtered during SIMS measurements in this work were measured by a Dektak 8 Stylus profiler after SIMS measurements. Constant sputter rates are assumed, and determined separately in each layer in the case of heterostructures.

4.1.4 Instrumentation

The SIMS measurements conducted in this thesis have been performed with the microanalyzer Cameca IMS-7f which is equipped with both a duoplasmatron and a cesium-source. Both an electrostatic sector analyzer and a magnetic sector analyzer are present in the instrument, as well as three detectors: Faraday cup, electron multiplier and a fluorescent screen. The sputtered craters are formed by rastering the primary ion beam over a quadratic area with dimensions in the range between 50×50 μm^2 and 500×500 μm^2. An ultra-high vacuum is required for the ions to reach the detectors. The base pressure in the sample chamber is $\leq 10^{-9}$ mbar to ensure a sufficiently long mean free path for the ions. In the case of high-resistive samples, the SIMS is equipped with an electron gun to bombard the sample with electrons to avoid charge build-up.

4.2 X-Ray Diffraction

This section is based on the book by Birkholz [56].

X-ray diffraction (XRD) is a non-destructive technique used for struc-

tural investigation of crystalline materials. X-rays are high energy electromagnetic radiation, where the wavelengths (0.01-10 nm) are comparable with interatomic spacing (0.15-0.4 nm). The technique rely on scattering of X-rays by atoms in the crystal and detection of diffraction phenomena whenever constructive or destructive interference occur.

Three different types of scattering processes may take place in the interaction between X-ray and matter. Two of them are inelastic, meaning the incident photons transfer its energy and momentum to an electron. The first process is called photoelectric effect, where the transfer cause a photoelectron to be released from its bound state. An inelastic scattering may not cause photoionization, but still lower the energy of the incident photon, this is the second process called Compton scattering. The third process is the low energy limit of Compton scattering and is called Thompson scattering. Here, the energy and momentum of the incident photons are conserved. Structural investigation of materials by XRD rely on the latter process.

Consider an incoming X-ray with wave vector $\mathbf{K_0}$, being scattered by atoms in a crystal with an outgoing wave vector $\mathbf{K}$. The scattering vector, the difference between the two wave vectors, equals

$$\mathbf{Q} = \mathbf{K} - \mathbf{K_0}, \tag{4.9}$$

as illustrated in Fig. 4.2.

Lets assume a cubic lattice for the material under investigation, with lattice constant a. The Laue equations describe the necessary condition to achieve maximum intensity for the scattered wave

$$\begin{aligned} a\mathbf{Qa} &= 2\pi h \\ a\mathbf{Qb} &= 2\pi k \\ a\mathbf{Qc} &= 2\pi l, \end{aligned} \tag{4.10}$$

where $\mathbf{a}$, $\mathbf{b}$ and $\mathbf{c}$ are the basis vectors of the crystal lattice and h, k and l are Miller indices of the crystal planes responsible for the scattering. The magnitude of $\mathbf{Q}$ at maximum intensity is given as the absolute value of the

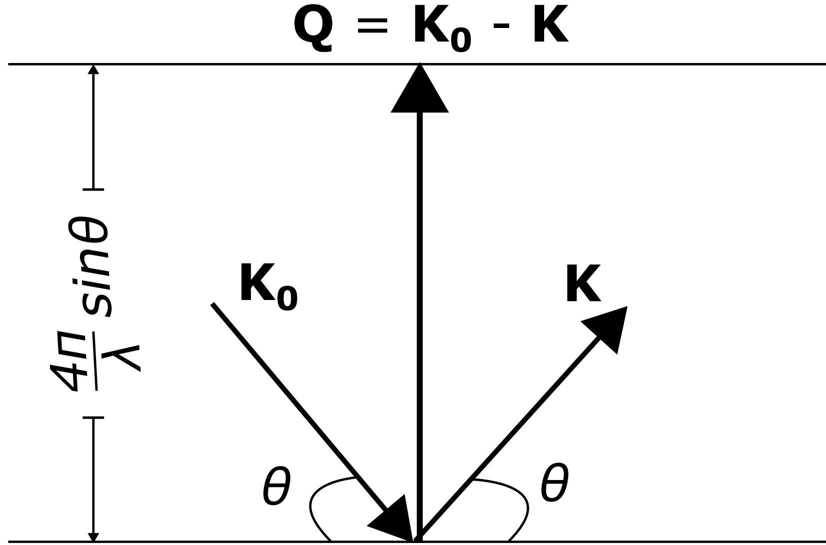

Figure 4.2: Geometry of the scattering vector in reciprocal space.

sum of the equations in 4.10

$$\frac{|\mathbf{Q}|}{2\pi} = \frac{\sqrt{h^2 + k^2 + l^2}}{a}. \tag{4.11}$$

By considering the geometry of Fig. 4.2 the length of **Q** can be found as $4\pi \sin\theta/\lambda$. After inserting this into Eq. 4.11 one obtain

$$2\frac{a}{\sqrt{h^2 + k^2 + l^2}} \sin\theta = \lambda. \tag{4.12}$$

One can recognize $a/\sqrt{h^2 + k^2 + l^2}$ as the distance between two adjacent planes in a cubic lattice, d_{hkl}. From these calculations the Bragg equation have been derived

$$2d_{hkl} \sin\theta_B = \lambda, \tag{4.13}$$

where θ_B is the angle at which maximum intensity is achieved. The Bragg equation tells us that whenever the radiation travel a distance inside the material equalling an integer number of wavelengths, constructive interference will occur. A simple cubic lattice with one atom in the unit cell was assumed in this derivation, but Eq. 4.13 holds for other lattice structures as well. However, more atoms in the unit cell may induce destructive interference for

certain reflections, e.g. in the fcc structure crystal planes with Miller indices all even or odd give constructive interference, while mixed Miller indices give destructive interference.

4.3 Glow-Discharge Optical Emission Spectroscopy

This section is based on the book by Nelis *et al.* [57].

Glow-Discharge Optical Emission Spectroscopy (GDOES) is an analytical technique used to study the chemical composition with depth in materials. It is similar to SIMS, but GDOES require less measurement time (tens of seconds) and is far more destructive in terms of removal of material (craters with dimensions of millimeter). Even though its detection limit ($\sim$ 10 ppm) and depth resolution (5-10 % of sputtered depth) are not as high as for SIMS, GDOES serve as an easy and fast technique for a wide range of solids.

In order to develop the glow-discharge, a potential difference is applied between the metal chamber wall (acting as anode) and the sample (acting as cathode). The gas in the chamber, usually argon at low pressure, start to ionize forming the plasma. The electrons are accelerated towards the anode, creating more positive ions, while the positive ions are accelerated towards the cathode/sample. This bombardment of the sample causes atoms to be sputtered from the surface into the plasma where they are excited by electrons already in the plasma. The sputtered ions will emit a photoelectron in order to return to their ground state. This photoelectron has a wavelength that is characteristic of the element responsible for the emission. The light emitted is passed through a spectrophotometer to separate the light into the specific wavelengths of each element represented in the plasma. The intensity of the light emitted is directly proportional to the concentration in the plasma, hence to the sample surface.

4.4 μ-Wave Detected Photoconductance Decay

This section is based on the book by Schroder [16]

Minority carrier lifetime measurements by μ-wave detected photoconductance decay (μ-PCD) offer high spatial resolution of the sample under test. However, no knowledge of the injection level is obtained unless large area bias light is used to set the injection level in the sample.

Almost every minority carrier lifetime measurements are based on the change in excess carrier concentration

$$\frac{d\Delta n(t)}{dt} = G(t) - R(t), \tag{4.14}$$

which is the balance of generation and recombination of carriers. By inserting Eq. 2.18 into Eq. 4.14 and rearrange for τ_{eff}, the following expression is obtained

$$\tau_{eff} = \frac{\Delta n(t)}{G(t) - d\Delta n(t)/dt}. \tag{4.15}$$

In μ-PCD, the excess carrier concentration is generated by applying a short light pulse, of transient nature, and photoconductance is measured during the decay of Δn. The generation rate is zero throughout the decay, thus Eq. 4.15 reduces to the simple differential equation

$$\tau_{eff} = -\frac{\Delta n(t)}{d\Delta n(t)/dt}, \tag{4.16}$$

where solutions of $\Delta n(t)$ are on the form

$$\Delta n(t) = \Delta n(0)e^{-t/\tau_{eff}}, \tag{4.17}$$

where t is the time of the measurement and $\Delta n(0)$ is the excess carrier concentration after applying the pulse and right before the start of the decay.

The excess carrier concentration is related to the photoconductance through

$$g = qW[\mu_n(\Delta n + n_0) + \mu_p(\Delta n + p_0)], \tag{4.18}$$

where W is the wafer thickness. We are interested in the excess conductance, which is simply

$$\Delta g = qW\Delta n(\mu_n + \mu_p). \tag{4.19}$$

The mobilities are dependent on Δn and are often assumed to be constant throughout the measurement, if not Δn is determined by iteration. Photoconductance-based systems are designed such that the measured voltage is related to the conductivity.

In μ-PCD set ups, the wafer and a ring-shaped microwave antenna, used near the resonance frequency, form a resonator. The basic principle is that an increase in free carrier concentration changes the dielectric function of the semiconductor, and thus the optical response, i.e. increased reflectivity in the microwave region. When the conductance in the wafer increases, a shift in the resonance curve is observed. The conductivity in the wafer is monitored by the reflectance of the microwave. The signal from the conductivity decay is fitted to an exponential time curve, hence the minority carrier lifetime is obtained.

4.5 Capacitance-Voltage Measurements

Measurement of capacitance-voltage (CV) characteristics is a fast and easy technique to obtain information about charge behaviour in semiconductors. Important parameters, such as doping concentration (N_D or N_A) and built-in voltage (V_0) of Schottky diodes, pn-junctions and MOS-capacitors can be deduced from one quick scan.

The capacitance of a junction can be defined as the change in fixed charges (ΔQ) in the SCR due to a change in applied voltage (ΔV). If considering a p^+n-junction as a parallel-plate capacitor with a thickness equal the width

of the SCR (W), the junction capacitance is given as

$$C = A\frac{\epsilon_0\epsilon_r}{W} = A\sqrt{\frac{q\epsilon_0\epsilon_r}{2(V_0+V)}N_D}, \tag{4.20}$$

where A is the diode area, ϵ_0 is the permittivity of free space, ϵ_r the relative permittivity of the material and V is the applied voltage. The expression used for W in Eq. 4.20 can be derived from an electrostatic analysis of a pn-junction. Rearrangement of Eq. 4.20 lead to the following expression

$$\frac{1}{C^2} = \frac{2}{qN_D\epsilon_0\epsilon_r A^2}V_0 + \frac{2}{qN_D\epsilon_0\epsilon_r A^2}V, \tag{4.21}$$

which produce a straight line. From Eq. 4.21, the donor concentration can be found from the slope and built-in voltage from the intersect between the extrapolated line and abscissa.

4.6 Deep-Level Transient Spectroscopy

This section is based on Chapter 8 in the book by Blood and Orton [17] and Lang [58].

Deep-Level Transient Spectroscopy (DLTS) is a powerful and sensitive technique for investigating electrically active traps in semiconductors. The method was first introduced by Lang in 1974 [58]. Capacitance transients are measured as a function of temperature and the obtained spectrum can give information about electronic properties of defects present in the semiconductor where a depletion layer (the SCR) is present. The defect signatures introduced in Sec. 2.2.4, such as trap concentration, apparent capture cross section and energy level in the band gap, can be quantified from DLTS measurements.

4.6.1 Principle of Operation

In DLTS, emission of majority carrier traps is observed by capacitance transients. An asymmetrically doped pn-junction or Schottky diode is usually

preferred, as the SCR will mainly extend into the lower doped side of the junction. The diode is fixed at a reverse bias V_{rb} before being pulsed by a positive voltage V_p, as shown in Fig. 4.3. The condition $(V_{rb} + V_p)$ is held at a time t_p in which majority carrier traps are filled. Shortly after V_p is

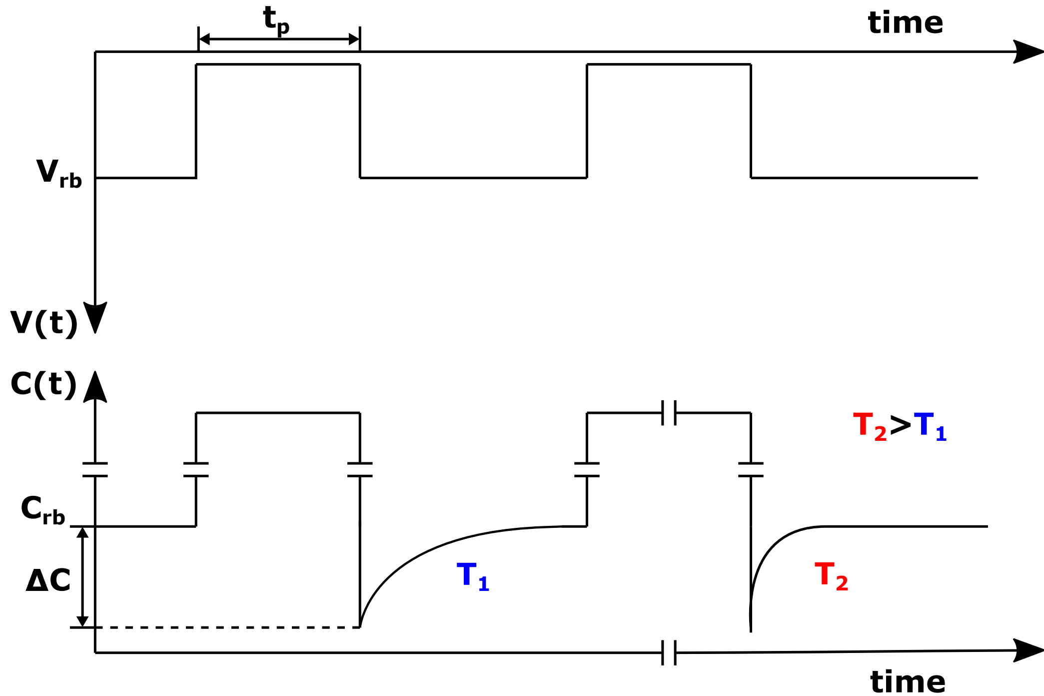

Figure 4.3: The top figure shows the diode kept at reverse bias V_{rb} then pulsed by a voltage V_p for a time t_p. The bottom figure shows the corresponding capacitance showing two transients at two different temperatures, T_1 and T_2.

removed and V_{rb} is restored, all traps within the SCR are filled. This results in a slightly increased depletion width, thus an increase of ΔC in diode capacitance as illustrated in Fig. 4.3. The filled traps will now start to emit majority carriers such that the occupancy of traps exponentially decrease according to

$$n_T(t) = N_T e^{-e_n t}, \tag{4.22}$$

hence producing the capacitance transients illustrated in Fig. 4.3. The capacitance at a time t after the pulsing can be expressed as

$$C(t) = C_{rb} + \Delta C e^{-e_n t} \tag{4.23}$$
$$= A\sqrt{\frac{q\epsilon_0\epsilon_r}{2(V_0+V_{rb})}N_D^{SCR}}, \tag{4.24}$$

where the last expression comes from the junction capacitance of a n-type semiconductor in Eq. 4.20. Filled traps inside the depletion region reduces the effective doping in the SCR

$$N_D^{SCR} = N_D - n_T(t) = N_D - N_T e^{-e_n t}, \tag{4.25}$$

giving the following expression for the capacitance transient

$$C(t) = A\sqrt{\frac{q\epsilon_0\epsilon_r}{2(V_0+V_{rb})}N_D}\sqrt{1-\frac{N_T}{N_D}e^{-e_n t}} = C_{rb}\sqrt{1-\frac{N_T}{N_D}e^{-e_n t}}. \tag{4.26}$$

By assuming the concentration of traps to be much smaller than the concentration of donors ($N_T \ll N_D$), Eq. 4.26 simplifies to

$$C(t) = C_{rb}\left(1-\frac{N_T}{2N_D}e^{-e_n t}\right). \tag{4.27}$$

According to Eq. 4.27 and Eq. 4.23 the peak change in capacitance must be given by

$$\Delta C = \frac{C_{rb}N_T}{2N_D}, \tag{4.28}$$

which is proportional to the trap concentration when assuming that the trap concentration is uniform with depth.

4.6.2 Generation of the DLTS Spectrum

The emission rate of majority carriers has a strong temperature dependency, as seen in Eq. 2.24. By measuring the average of the capacitance transients, while varying the temperature, a DLTS spectrum is constructed, as illustrated in Fig. 4.4. For example, the capacitance transients can be processed

by calculating the difference in capacitance between two fixed times, t_1 and t_2 as shown in Fig. 4.4. If the width of this time window (t_w) is varied, the position of the peak is shifted. These shifts in observed maximum capacitance transient allows the emission rate to be calculated for different temperatures, thus creating the Arrhenius behaviour discussed in Sec. 2.2.4.

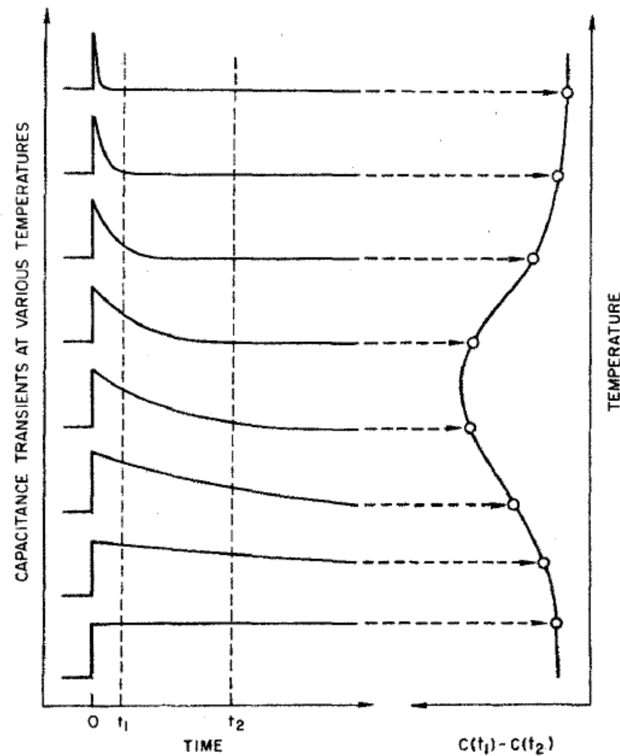

Figure 4.4: The graph to the left shows capacitance transients at different temperatures. The vertical graph to the right shows how a peak in the DLTS spectrum is constructed from the difference in capacitance in a fixed time window. Adapted from Lang [58].

For a better extraction of the DLTS signal from noise, the measured transients are multiplied by a weighting function $w(t)$, instead of the two fixed times (t_1 and t_2) used for illustration above. A popular weighting function giving good signal-to-noise ratio is the lock-in filter. It takes the sum of all values from $t_w/2$ to t_w and subtracts the sum of all values from time equal 0 to $t_w/2$. However, the energy resolution obtained by the lock-in filter is low, and may give difficulties in separating nearby energy levels (i.e.

giving rise to overlapping peaks), and a GS4 filter can been applied for better resolution. However, an improved energy resolution is gained at the expense of a lower signal-to-noise ratio.

4.6.3 Data Extraction and Physical Interpretation

The emission rate for different time windows can be calculated from the peaks in the DLTS spectrum. A simulation of such a DLTS spectrum with its different time windows is illustrated in Fig. 4.5, where the inset illustrates an Arrhenius plot of Eq. 2.25

$$\ln\left(\frac{e_n}{T^2}\right) = -\frac{\Delta H}{kT} + \ln(\beta_n \sigma_{na}),$$

obtained from the calculated emission rates. The sign of the DLTS signal may reveals whether the peak belongs to a majority- or minority carrier trap, while the trap concentration is directly proportional to ΔC as seen in Eq. 4.28.

In Sec. 2.2.4 an expression for emission rate was derived from a thermodynamic point of view. This revealed that the calculated activation energy does not include the entropy, and the extracted capture cross section is found at $T \to \infty$. The activation energies obtained are often stated as $(E_c - E_T)$, the position of the trap states relative to the conduction band edge. However, the activation energy is not directly the energy level of the trap (also interpreted from thermodynamics) as this only holds if $(E_c - E_T)$ is itself temperature independent. If this is not true, both the energy position and capture cross section will be modified from the temperature dependency.

Evaluations of the peak shapes in DLTS spectrum may reveal information of the dimensionality of the defect observed. In DLTS, point defects are normally studied and considered in the theory, which produce symmetrical peaks as illustrated in Fig. 4.5. However, the shape of an extended defect may deviate from that of a point defect, making it chalenging to interpret the data and obtaining quantitative information about the electronic properties of extended defects. As an example, Schröter *et al.* studied $NiSi_2$ platelets

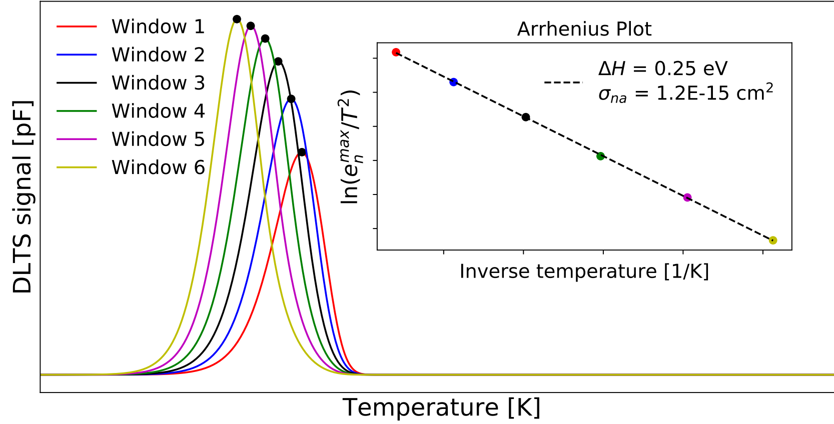

Figure 4.5: An example of a simulated DLTS spectrum using the lock-in weighting function with six time windows. The inset is the Arrhenius plot obtained from calculating the emission rates from the peaks in the DLTS spectrum (illustrated with black dots). The position of the trap level relative to the conduction band is calculated from the slope of the linear fit, while the apparent capture cross section, σ_{na}, is the extrapolated value at $1/T \rightarrow 0$. The trap concentration is proportional to the peaks in the spectrum, giving $N_T = 10^{13}$ cm^{-3} for a donor concentration of 10^{15} cm^{-3}.

and dislocations in Si using DLTS [59]. Their simulations and experimental results revealed a broadening towards lower temperatures for peaks related to extended defects. Furthermore, electronic states from extended defects are subject to more bandlike states, different from energy states origin from point defects.

4.7 Scanning Electron Microscopy

This section is based on the book by Leng [60].

Scanning electron microscopy (SEM) is a popular technique to examine microscopic structure. An electron beam is emitted from an electron gun by applying an accelerating voltage of 1-40 kV. This electron beam is focused on to the sample by several electromagnetic lenses and deflected on to the sample surface. The generated intensity from scanning the electron beam

over the sample surface is mapped acquiring an image yielding information about structure, chemical composition, surface topography and more.

The electrons bombarding the sample are either inelastically- or elastically scattered. In the latter case, the electrons are back scattered by atoms in the sample giving compositional contrast in the acquired image. Inelastic scattering produces secondary electrons (SE) through incident electrons transferring its kinetic energy to electrons in the sample. Electrons with sufficient kinetic energy will be emitted by its orbital becoming a SE. Only SE generated close to the sample surface (few nm) will have sufficient energy to reach the detector. This gives good spatial resolution, thus revealing information about the sample topography.

CHAPTER 5

Results and Discussion

This chapter is dedicated to the main findings of the experimental work and will discuss the presented results. To advance the progress of CZTS-on-Si tandem solar cells, two topics have been identified in this work that requires specific investigation; band gap engineering of the CZTS top cell, and the interface between the Si and the CZTS. In particular, interdiffusion of the elements in CZTS may occur, where in-diffusion of Cu into the Si bottom cell may be detrimental. Finally we develop, fabricate and characterize the full tandem structure, revealing promising results for further development.

5.1 SIMS and GDOES as Tools to Study Ge Gradient in CZTGS

As previously addressed, incorporation of Ge in CZTS is a route to achieve a band gap of 1.7 eV, the optimum top cell band gap in a Si-based tandem solar cell. Additionally, a variation of x with depth, in $\mathrm{Cu_2ZnSn_{1-x}Ge_xS_4}$, results in a compositional gradient and thus a gradient in the band gap. Such a band gap gradient is a potential method to increase the efficiency of chalcogenides by decreasing interface recombination. In this study, Ge/Sn graded CZTGS samples have been measured with SIMS and GDOES. The depth resolution and detection sensitivity of SIMS is higher than that of GDOES. However, SIMS measurement may be affected by a matrix effect (see Sec. 4.1.1 for a

description of the matrix effect), while this potential effect is not an issue for GDOES measurements. The two techniques have been compared to establish the validity of measuring depth profiles of Ge/Sn gradients in this material system.

5.1.1 Sample Preparation

Here, efforts to form a band gap gradient were made by co-sputtering of CZTS subsequently on top of CZGS already deposited on a Mo coated SLG substrate. The CZTS precursors were co-sputtered as described in Sec. 3.4.2, and the CZGS presursors were co-sputtered by switching the SnS target with a Ge target. The thickness of the two precursors should be $\sim$ 200 nm by considering the duration of the co-sputtering. However, the co-sputtering of CZGS resulted in only 100-150 nm of precursor. Four samples were prepared whereas three of them were sulphurized for 2, 6 and 13 minutes, while the last was kept as-deposited (precursor). A process flow of the sample preparation described above is illustrated in Fig. 5.1. In order to investigate the crystallization of the precursors after sulphurization, XRD measurements were conducted on all samples. The XRD results in Fig. 5.2 show the evolution of the characteristic kesterite peaks and suggest a higher degree of crystallinity for longer sulphurization. Here, the sample is scanned through a range of angles 2θ (x-axis). Whenever the incident X-rays and the diffracted ray (from the sample) exhibit constructive interference, a peak in intensity is detected (y-axis).

5.1.2 SIMS Results

Depth profiles obtained from SIMS of S, Cu, Zn, Ge, Mo and Sn in all samples are presented in Fig. 5.3. A detailed table of the primary beam ions employed and species detected can be found in Tab. A.1 in Appendix A. The Mo interfaces are assumed to be at the half-maximum of the Mo intensity, which is illustrated by a black vertical line. Such a black line is used in all SIMS and GDOES depth profiles to illustrate the CZTGS/Mo interface. The Ge intensity of the precursor (Fig. 5.3a) increases near the

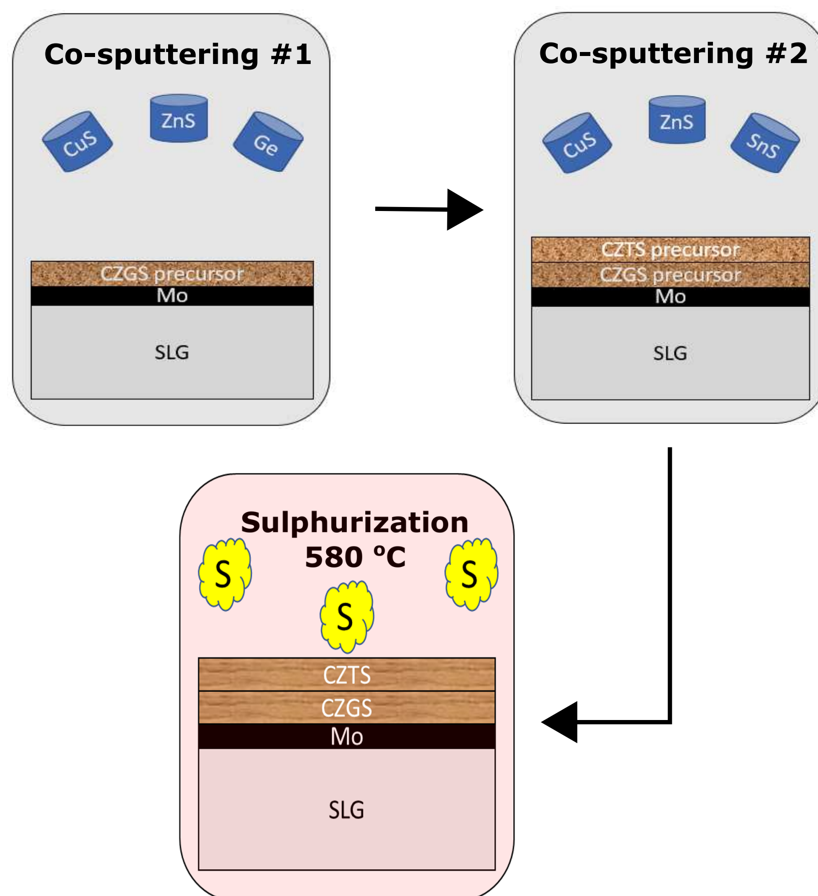

Figure 5.1: Process flow of the growth of the CZTGS samples characterized in this section.

Mo back contact confirming the $\sim$ 100 nm thick CZGS prucursor layer. In this layer, the Cu signal decreases and the Zn signal increases. The change in intensities might suggest that the CZGS layer is more Cu-poor and Zn-rich than the CZTS layer on top. However, after only 2 minutes of sulphurization, interdiffusion of the elements between the CZGS and the CZTS layers has occured, as can be seen from Fig. 5.3b. The depth profiles in Fig. 5.3c show that after 6 minutes of sulphurization we can see a clear incorporation of Ge towards the surface and diffusion of Sn to depths corresponding to the deposited CZGS precursor. The longest sulphurization (13 minutes) results in complete mixing of Sn and Ge, and no separate CZTS and CZGS layers are present. However, the Sn intensity decrease faster than the Ge intensity

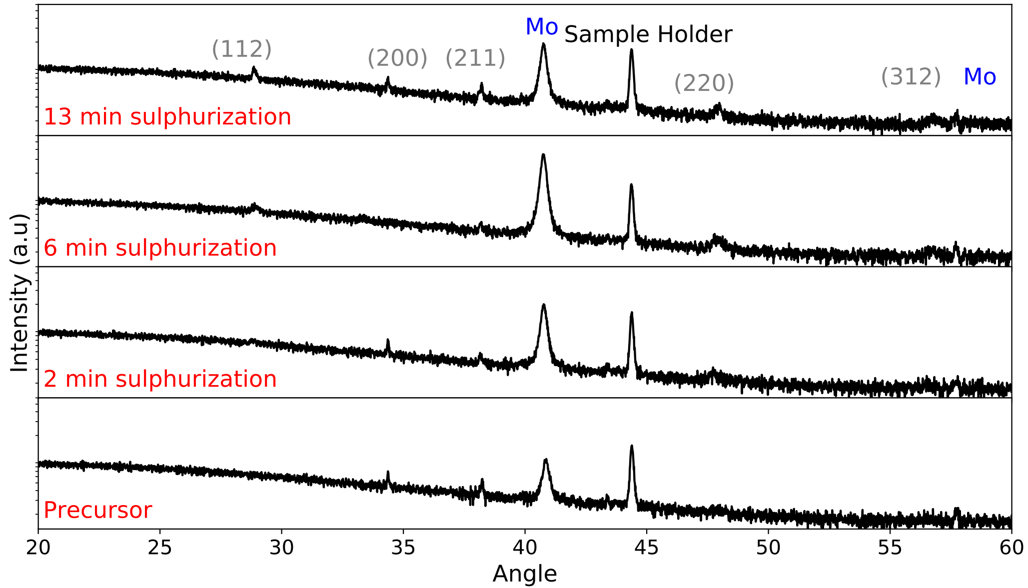

Figure 5.2: XRD results for the CZTS/CZGS samples with different sulphurization times at 580 °C. CZTGS related peaks are included in grey, wthe intensity peaks from the Sample Holder and the Mo are indicated with black and blue text, respectively.

close to the Mo interface. Notably, the longest sulphurized sample (Fig. 5.3d) shows a peak in the S intensity extending into the Mo interface. The peak in S intensity and stagnation in Mo intensity (between 300 and 400 nm) may indicate a formation of MoS_2 at the Mo interface. A minor peak in Zn intensity can be observed towards the CZTGS surface coupled with a decrease in Cu signal with depth. The high Zn intensity towards the surface indicate the formation of ZnS with Cu-poor conditions. However, this remain a speculation since no additional peaks were observed by XRD, although such secondary phases may be too thin for a pronounced signature in XRD and/or give overlapping peaks.

5.1.3 GDOES Results

The sputtered crater depths of the samples after GDOES measurements were not measured, hence a conversion from measurement time to depth cannot be performed directly. However, by assuming that the Mo interfaces calculated

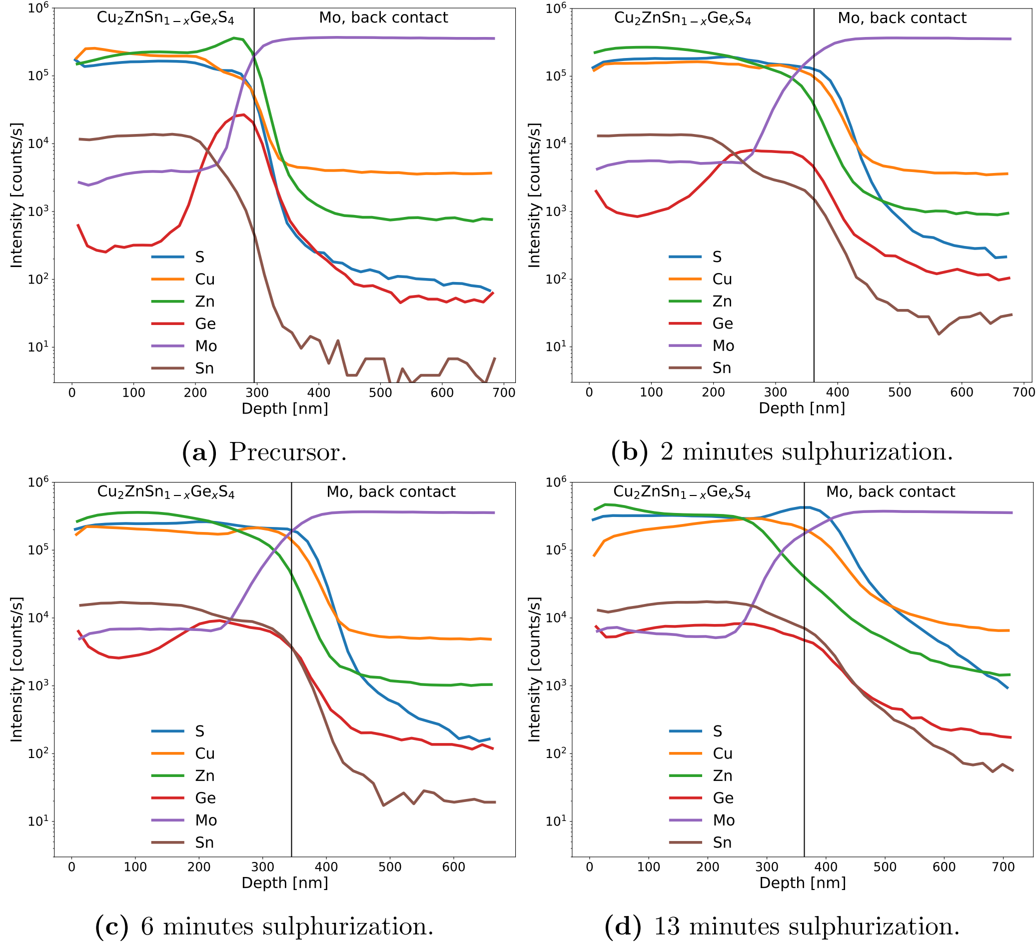

(a) Precursor.

(b) 2 minutes sulphurization.

(c) 6 minutes sulphurization.

(d) 13 minutes sulphurization.

Figure 5.3: Depth profiles from SIMS of the evolution of the CZTS/CZGS stack for different annealing times. (a) 200 nm CZTS precursor layer stacked on top of a 100 nm CZGS precursor (b) after 2 minutes sulphurization, (c) after 6 minutes sulphurization and (d) after 13 minutes sulphurization. A sulphurization time of 2 minutes (b) induce interdiffusion of elements between the CZTS and the CZGS layers. Further diffusion is observed after 6 minutes of sulphurization (c), and after 13 minutes sulphurization (d) a complete exchange of Ge and Sn between the two layers have occurred.

from GDOES and SIMS occur at the same depth, the sputter rate in CZTGS can be determined, and thus the time be converted to depth.

The depth profile obtained from GDOES of the precursor in Fig. 5.4a shows the same Zn intensity peak in the CZGS precursor as seen from SIMS in 5.3a. In the depth profiles from GDOES and SIMS, a similar evolution

in Zn, Ge and Sn diffusion after sulphurization times of 2 and 6 minutes as seen in Fig. 5.4b and c, respectively. After complete sulphurization, the Sn and Ge intensities in Fig. 5.4d are approximately equivalent throughout the CZTGS layer with no difference in the slope close to the Mo interface.

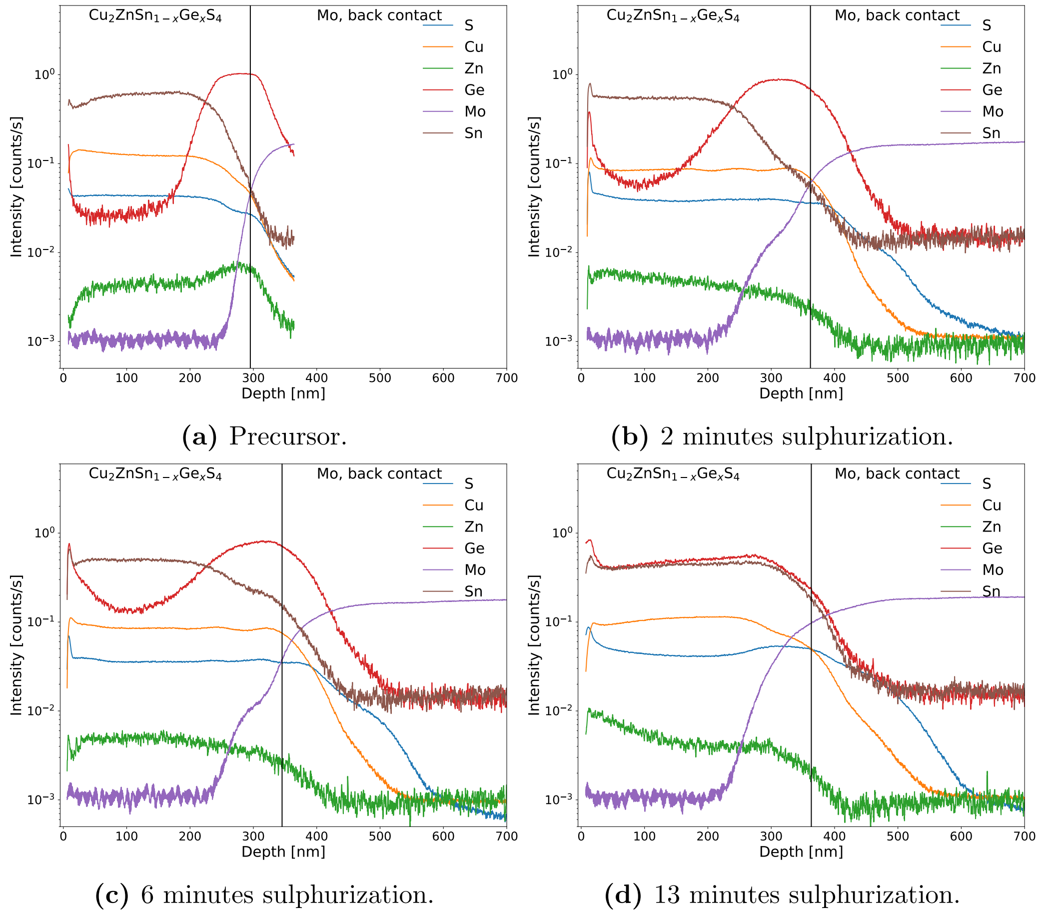

(a) Precursor.

(b) 2 minutes sulphurization.

(c) 6 minutes sulphurization.

(d) 13 minutes sulphurization.

Figure 5.4: Depth profiles from GDOES of the evolution of the CZTS/CZGS stack for different annealing times. The conversions from measurement time to crater depth are based on the assumption that the Mo interfaces calculated from GDOES and SIMS coincides. The depth profiles in (a) show 200 nm CZTS precursor layer stacked on top of a 100 nm CZGS precursor (b) after 2 minutes sulphurization, (c) after 6 minutes sulphurization and (d) after 13 minutes sulphurization. The evolution of Ge diffusion is similar of that observed in Fig. 5.3.

5.1.4 Discussion

When the matrix is changing the sputtering yield and ionization efficiency in SIMS may also change, as discussed in Sec. 4.1.1. All species detected in Fig. 5.3 are clusters formed with Cs in order to minimize this matrix effect [61]. If the correlation of Sn and Ge intensities is constant, i.e. that the sum of them is constant with a decreasing Ge signal accompanied by an increasing Sn signal or *vice versa*, the concentration ratio between them can be calculated. Such a linear dependency is a result of a direct exchange of the elements in the matrix/crystal structure. This has been investigated in Fig. 5.5, where the Sn intensity is plotted as a function of Ge intensity in Fig. 5.5b with the colors corresponding to the regions in Fig. 5.5a. The green region is defined

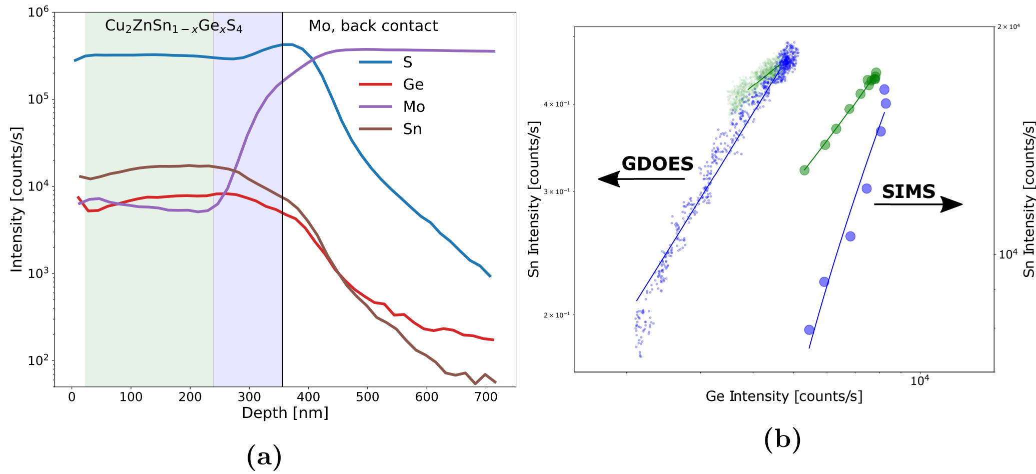

Figure 5.5: (a) Depth profiles of the 13 minutes sulphurized sample with the CZTGS divided into two regions: (green) the region corresponding to the area where the CZTS precursor originated (without the surface) and the region corresponding to the area where the CZGS precursor originated and the Mo interface (blue). (b) Corresponding Sn intensity as a function of Ge intensity where the blue dots are measured intensities from the blue region in (a) and the green dots from the green region. The solid lines are linear fits to the measured intensities.

as the area corresponding to the region where the CZTS precursor originated (without the surface) and the blue as the region corresponding to the area where the CZGS precursor originated in addition to the Mo interface. The correlation in Fig. 5.5b shows a linear dependency in both regions with an

increasing slope, for both GDOES and SIMS. A decreasing slope is expected if the Ge atoms were to substitute the Sn atoms. Instead, the measured intensities indicate an increasing concentrations of both Ge and Sn with depth in both sections, i.e. the sum [Ge]+[Sn] is not constant. This is not unexpected as the growth of CZTGS is not stoichiometric. The SIMS results in Fig. 5.5b alone cannot exclude the matrix effect due to the positive slope. However, the results from GDOES suggest the same linear dependency. In GDOES, the ionization of the sputtered atoms do not depend on the matrix, hence no matrix effect will be present. Thus, the results from GDOES can help excluding the matrix effect from the SIMS measurements.

Assuming that the band gap can be determined from Eq. 2.37 with the Ge/Sn ratio determined from the intensities of Ge and Sn obtained from SIMS, the band gap grading as a function of depth in CZTGS can be calculated as in Fig. 5.6. According to SIMS, the [Ge]/([Sn]+[Ge]) ratio is close to 0.3 in the green section, which is the same ratio estimated by researchers at Uppsala University on the same samples using XRD and Raman spectroscopy measurements. Note that a minor gradient in the band gap is evident towards the Mo interface. This is supported by the depth profiles of Ge

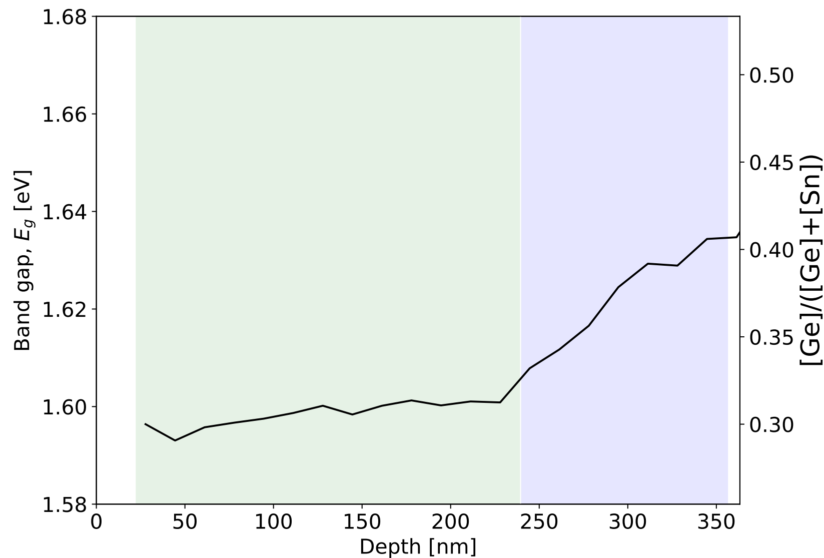

Figure 5.6: Band gap, and Ge/Sn ratio as a function of depth in the 13 minutes sulphurized CZTGS with the regions presented in Fig. 5.5a.

and Sn by GDOES in Fig. 5.4d where the Ge intensity is slightly increasing towards the interface, with the Sn intensity being close to constant.

The depth profiles obtained from GDOES in Fig. 5.4 and those from SIMS in Fig. 5.3 exhibit a good resemblance in terms of diffusion. Nevertheless, the intensities of S and Sn from GDOES in Fig. 5.4d do not show the same behaviour as that of SIMS in Fig. 5.3d close to the Mo interface. Additionally, GDOES does not detect the peak in Zn intensity close the CZTS surface. These dissimilarities may originate from the lower depth resolution of GDOES compared to SIMS. In GDOES a large (in the order of mm) spherical area is analyzed making it difficult to detect peaks in intensity originating from secondary phases that covers only parts of the layer.

The sulphurization of a subsequent co-sputtered CZTS precursor on top of a CZGS precursor led to an increased band gap with a gradient towards the Mo interface, according to SIMS measurements supported by GDOES. However, the incorporation of Ge in CZTS has not been extensively studied, hence pure CZTS absorbers will be employed in the investigation to come, of the effect of CZTS synthesis on the Si bottom cell.

5.2 Interdiffusion From CZTS Synthesis and its Impact on Device Performance

The aim of this work is to explore the degradation of the Si bottom cell following the CZTS synthesis, and investigate in-diffusion of impurities as a potential cause. Further, the effect of a TiN diffusion barrier on diffusion resistance is studied and the dependence of TiN layer thickness. In addition, the impact of the TOPCon configuration on in-diffusion is investigated. The results following this work are reported in [62] (to be submitted to Advanced Energy Materials).

All samples in this section was prepared at DTU in Denmark. Si wafers with and without the TOPCon structure were analyzed. In the samples with TOPCon, n^+ poly-Si was deposited on both sides according to the processing described in Sec. 3.1. Barrier layers of 25 nm TiN were deposited on the backside, and 0, 10 and 25 nm on the front by PEALD (Sec. 3.2.1). Further, CZTS precursors were deposited by co-sputtering (Sec. 3.4.2) and sulphurized at 525 °C for 30 minutes.

All samples are identified by name based on structure and configuration, as listed in Tab. 5.1. After the CZTS deposition and sulphurization, the

Table 5.1: Overview of samples characterized in this section, including sample identification and its respective strucute.

Name:	**Sample:**	**TiN thickness:**	**TOPCon:**
CZTS/0TiN/T-Si	Tandem	0 nm	Yes
CZTS/10TiN/T-Si	Tandem	10 nm	Yes
CZTS/25TiN/T-Si	Tandem	25 nm	Yes
Cu/25TiN/T-Si	Reference	25 nm	Yes
CZTS/0TiN/Si	Tandem	0 nm	No
CZTS/10TiN/Si	Tandem	10 nm	No
CZTS/25TiN/Si	Tandem	25 nm	No
Cu/25TiN/Si	Reference	25 nm	No

sample with no TiN (CZTS/0TiN/T-Si), and the samples with 10 and 25 nm TiN, referred to as CZTS/10TiN/T-Si and CZTS/25TiN/T-Si, were placed in a mixture of H_2O_2:4 H_2SO_4 (piranha) to remove CZTS and TiN. The effective

minority carrier lifetimes in the Si bottom cells were measured, however, further cleaning in H_2O_2:NH_4OH:5 H_2O (RCA1) and diluted HF (2 %) were performed prior to SIMS characterization. The equivalent samples without the TOPCon configuration, referred to as CZTS/0TiN/Si, CZTS/10TiN/Si and CZTS/25TiN/Si, were all subjected to the same cleaning procedure prior to DLTS and SIMS measurements. Samples with 25 nm TiN and 100 nm Cu, Cu/25TiN/(T-)Si, were also prepared for comparison of Cu in-diffusion from CZTS and pure Cu. A schematic illustration of the TOPCon samples can be seen in Fig. 5.7, where the thickness of SiO_2 and n^+ Poly-Si are 1.5 and 40 nm, respectively.

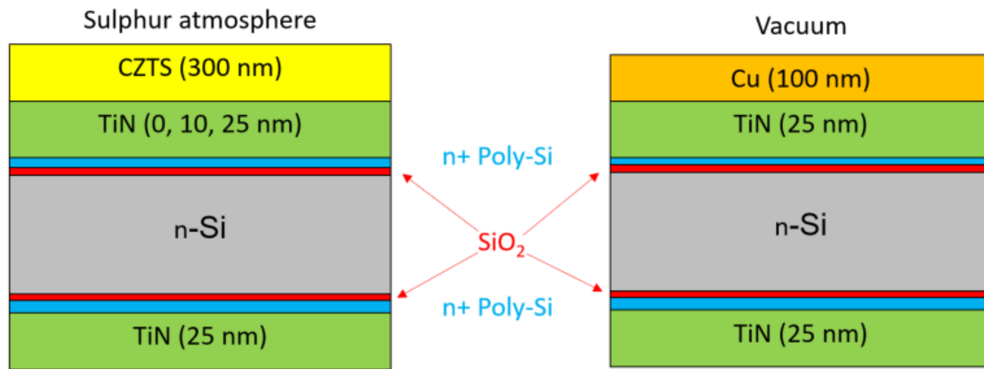

Figure 5.7: Schematic overview of the two types of structures used for the interdiffusion study. Prior to SIMS measurement CZTS/Cu and TiN were etched away in piranha solution, followed by cleaning of the surfaces in RCA1 and HF to remove residuals.

5.2.1 Post-Deposition Etching of CZTS and/or TiN

To investigate the impurity incorporation in the Si bottom cell after CZTS synthesis it is important that both the TiN and/or the CZTS are fully removed. Initial SIMS measurements revealed residuals of TiN at the surface after the piranha etch. This was also supported by Rutherford Backscattering Spectrometry (RBS) of the same samples [62]. The samples were therefore etched in RCA1 solution to remove CZTS/TiN residuals and subsequently dipped in diluted HF to etch any potential oxide layer.

XRD measurements of the samples before, and after the three step cleaning procedure can be seen in Fig. 5.8. After etching, no CZTS and/or TiN related peaks are present, and the absence of CZTS and TiN were further supported by SEM (not included).

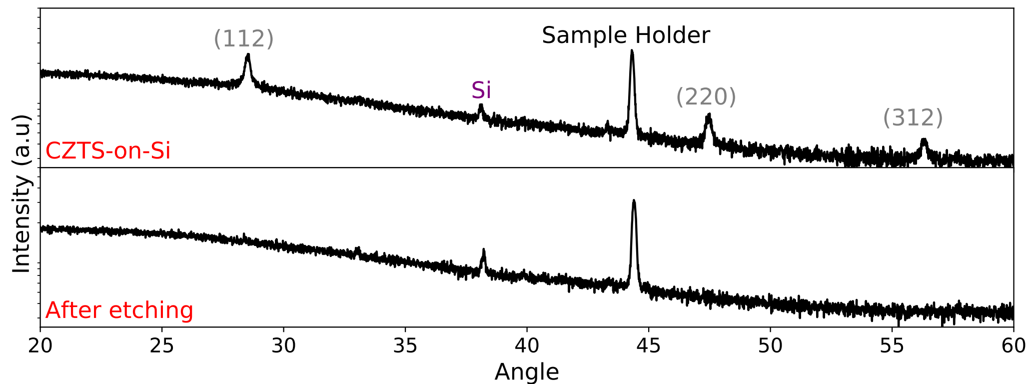

Figure 5.8: XRD measurements of CZTS on Si before (uppermost) and after the three step etching (lower). The CZTS related peaks: (112), (220) and (312) are gone after the etching.

5.2.2 Si with TOPCon - Lifetime Measurements

The effective minority carrier lifetimes in the Si bottom cell with TOPCon at different stages in the tandem processing are presented in Fig. 5.9, and was performed at DTU. The lifetime from the Cu reference is also included for comparison. All samples with TiN and/or CZTS retain above 50 % of the as-passivated lifetime, more than twice of the Cu reference. A significant portion of the decrease occurs during the TiN deposition, as seen in Fig. 5.9. Notably, the decrease in lifetimes occur irrespective of TiN thickness. However, the zoom-in view in the inset in Fig. 5.9 reveal a steeper decrease in lifetime for the sample with no TiN.

The reference sample with a Cu top layer(black line), as depicted in Fig. 5.7, is far more degraded than that of the CZTS samples, as seen in Fig. 5.9. The minority carrier lifetimes in the Cu reference is plotted for different annealing times in Fig. 5.10. Not surprisingly, the lifetime decrease for longer annealing times as more in-diffusion of Cu is expected.

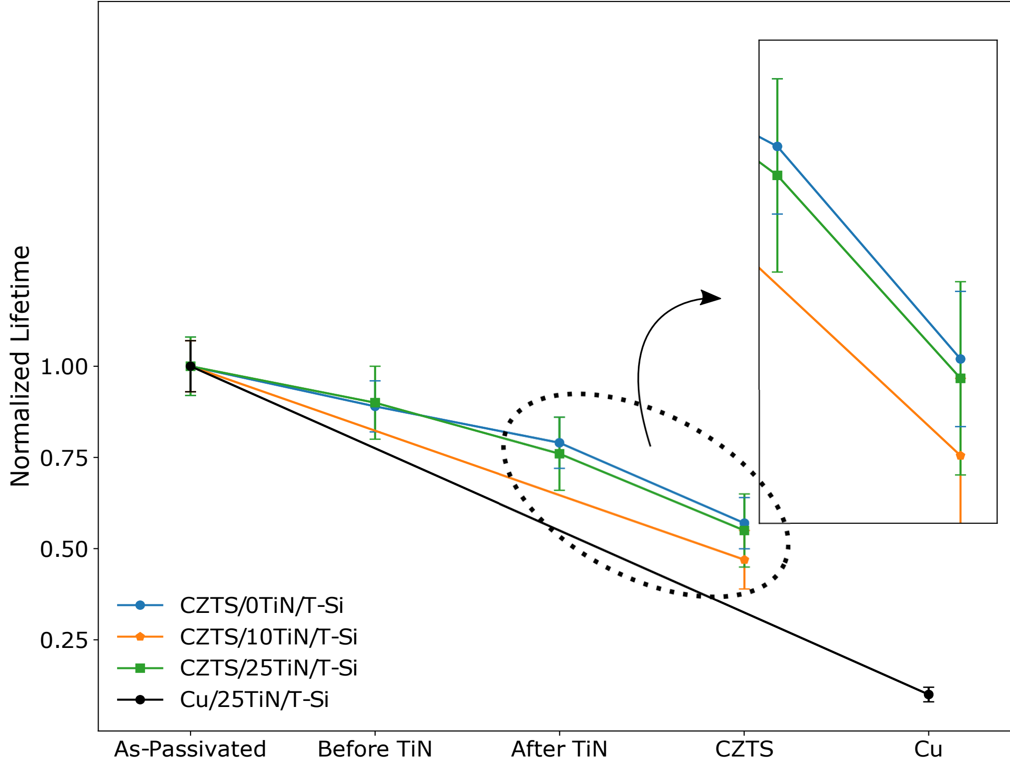

Figure 5.9: Normalized minority carrier lifetimes of all TOPCon samples after the processing steps. The error bars represents the standard deviation of the mean value from the minority carrier lifetime measured with μ-PCD mapping. Inset: Zoom-in view of the decrease in minority carrier lifetime as a result of the CZTS synthesis.

5.2.3 Si with TOPCon - SIMS Results

To evaluate the incorporation of impurities from the CZTS or Cu layer into the TOPCon structure, SIMS depth profiles were performed. In all depth profiles within this section, the backgrounds color indicate the corresponding layer at the depth of which the secondary ions are detected (blue indicate n^+ poly-Si layer, while gray indicate bulk Si). It is assumed that the poly-Si layers are 40 nm and the thin oxide layers are 1.5 nm.

Here, primary beams of both O_2^+ and Cs^+ ions have been employed in order to investigate a wide range of elements. A detailed description of the primary beam ions employed and species detected in the depth profiles

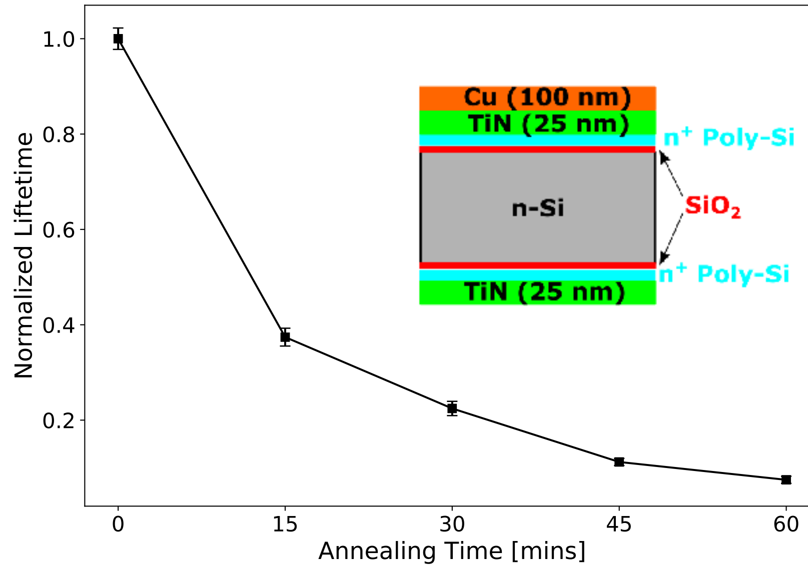

Figure 5.10: Normalized minority carrier lifetimes for the Cu reference samples at different annealing times. The inset shows the structure of the sample.

presented, can be found in Tab. A.1 in Appendix A. In all the TOPCon samples with CZTS, no significant in-diffusion into the mono n-Si takes place for any of the monitored elements in Fig. 5.11. It should be mentioned that the Ti signal detected at the surface of the sample without TiN (blue line in Fig. 5.11b) most likely originates from mass interference with ozone (O_3).

Quantitative depth profiles of Cu in the TOPCon configured Si can be found in Fig. 5.12a. A higher concentration of Cu is observed in the sample without TiN compared to sample with 10 nm TiN. Further, a 25 nm TiN layer makes the structure more resilient to interdiffusion. Interestingly, the n^+ poly-Si layer seems to be working as a gettering site, since a build-up of Cu in this region is observed, and is a well-known and utilized phenomena in Si solar cell processing [63, 64]. The gettering is ascribed the heavy doping and polycrystalline structure in the poly-Si layer (light blue), which increases the solid solubility of Cu relative to that of bulk Si (grey) [65]. As previously mentioned, Cu is a fast diffuser in Si. This is evident from Fig. 5.12b where an accumulation of Cu is present in the polycrystalline layer at the back side, i.e. opposite of the CZTS-deposited side. Notably, the concentration of Cu

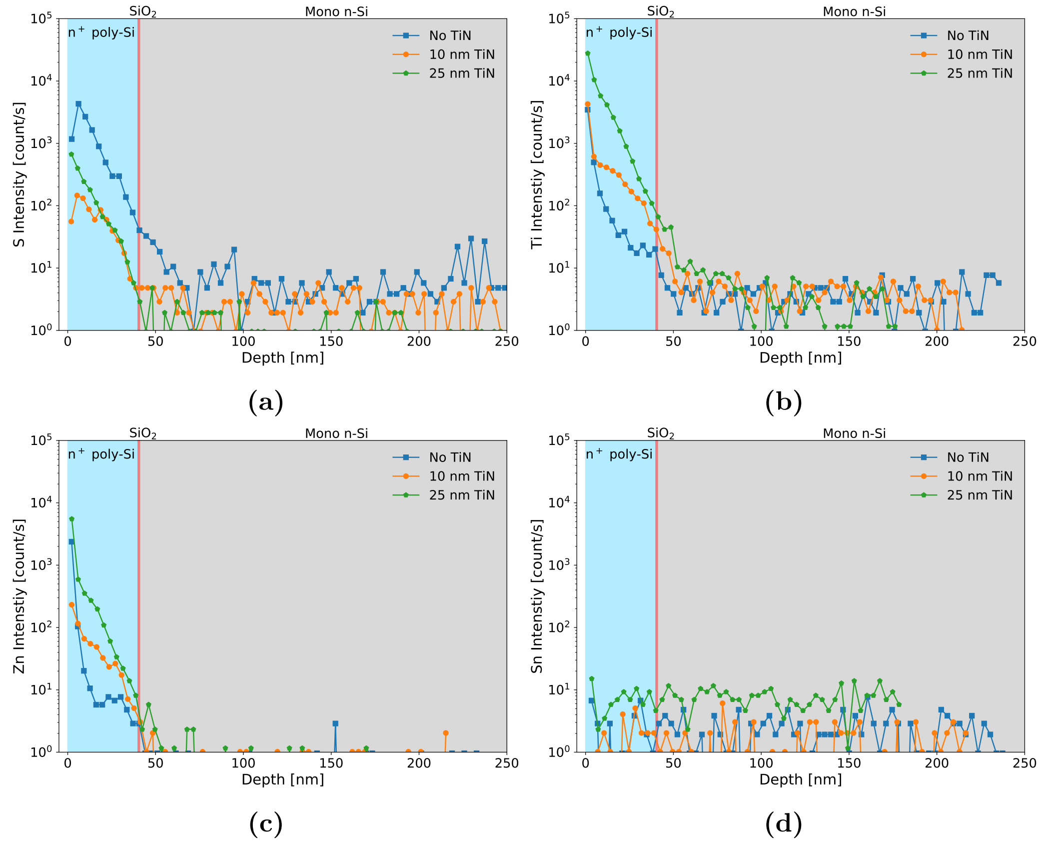

Figure 5.11: Depth profiles from SIMS of elements from CZTS and TiN (not Cu and N) and their potential in-diffusion to the TOPCon Si after CZTS synthesis. There are evidence of (a) S, (b) Ti and (c) Zn in the poly-Si layer, while no (d) Sn is detected in the samples. The TiN layers and/or CZTS layers are removed prior to the SIMS measurements by etching.

on the backside (Fig. 5.12b) is almost one order of magnitude larger than that found at the front side (Fig. 5.12a). However, the measurements are conducted on different days, hence an additional uncertainty can be expected to the ± 10 % error in accuracy following the quantification.

Depth profiles obtained from SIMS of Cu in the Cu/25TiN/T-Si samples are presented in Fig. 5.13. The depth profiles of Cu in the Cu reference samples annealed for 15, 30, 45 and 60 minutes (in vacuum atmosphere) exhibit also a peak in the n$^+$ poly-Si layer, with a steady decrease in concentration in the mono-Si bulk. However, as seen in Fig. 5.13, the concentrations are more than one order of magnitude higher compared to that of the depth

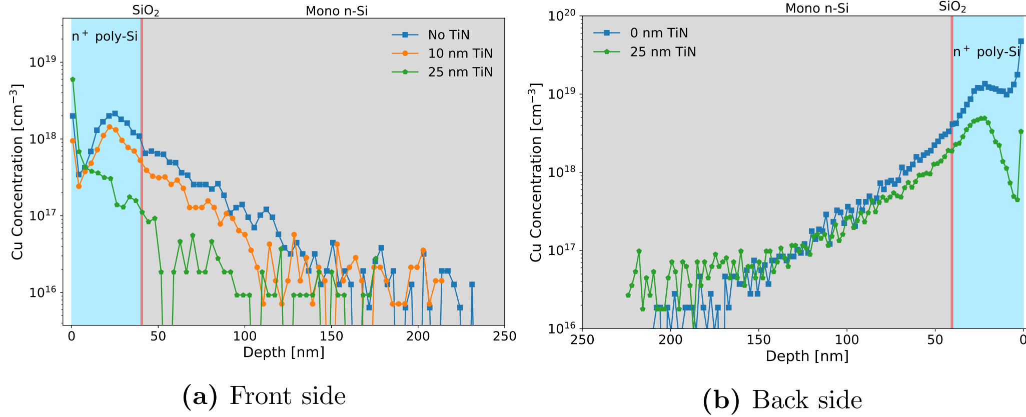

(a) Front side

(b) Back side

Figure 5.12: Depth profiles from SIMS of Cu representing its potential in-diffusion to the TOPCon Si after CZTS synthesis. The TiN diffusion barrier is preventing interdiffusion, with the poly-Si layer, both at the front side (a) and back side (b), working as a segregation site for in-diffused Cu. The TiN layers and Cu layers are removed prior to the SIMS measurements by etching.

profiles in Fig. 5.12a. Additionally, the Cu signal extends farther into the mono-Si layer. The concentration of Cu increases for longer annealing times, which correlates with the decrease in minority carrier lifetime from Fig. 5.10. This is further highlighted in Fig. 5.14, where the relationship between the decrease in minority carrier lifetime and increase in Cu concentration with annealing time is shown. Here, the peak concentrations in the polycrystalline layer are normalized to the peak seen for the 60 minutes annealed sample.

After the heat treatments at 45 and 60 minutes, a brown layer was observed. This is believed to be copper silicide, (Cu_3Si), forming after the longer heat treatments. However, the Cu_3Si seemed to disappear after the three step cleaning procedure described in Sec. 5.2. The formation may have occured due to the the concentration of Cu reaching the solid solubility of Cu in Si. The solid solubility for Cu in n^+ poly-Si is expected to be high, minimum 10^{20} cm^{-3}, based on the peak Cu concentration in the poly-Si layer after the 60 min annealing in Fig. 5.13.

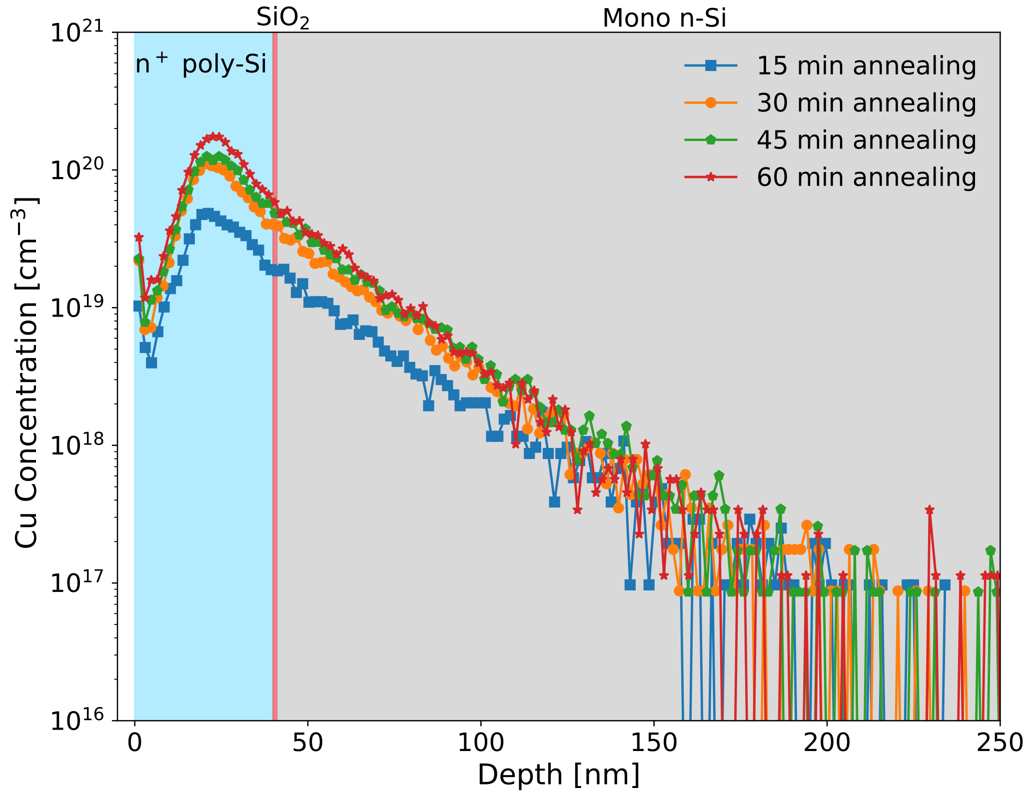

Figure 5.13: Depth profiles from SIMS of Cu in the TOPCon Si after deposition of pure Cu and subsequent annealing. The in-diffusion of Cu is increasing with longer annealing.

5.2.4 Si without TOPCon - SIMS Results

The TOPCon structure, especially with the heavy doped polycrystalline layer, may have great impact on the resilience towards interdiffusion. Depth profiles by SIMS of Cu, Ti and Zn in CZTS-processed Si substrates (without the TOPCon configuration) can be seen in Fig. 5.15. High concentrations/intensities are measured close to the surface, and show an increase of Cu concentration near the surface with increased TiN thickness, as can be seen in Fig. 5.15a. This is opposite to the observed behaviour with a TOPCon structure (Fig. 5.12) where the TiN layer suppressed the incorporation of Cu. However, both Ti and Zn are detected over 100 nm into the bulk of the samples, with a diffusion barrier, before approaching the detection limit

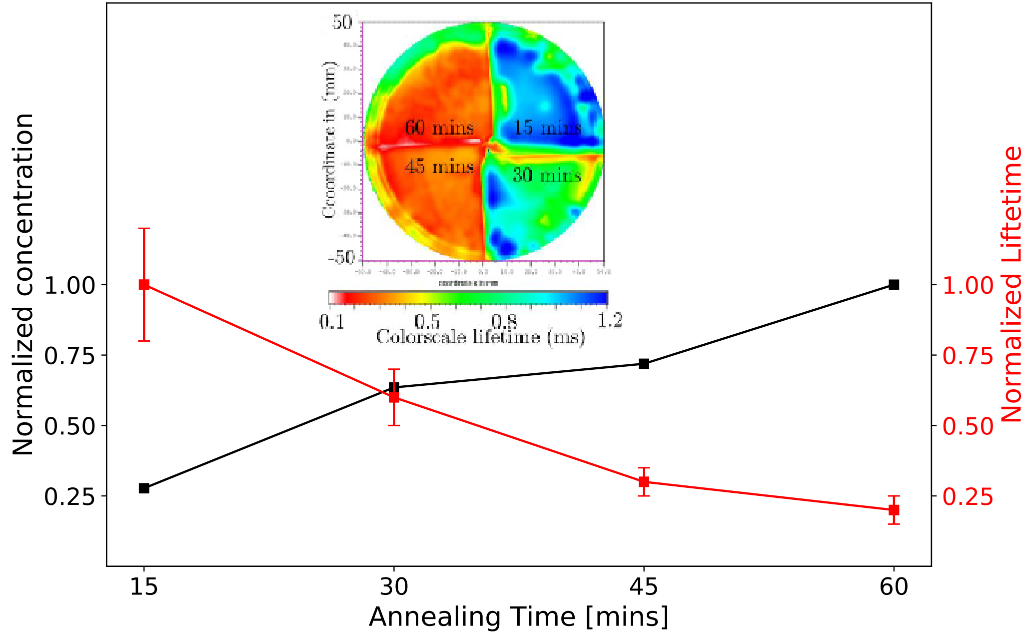

Figure 5.14: Comparison of minority carrier lifetimes with peak Cu concentration normalized to the maximum Cu concentration. Inset: The minority carrier lifetime mapping from μ-PCD measurements of the four samples with different annealing times. The error bars in the minority carrier lifetime results represents the standard deviation of the mean value with an additionally uncertainty representing the location of where the SIMS measurements are conducted.

in the samples. The in-diffusion of Ti exceeds multiple lengths of the initial deposited TiN layer, which makes it unlikely to stem from residuals of TiN on the surface. One explanation may be that the signals detected are due to sputter-induced diffusion [66], where the ion bombardment is causing the element to diffuse into the bulk. However, the interface between the TiN and the moderately doped n-Si may not be too resilient to the high temperature processing and a layer of Cu, Ti and/or Si may be forming at the interface. No visually observed formation of any surface layers were present on the CZTS/(0,10,25)TiN/Si samples. The Si substrates with 25 nm of TiN and 100 nm of pure Cu annealed in 15 minutes had a residual layer still present after the three step etching procedure, thus the obtained SIMS depth profiles are not representative for comparison.

A significant in-diffusion of Cu to the Si substrate without TiN is expected

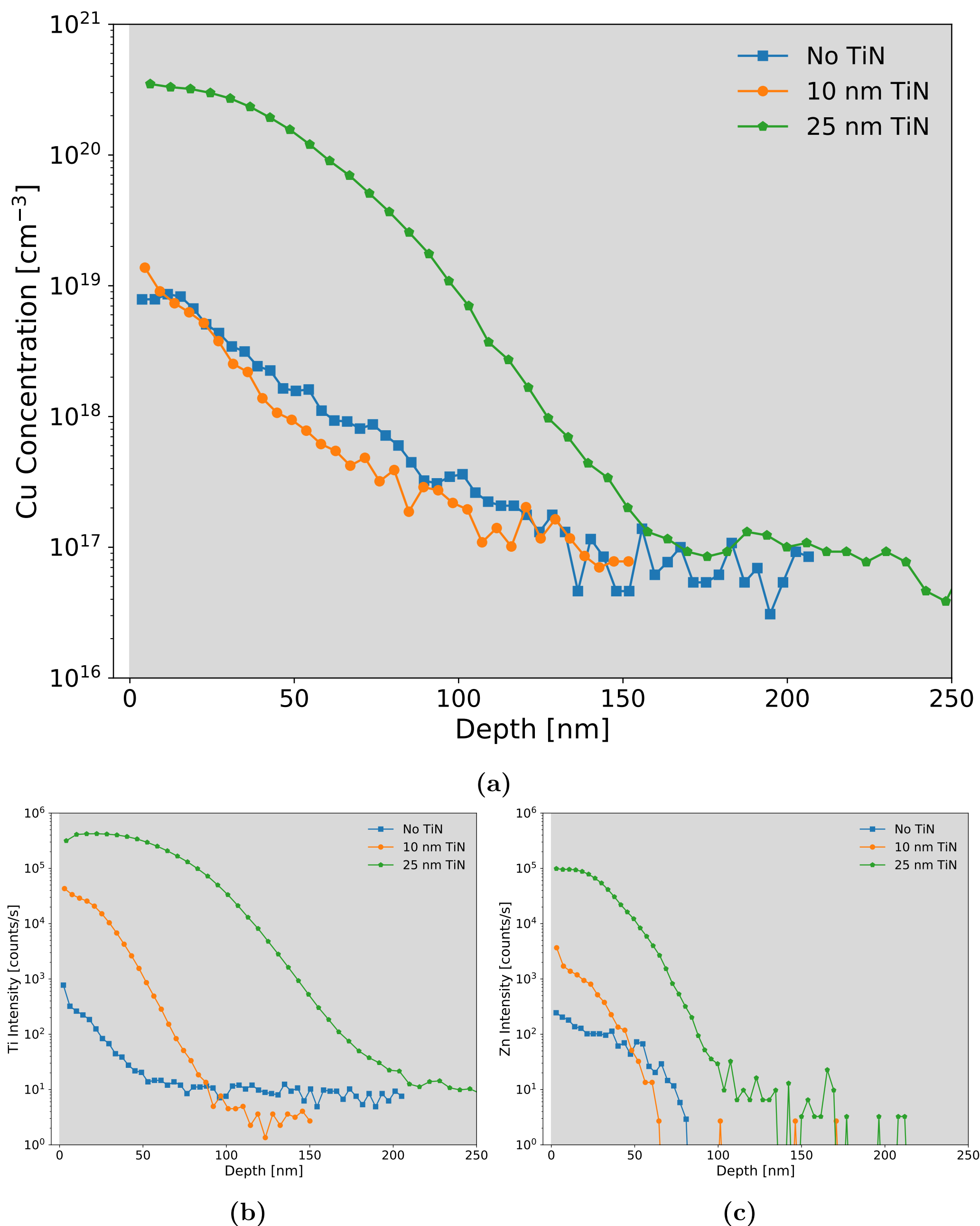

Figure 5.15: Depth profiles from SIMS of (a) Cu, (b) Ti and (c) Zn and their potential in-diffusion to the Si bottom cell after CZTS synthesis. There is clear evidence of all investigated elements in the subsurface Si bottom cell. The TiN layers and/or CZTS layers are removed prior to the SIMS measurements by etching.

from the high surface concentration of Cu measured in Fig. 5.15a. By taking the low solid solubility of Cu in Si into consideration, Cu precipitates may have formed with an inhomogeneous spatial distribution.

5.2.5 Si without TOPCon - DLTS Results

The heavy doped poly-Si is not eligible for making Schottky contacts as this will cause field emission of majority charge carriers. However, Schottky diodes on the CZTS-processed samples without TOPCon were fabricated by depositing Pd contacts by thermal evaporation. The longest rate window from the DLTS measurements of the samples with no TiN, 10 nm and 25 nm TiN diffusion barrier are shown in Fig. 5.16, alongside with the reference silicon wafer. The diodes were kept at -5 V reverse bias and driven

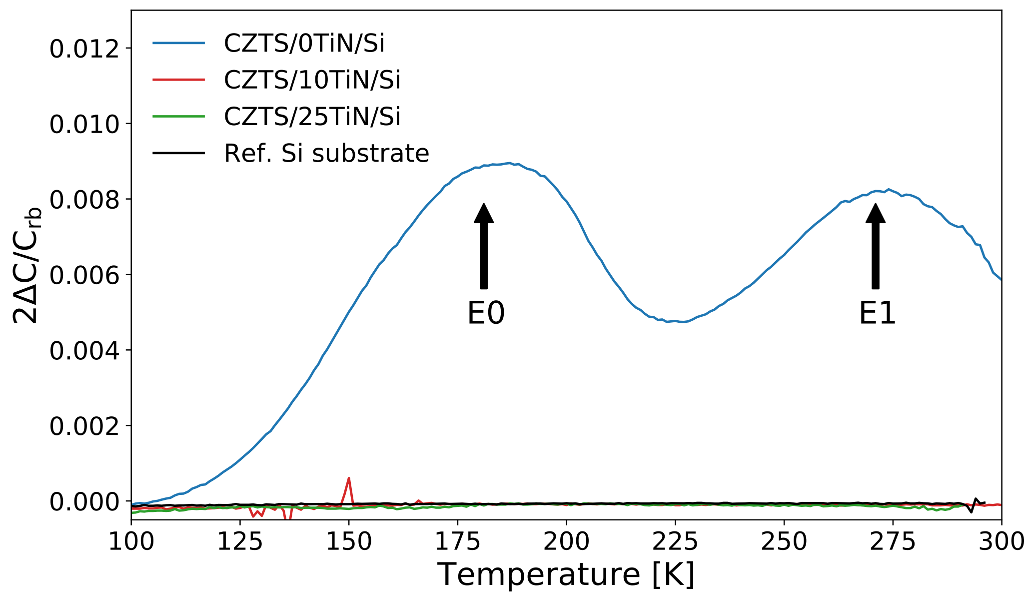

Figure 5.16: DLTS spectra of the samples with different diffusion barrier thickness and a reference as-grown silicon sample. The sample with no TiN shows two broad peaks whereas the lower-temperature peak (E0) shows a shoulder towards lower temperatures.

into forward bias (1 V) during the filling pulse, thus probing the SCR close to the metal-semiconductor interface. As shown in Fig. 5.16, the sample processed with no TiN shows presence of defects not observed in the other

samples (E0 and E1). The activation energy and apparent capture cross section obtained from an Arrhenius plot of E0 are 0.16 eV and 2×10^{-22} cm^2, respectively. This energy level has previosly been reported as interstitial Cu in Si by Istratov *et al.* in [67] and references therein. Both peaks evident in Fig. 5.16 are broad and the peak at lowest temperature contain a shoulder towards lower temperatures. This may originate from extended defects such as dislocations or precipitates [59], or several overlapping defect levels. The signal was also post-processed with a GS4 weighting function in an attempt to resolve several peaks from the broad signatures obtained when applying the lock-in weighting function. The DLTS spectra obtained from both filters can be found in Fig. 5.17 in addition to a simulated DLTS signal using defect signatures from E01, E02 and E1. A third peak is evident in Fig. 5.17, however this is only visible in the sixth rate window. The defects signatures

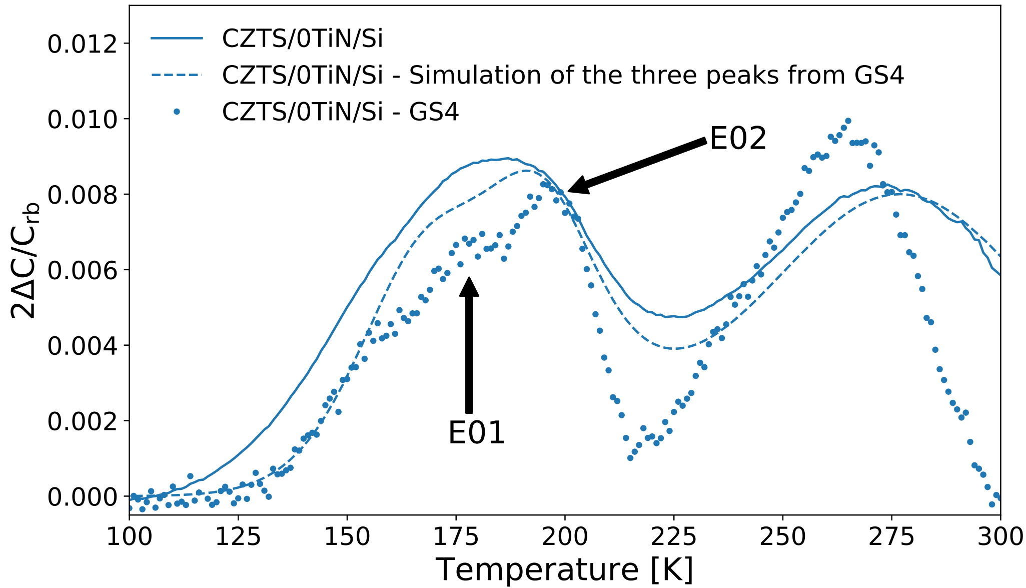

Figure 5.17: DLTS spectra of the sample with no TiN diffusion barrier where the broad peak are resolved by processing the signal with the GS4 weighting function (dots). The defect signatures obtained from the resolved spectrum were used to simulate a DLTS sprectrum with the lock-in weighting function (dashed line).

of E0, E01, E02 and E1 are presented in Tab. 5.2. However, caution must be taken in the physical interpretation of E0, E01 and E02 as the peaks are

hard to decipher and most likely originate from extended defects.

Table 5.2: Defect signatures of all peaks from Fig. 5.16 and Fig. 5.17. However, the peaks in E0, E01 and E02 may originate from extended defects, thus the extracted parameters are non-physical.

Defect ID:	$\mathbf{E_T}$ **[eV]:**	$\sigma_{\mathbf{na}}$ **[cm^2]:**	**Weighting function:**
E0	0.20	1.7×10^{-20}	Lock-in
E1	0.16	2.0×10^{-22}	GS4
E01	0.23	5.0×10^{-20}	GS4
E02	0.16	5.0×10^{-21}	GS4

Several filling pulse voltages were tried and no peaks were observed for $V_p \leq V_{rb}$, as presented in Fig. 5.18. A very small peak can be seen for $V_p = 7$ V, but it did not exhibit any Arrhenius behaviour. The results from Fig.

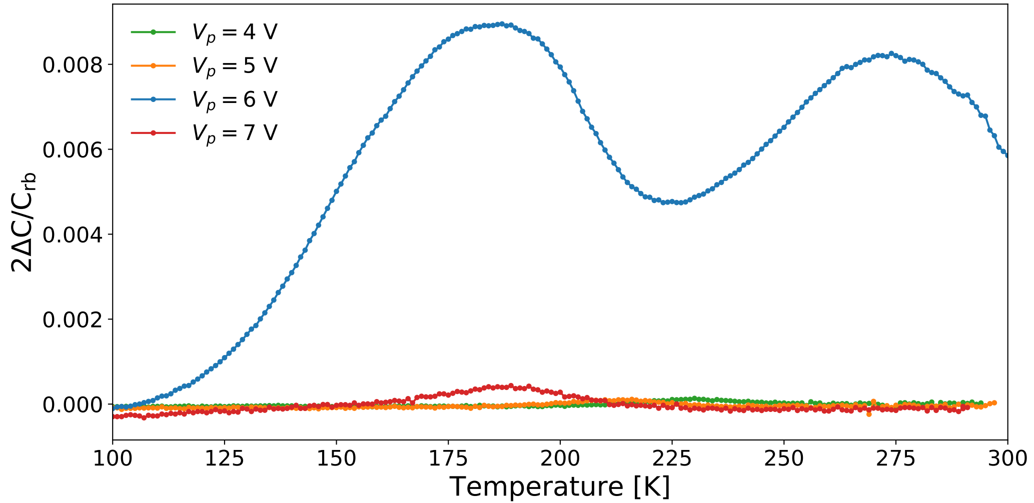

Figure 5.18: DLTS spectrums of the sample with No TiN with different filling pulses (V_p). In the forward bias situation the entire SCR is quenched, hence the interface defects will contribute to the signal.

5.18 indicate that the defects observed are interface states, or located close to the interface. This is further supported from the very low apparent cross sections in Tab. 5.2.

According to the DLTS measurements, a TiN diffusion barrier of 10 nm is sufficient to suppress the formation of electrically active traps in Si after

CZTS processing. Moreover, the nature of the TOPCon structure can be ascribed a gettering site in the Si bottom cell for in-diffused Cu from CZTS. The combination of the TOPCon structure in Si with a 10 nm layer of TiN is promising for fabrication of CZTS-on-Si tandem devices.

5.3 Fabrication of Monolithic Tandem Solar Cells

This section provides the processing and characterization of a working monolithic solar cell of CZTS-on-Si, where the Si bottom cell is configured with TOPCon.

The processing of the bottom cell and deposition of TiN was conducted at DTU before being shipped to UiO. The TOPCon configured Si with TiN was then brought to the Uppsala University where the CZTS synthesis and device making were performed. The final metallization and testing were done in Norway at UiO and IFE, respectively.

5.3.1 Experimental Details

Device areas of 3×3 mm^2 were patterned on an asymmetrically TOPCon configured Si wafer with silicon nitride by PECVD. The processing of the TOPCon configuration is explained in Sec. 3.1. Based on the findings in Sec. 5.2, 10 nm of TiN was deposited by PEALD (see Sec. 3.2.1) to act as a diffusion barrier. As the p^+ poly-Si is easily contaminated, the backside was covered by a 75 nm layer of SiN for protection.

The CZTS films were deposited by co-sputtering as described in Sec. 3.4.2. The Si wafers with TiN and CZTS precursor were placed in a pyrolytic carbon coated graphite box with 70 mg of elemental sulphur, before being placed in a preheated tube furnace for sulphurization. After transferring the graphite box into the hot zone the temperature inside the box reaches 580 °C after 1-2 minutes.

Prior to CdS deposition, the samples were etched in ammonia solution as surface treatment for removal of any secondary phases. Subsequently, 50 nm buffer layers of CdS was deposited by CBD as described in Sec. 3.3. Excess CdS deposited on the backside was removed using hydrochloric acid. Bilayers of i-ZnO/Al:ZnO were deposited by RF sputtering. A process flow of the device fabrication described above can be seen in Fig. 5.19. Before finalizing the devices by depositing Al back contacts by thermal evaporation,

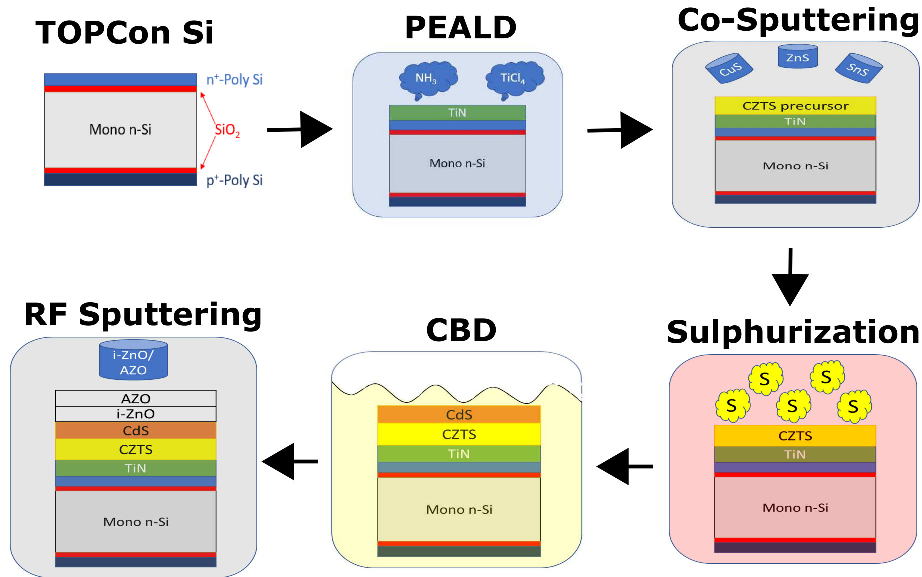

Figure 5.19: Process flow of the device processing of CZTS-on-Si tandem solar cells fabricated in this thesis.

the protective SiN was removed by 6 minutes etching in diluted HF. During the etch the front side (window layer) was protected by a photoresist, which was subsequently removed in acetone. The final cells were defined by scribing by hand with a scalpel to match the predefined cell areas of 3×3 mm^2.

5.3.2 Optimization of the CZTS Deposition on Si

In the initial CZTS synthesis, 500 nm of CZTS precursors were deposited and annealed for either 1 or 13 minutes. To achieve in-diffusion of Na, a slice of SLG was placed directly on top of the CZTS film. The CZTS films in contact with glass substrates were completely peeled off during sulphurization, and those not in contact with glass peeled off after air exposure. To investigate the effect of dwell temperature on peeling, a similar run was conducted with a sulphurization time of 13 minutes and the dwell temperature set to 540 °C. The CZTS film in contact with glass peeled off during sulphurization, while the one not in contact with glass began the peeling some time after air exposure.

Indeed, sputter-deposited films usually contain built-in stress, often re-

lated to mismatch in thermal expansion coefficient, and also expected in the present heterostructure. For example, during crystal growth (sulphurization), certain grains may grow on the expense of smaller grains and cause even more stress in the CZTS film. Several deposition parameters affects the stress in the deposited film, including substrate temperature and chamber pressure. However, due to a time constraint in completing the depositions, a reduction in precursor thickness was considered the most efficient approach of improving the adhesion. CZTS precursors of 300 nm were deposited and successfully annealed (without the presence of glass), for 1 and 13 minutes. A summary of the parameters employed in the synthesis of CZTS absorbers on Si substrates can be found in Tab. B.1 in Appendix B.

5.3.3 Morphology and Crystallinity

Fig. 5.20 shows XRD spectra of the 300 nm thick CZTS, sulphurized in 1 and 13 minutes, deposited on top of Si substrates with TOPCon. The CZTS sulphurized for 1 minute only exhibits the (112) peak, as seen in the lower part of Fig. 5.20, which may be an indication of no kesterite crystallization. The 13 minutes annealed sample, however, show evidence of the (200) peak in the upper part of Fig. 5.20.

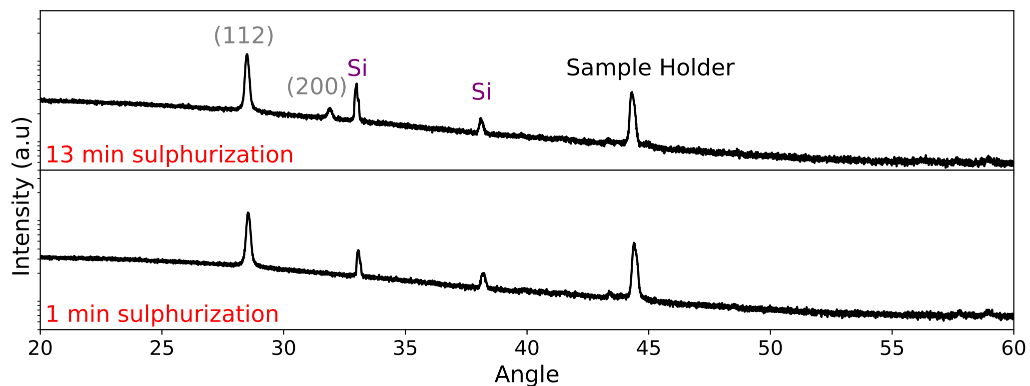

Figure 5.20: XRD measurements of the samples, with different suphurization times, prior to the chemical bath deposition.

Cross-section SEM images of the samples support the XRD results. The sample subjected to the rapid 1 minute sulphurization pictured in Fig. 5.21

shows a lamellar microstructure common for CZTS precursors. The 13

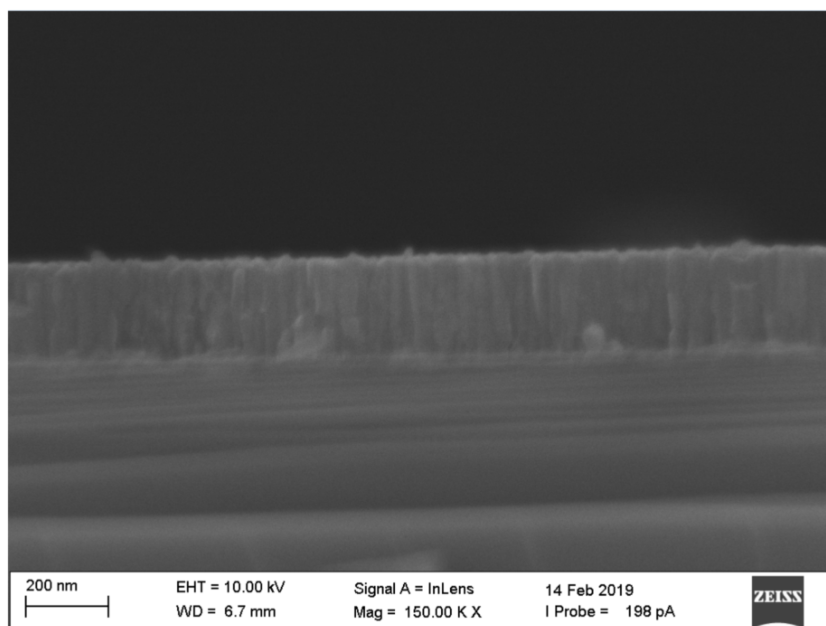

Figure 5.21: SEM image of 300 nm CZTS on Si annealed at 579 °C for 1 min, prior to chemical bath deposition.

minutes sulphurization resulted in larger grain growth, as seen in Fig. 5.22, with a lateral extension close to the CZTS thickness, similar to that expected for a working CZTS thin film absorber.

5.3.4 Device Characterization

Dark and light JV curves were measured with a Newport ABA solar simulator with standard testing conditions (STC) at the facilities of Institute for Energy Technology (IFE).

Diode characteristics of both the 1 minute and the 13 minutes sulphurized tandems, with low illumination, are shown in Fig. 5.23. These results show the establishment of successful rectifying junctions of CZTS deposited on top of TOPCon Si. Both cells exhibit a high leakage current density seen in the reverse bias regime. This is most likely due to a low shunt resistance, and with the low light level (less photo-generated current) its effect is more severe than that of higher illumination. Indeed, it is expected a low shunt resistance

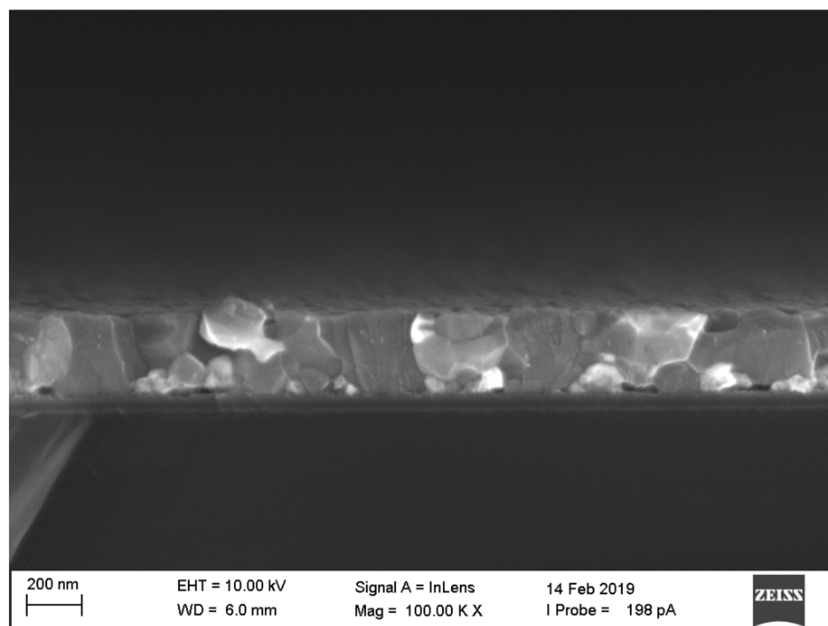

Figure 5.22: SEM image of 300 nm CZTS on Si annealed at 580 °C for 13 min, prior to chemical bath deposition.

as the JV curves are measured by probing directly on to the window layer (no metal contacts). However, a voltage-dependent generation current may also be responsible for the deviation from a constant leakage current in reverse bias.

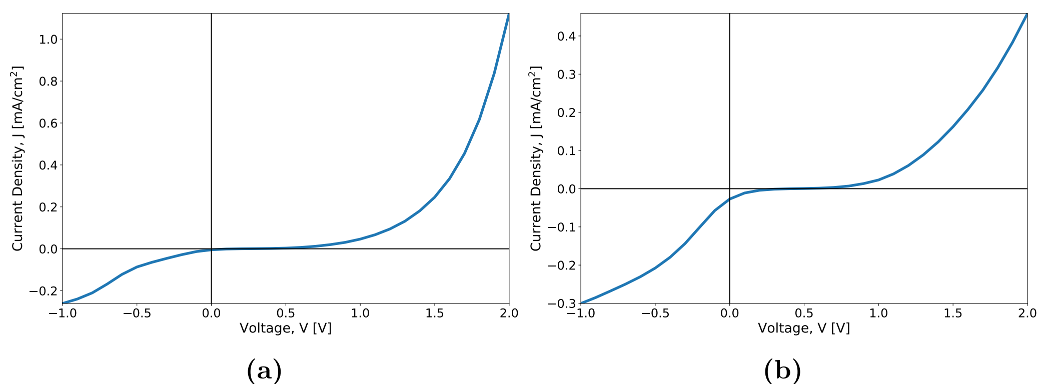

Figure 5.23: JV curves of the tandem solar cells with 300 nm of CZTS sulphurized for (a) 1 minute and (b) 13 minutes.

Successful light JV curves of the two tandems can be seen Fig. 5.24 prov-

ing that tandem solar cells of CZTS-on-Si can be fabricated experimentally. The light JV-characteristics with STC of the 1 minute annealed sample in Fig. 5.24a shows poor J_{sc} and V_{oc} with an negligible efficiency. The device subjected to full sulphurization (13 minutes), however, display a JV curve resembling that of a pn diode, see Fig. 5.24b. The tandem device exhibits a V_{oc} over 800 mV, higher than the two cells individually (with STC) and the highest reported for CZTS/Si tandem cells. The JV curve is highly distorted, which are one of more factors causing the poor conversion efficiency of 0.24 %.

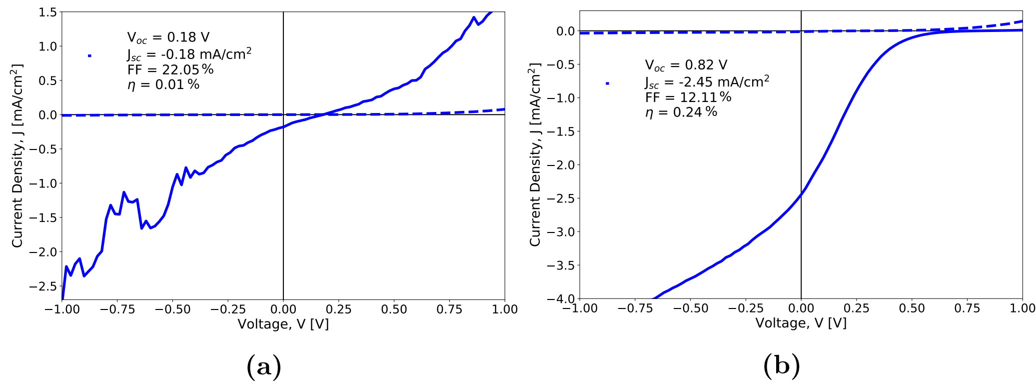

Figure 5.24: Light (solid) and dark (dashed) JV curves of the tandem solar cells with 300 nm of CZTS sulphurized for (a) 1 minute and (b) 13 minutes.

5.3.5 Discussion

As previously addressed, devices of Si with TOPCon have achieved a V_{oc} close to 740 mV. However, after the TiN and CZTS processing the minority carrier lifetime in Si is degraded and thus a decreased implied V_{oc} is expected. By taking this into consideration, the measured V_{oc} of 820 mV must contain a solid contribution from the CZTS top cell. The demonstration of this additive effect of V_{oc} was intended one of the main objectives in this thesis.

Both devices including the rapid 1 minute sulphurized CZTS produced working tandem solar cells. The performance of 0.24 %, however, is poor compared to single junction cells. This can be related to lack of crystallinity seen from the XRD measurement in Fig. 5.20 and cross-section view image

in Fig. 5.21 from SEM. Recently, Larsen *et al.* achieved a record high V_{oc} of 809 mV for single-junction CZTS where the CZTS was subjected to the same rapid sulphurization (1 minute) as attempted here. However, cross-section images from transmission electron microscopy (TEM) reveal a crystallization of small grains. The poor crystallization in Fig. 5.21 may be due to the absence of alkalis, the reduced thickness and/or the absent air annealing prior to CdS deposition. One may argue that the grains observed in Fig. 5.22 are smaller than usually observed in CZTS on Mo-coated SLG, whereas the factors mentioned above applies.

The distortion observed in the JV curve in Fig. 5.24b has been previously reported, both in tandem and single-junction thin films. This so-called "rollover" effect is often associated with current-mismatching in tandems [68] and current blocking. The latter arises from non-optimized interfaces with presence of reverse Schottky contacts. Here, it is likely that the rollover effect originate from current-mismatching of the two cells with the CZTS as the limiting cell. However, the same effect has been reported in CIGS deposited on substrates not containing alkali elements [69]. Here, the origin of this effect was assigned a non-ohmic behaviour at the Mo interface which dissapeared when incorporating Na in the CIGS. The rollover effect has also been observed in single-junction CZTS devices, and solved by surface treatment of KCN etching [41].

CHAPTER 6

Summary

Band gap grading by incorporation of Ge in CZTS and the potential interdiffusion of impurities from CZTS in to Si bottom cell during CZTS processing have been investigated. The compatibility of CZTS as top cell in monolithically-integrated Si-based tandem solar cells has been proven experimentally. This has been done through fabrication of working CZTS-on-Si tandem solar cells. The successful devices were achieved by employing findings from SIMS, DLTS and minority carrier lifetime measurements of intermediate structures, in the final tandem fabrication.

6.1 Conclusion

Most of today's PV technology is based on the semiconductor, silicon. Single-junction Si solar cells are limited to efficiencies below 30 % according to the Shockley-Queissier limit. This thesis has assessed the possibility of the thin film chalcogenide, CZTS, as top cell in Si-based tandem solar cells using TOPCon Si as the bottom cell.

Depth profile techniques have been used to study the incorporation of Ge in CZTS to achieve the optimum band gap for a top cell in Si-based tandem solar cells. A comparison of depth profiles from GDOES and SIMS revealed how the combination of the two techniques can be used in excluding potential matrix effects in SIMS measurements.

The use of a thin diffusion barrier of TiN has been investigated to avoid

contamination of the Si bottom cell from the CZTS synthesis. Depth profiles obtained from SIMS of metallic and chalcogen impurities of the post CZTS-processed Si bottom cell revealed how the heavy phosphorous-doped polycrystalline layer from the TOPCon Si structure can be ascribed as a gettering site for Cu in Si. Measurements from SIMS and DLTS showed that the TiN diffusion barrier suppressed the in-diffusion of Cu, and other detrimental impurities, to the Si bottom cell.

The combination of TOPCon Si with a TiN diffusion barrier is proven compatible with a 300 nm layer of CZTS as top cell in a working CZTS-on-Si tandem solar cell. The full fabrication of the above device, with 10 nm of TiN, resulted in an additive V_{oc} of more than 800 mV, higher than that of CZTS and TOPCon Si individually. These results provide a solid foundation for the development of the next generation CZTS-on-Si tandem solar cells.

6.2 Suggestions for Further Work and Improvements

As this thesis was intended as a "proof-of-concept" dedicated CZTS-on-Si tandem solar cells, it returned several ideas for paths towards further improvements. In particular, the efficiency may be improved substantially by optimizing the current-matching between the layers.

The investigation of TiN as a diffusion barrier was reserved as a diffusion study. Although it has been successfully employed, the electrical properties of the TiN interfaces were not characterized and may not be optimized. The presence of reverse Schottky contacts will limit the total current extraction and should be thoroughly investigated by preparing intermediate structures of TiN on top of TOPCon Si and CZTS, separately. For example, tuning the structural and electrical properties via controlling the oxygen content, including oxynitride alloying, may be a viable path for further improvements.

The CZTS absorbers used as the top cell in the tandem devices had non-optimum band gaps (no incorporation of Ge), thus the absorption of the incident photons are not fully utilized. The current produced in the CZTS

is dependent of the thickness, hence the current-mismatching may have been enhanced by the thin CZTS layers deposited. Research dedicated the growth of CZTGS on Si with optimized thickness should be investigated to reduce the current-mismatch in the device.

The presence of alkali elements is an important contributor for high-quality CZTS and CIGS devices [70]. As the contact with SLG corrupted the adhesion of CZTS on Si, with TiN, investigations with NaF-deposited CZTS, with different thicknesses of NaF, should be conducted for improved crystallization and thus (potentially) device performance. The incorporation of other alkali elements should also be investigated, e.g. potassium (K) doping of CIGS by KF post deposition treatment has proven to enhance the device efficiency [71]. Here, a dedicated diffusion study of alkali elements by SIMS is necessary to investigate the distribution of the alkali element and any potential out-diffusion from the CZTS top cell.

The fabrication performed in this work included many processing steps, whereas several of the them were not optimized for the studied structure. Hopefully, the positive result of this work can lead to a more comprehensive study on optimizing these processing steps for the fabrication of CZTS-on-Si tandem solar cells. Further, post-deposition annealing has led to improved device performance [72]. A study on post-deposition air annealing at different temperatures should be investigated, and possibly annealing in other ambient atmospheres. The fabricated devices in this work were subjected to ammonia etching following the sulphurization. Other surface treatments may be more effective for the removal of secondary phases and thus potentially improve the device efficiency, e.g. the more common surface treatment by KCN etching should be explored. Moreover, a study on the formation of secondary phases in CZTS grown on Si substrates would be useful in such a study.

Bibliography

[1] International Energy Agency. *World energy outlook 2018*. 2018.

[2] SolarPower Europe. *Global Market Outlook 2018-2022*. 2018.

[3] M. A. Green et al. "Solar cell efficiency tables (Version 53)". In: *Progress in Photovoltaics: Research and Applications* 27.1 (2019), pp. 3–12. DOI: 10.1002/pip.3102.

[4] K. Ito. *Copper Zinc Tin Sulfide-Based Thin Film Solar Cells*. John Wiley & Sons, Ltd., 2015.

[5] R. J. D. Tilley. *Understanding solids: the science of materials*. John Wiley & Sons, Ltd., 2004. ISBN: 0 470 85275 5.

[6] C. Kittel. *Introduction to solid state physics*. John Wiley & Sons, Inc., 2005. ISBN: 0 471 41526 8.

[7] S. A. Campbell. *Fabrication enginnering at the micro- and nanoscale*. Oxford University Press, 2013. ISBN: 9780199861224.

[8] A. Fick. "Ueber Diffusion". In: *Annalen der Physik* 170.1 (1855), pp. 59–86. DOI: 10.1002/andp.18551700105.

[9] C. M. Sutter-Fella et al. "Sodium Assisted Sintering of Chalcogenides and Its Application to Solution Processed Cu2ZnSn(S,Se)4 Thin Film Solar Cells". In: *Chemistry of Materials* 26.3 (2014), pp. 1420–1425. DOI: 10.1021/cm403504u.

[10] S. Haass et al. "Complex Interplay between Absorber Composition and Alkali Doping in High-Efficiency Kesterite Solar Cells". In: *Advanced Energy Materials* 8 (Oct. 2017), p. 1701760. DOI: 10.1002/aenm.201701760.

[11] A. Laemmle et al. “Investigation of the diffusion behavior of sodium in Cu(In,Ga)Se2 layers”. In: *Journal of Applied Physics* 115.15 (2014), p. 154501. DOI: 10.1063/1.4871457.

[12] R. Wuerz, W. Hempel and P. Jackson. “Diffusion of Rb in polycrystalline Cu(In,Ga)Se2 layers and effect of Rb on solar cell parameters of Cu(In,Ga)Se2 thin-film solar cells”. In: *Journal of Applied Physics* 124.16 (2018), p. 165305. DOI: 10.1063/1.5044629.

[13] S. Grini et al. “Low temperature incorporation of selenium in Cu2ZnSnS4: Diffusion and nucleation”. In: *Thin Solid Films* 665 (Sept. 2018). DOI: 10.1016/j.tsf.2018.09.024.

[14] S. P. Harvey, I. Repins and G. Teeter. “Defect chemistry and chalcogen diffusion in thin-film Cu2ZnSnSe4 materials”. In: *Journal of Applied Physics* 117.7 (2015), p. 074902. DOI: 10.1063/1.4907951.

[15] B. G. Streetman and S. K. Banerjee. *Solid state electronic devices*. Pearson, 2014. ISBN: 978-0133356038.

[16] D. K. Schroder. *Semiconductor material and device characterization*. John Wiley & Sons, Inc., 2006. ISBN: 978-0-471-73906-7.

[17] P. Blood and J.W. Orton. *The Electrical Characterization of Semiconductors: Majority Carriers and Electron States*. Academic Press, 1992. ISBN: 0-12-528627-9.

[18] J. Nelson. *The physics of solar cells*. Imperial College Press, 2003. ISBN: 978-1-86094-349-2.

[19] D. M. Chapin, C. S. Fuller and G. L. Pearson. “A New Silicon p-n Junction Photocell for Converting Solar Radiation into Electrical Power”. In: *Journal of Applied Physics* 25.5 (1954), pp. 676–677. DOI: 10.1063/1.1721711.

[20] W. Shockley and H. J. Queisser. “Detailed Balance Limit of Efficiency of p-n Junction Solar Cells”. In: *Journal of Applied Physics* 32.3 (1961). DOI: 10.1063/1.1736034.

[21] A. De Vos. “Detailed balance limit of the efficiency of tandem solar cells”. In: *Journal of Physics D: Applied Physics* 13.5 (May 1980), pp. 839–846. DOI: 10.1088/0022-3727/13/5/018.

[22] F. Feldmann et al. “Passivated rear contacts for high-efficiency n-type Si solar cells providing high interface passivation quality and excellent transport characteristics”. In: *Solar Energy Materials and Solar Cells* 120 (2014), pp. 270–274. DOI: https://doi.org/10.1016/j.solmat.2013.09.017.

[23] R. Peibst et al. “Working principle of carrier selective poly-Si/c-Si junctions: Is tunnelling the whole story?” In: *Solar Energy Materials and Solar Cells* 158 (2016), pp. 60–67. DOI: https://doi.org/10.1016/j.solmat.2016.05.045.

[24] A. Richter et al. “Tunnel oxide passivating electron contacts as full-area rear emitter of high-efficiency p-type silicon solar cells”. In: *Progress in Photovoltaics: Research and Applications* 26.8 (2018). DOI: 10.1002/pip.2960.

[25] F. Haase et al. “Laser contact openings for local poly-Si-metal contacts enabling 26.1%-efficient POLO-IBC solar cells”. In: *Solar Energy Materials and Solar Cells* 186 (2018), pp. 184–193. DOI: https://doi.org/10.1016/j.solmat.2018.06.020.

[26] R. Cariou et al. “III–V-on-silicon solar cells reaching 33% photoconversion efficiency in two-terminal configuration”. In: *Nature Energy* 3.4 (2018). DOI: 10.1038/s41560-018-0125-0.

[27] F. Sahli et al. “Fully textured monolithic perovskite/silicon tandem solar cells with 25.2% power conversion efficiency”. In: *Nature Materials* 17.9 (2018). DOI: 10.1038/s41563-018-0115-4.

[28] S. Chen et al. “Crystal and electronic band structure of Cu2ZnSnX4 (X=S and Se) photovoltaic absorbers: First-principles insights”. In: *Applied Physics Letters* 94.4 (2009), p. 041903. DOI: 10.1063/1.3074499.

[29] S. Schorr, H.-J. Hoebler and M. Tovar. “A neutron diffraction study of the stannite-kesterite solid solution series”. In: *European Journal of Mineralogy* 19 (Feb. 2007). DOI: 10.1127/0935-1221/2007/0019-0065.

[30] K. Momma and F. Izumi. “*VESTA3* for three-dimensional visualization of crystal, volumetric and morphology data”. In: *Journal of Applied Crystallography* 44.6 (Dec. 2011), pp. 1272–1276. DOI: 10.1107/S0021889811038970.

[31] J. J. S. Scragg et al. “Cu–Zn disorder and band gap fluctuations in Cu2ZnSn(S,Se)4: Theoretical and experimental investigations”. In: *physica status solidi (b)* 253.2 (2016), pp. 247–254. DOI: 10.1002/pssb.201552530.

[32] N. Song et al. “Study of sputtered Cu2ZnSnS4 thin films on Si”. In: *Applied Surface Science* 459 (2018), pp. 700–706. DOI: https://doi.org/10.1016/j.apsusc.2018.07.192.

[33] N. Song et al. “Epitaxial Cu2ZnSnS4 thin film on Si (111) substrate”. In: *Applied Physics Letters* 106.25 (2015), p. 252102. DOI: 10.1063/1.4922992.

[34] H. Katagiri et al. “Enhanced Conversion Efficiencies of Cu2ZnSnS4-Based Thin Film Solar Cells by Using Preferential Etching Technique”. In: *Applied Physics Express* 1 (2008), p. 041201. DOI: 10.1143/apex.1.041201.

[35] K. Maeda et al. “Dependence on Annealing Temperature of Properties of Cu2ZnSnS4 Thin Films Prepared by Sol-Gel Sulfurization Method”. In: *Japanese Journal Of Applied Physics* 50.1 (2011). DOI: 10.1143/jjap.50.01be10.

[36] A.V. Moholkar et al. “Synthesis and characterization of Cu2ZnSnS4 thin films grown by PLD: Solar cells”. In: *Journal of Alloys and Compounds* 509.27 (2011), pp. 7439–7446. DOI: https://doi.org/10.1016/j.jallcom.2011.04.074.

[37] W. Wang et al. “Device Characteristics of CZTSSe Thin-Film Solar Cells with 12.6% Efficiency”. In: *Advanced Energy Materials* 4.7 (2014), p. 1301465. DOI: 10.1002/aenm.201301465.

[38] B.-T. Jheng, Po-Tsun Liu and Meng-Chyi Wu. “A promising sputtering route for dense Cu2ZnSnS4 absorber films and their photovoltaic performance”. In: *Solar Energy Materials and Solar Cells* 128 (2014), pp. 275–282. DOI: https://doi.org/10.1016/j.solmat.2014.05.033.

[39] C.-Y. Liu et al. “Sodium Passivation of the Grain Boundaries in CuInSe 2 and Cu 2 ZnSnS 4 for High-Efficiency Solar Cells”. In: *Advanced Energy Materials* 7 (Dec. 2016), p. 1601457. DOI: 10.1002/aenm.201601457.

[40] I. Grozdanov and M. Najdoski. “Optical and Electrical Properties of Copper Sulfide Films of Variable Composition”. In: *Journal of Solid State Chemistry* 114.2 (1995), pp. 469–475. DOI: https://doi.org/10.1006/jssc.1995.1070.

[41] M. Buffière et al. “KCN Chemical Etch for Interface Engineering in Cu2ZnSnSe4 Solar Cells”. In: *ACS Applied Materials & Interfaces* 7.27 (2015), pp. 14690–14698. DOI: 10.1021/acsami.5b02122.

[42] H. Katagiri et al. “The Influence of the Composition Ratio on CZTS-based Thin Film Solar Cells”. In: *MRS Proceedings* 1165 (2009), 1165–M04–01. DOI: 10.1557/PROC-1165-M04-01.

[43] P.E. Agbo, P.A. Nwofe and L.O. Odo. “Analysis on energy bandgap of zinc sulphide (ZnS) thin films grown by solution growth technique”. In: *Chalcogenide Letters* 14 (Aug. 2017), pp. 357–363.

[44] H. Ferhati and F. Djeffal. “Graded band-gap engineering for increased efficiency in CZTS solar cells”. In: *Optical Materials* 76 (2018), pp. 393–399. DOI: https://doi.org/10.1016/j.optmat.2018.01.006.

[45] K. Woo et al. “Band-gap-graded Cu2ZnSn(S1-x,Sex)4 Solar Cells Fabricated by an Ethanol-based, Particulate Precursor Ink Route”. In: *Scientific reports* 3 (Oct. 2013), p. 3069. DOI: 10.1038/srep03069.

[46] S. Zamulko, R. Chen and C. Persson. “Investigation of the structural, optical and electronic properties of Cu2Zn(Sn,Si/Ge)(S/Se)4 alloys for solar cell applications”. In: *physica status solidi (b)* 254.6 (2017), p. 1700084. DOI: 10.1002/pssb.201700084.

[47] G. Chen et al. “Bandgap engineering of Cu2ZnSn1-xGexS(e)4 by adjusting Sn-Ge ratios for almost full solar spectrum absorption”. In: *Journal of Alloys and Compounds* 718 (2017), pp. 236–245. DOI: https://doi.org/10.1016/j.jallcom.2017.05.150.

[48] A. E. Kaloyeros and E. Eisenbraun. “Ultrathin Diffusion Barriers/Liners for Gigascale Copper Metallization”. In: *Annual Review of Materials Science* 30.1 (2000), pp. 363–385. DOI: 10.1146/annurev.matsci.30.1.363.

[49] C. Lee and Yu-Lin Kuo. “The evolution of diffusion barriers in copper metallization”. In: *JOM* 59.1 (2007), pp. 44–49. DOI: 10.1007/s11837-007-0009-4.

[50] S. Englund et al. “Characterization of TiN back contact interlayers with varied thickness for Cu2ZnSn(S,Se)4 thin film solar cells”. In: *Thin Solid Films* 639 (2017), pp. 91–97. DOI: https://doi.org/10.1016/j.tsf.2017.08.030.

[51] J. B. Heng et al. “23% High-Efficiency Tunnel Oxide Junction Bifacial Solar Cell With Electroplated Cu Gridlines”. In: *IEEE Journal of Photovoltaics* 5 (Jan. 2015), pp. 82–86. DOI: 10.1109/JPHOTOV.2014.2360565.

[52] F. Feldmann et al. “The application of poly-Si/SiOx contacts as passivated top/rear contacts in Si solar cells”. In: *Solar Energy Materials and Solar Cells* 159 (2017), pp. 265–271. DOI: https://doi.org/10.1016/j.solmat.2016.09.015.

[53] T. Kääriäinen et al. *Atomic Layer Deposition: Principles, Characteristics, and Nanotechnology Applications, Second Edition*. Wiley, 2013. ISBN: 9781118747407.

[54] A. Majid and M. Bibi. *Cadmium based II-VI Semiconducting Nanomaterials*. Springer, 2018. ISBN: 9783319687537.

[55] P. van der Heide. *Secondary Ion Mass Spectrometry: an Introduction to Principles and Practices*. John Wiley & Sons, Inc., 2014. ISBN: 978-1-118-48048-9.

[56] M. Birkholz. *Thin Film Analysis by X-Ray Scattering*. Wiley-VCH, 2006. ISBN: 3-527-31052-5.

[57] T. Nelis, R. Payling and N. W. Barneet. *Glow Discharge Optical Emission Spectroscopy: A Practical Guide*. The Royal Society of Chemistry, 2003. ISBN: 978-0-85404-521-1.

[58] D. V. Lang. "Deep-level transient spectroscopy: A new method to characterize traps in semiconductors". In: *Journal of Applied Physics* 45.7 (1974), pp. 3023–3032.

[59] W. Schröter et al. "Bandlike and localized states at extended defects in silicon". In: *Physical review. B, Condensed matter* 52 (Dec. 1995), pp. 13726–13729. DOI: `10.1103/PhysRevB.52.13726`.

[60] Y. Leng. *Materials Characterization: Introduction to Microscopic and Spectroscopic Methods, Second Edition*. Wiley-VCH, 2013. ISBN: 9783527334636.

[61] Y. Gao et al. "On the SIMS depth profiling analysis: reduction of matrix effect". In: *International Journal of Mass Spectrometry and Ion Processes* 143 (1995), pp. 11–18. DOI: `https://doi.org/10.1016/0168-1176(94)04113-L`.

[62] A. Hajijafarassar et al. "Monolithic two-terminal tandem solar cell potential of Thin Film Chalcogeni-des on TOPCon Si". Forthcoming.

[63] J. S. Kang and D. K. Schroder. "Gettering in silicon". In: *Journal of Applied Physics* 65.8 (1989), pp. 2974–2985. DOI: `10.1063/1.342714`.

[64] D. Macdonald et al. "Phosphorus gettering in multicrystalline silicon studied by neutron activation analysis". In: *Conference Record of the Twenty-Ninth IEEE Photovoltaic Specialists Conference, 2002.* 2002, pp. 285–288. DOI: `10.1109/PVSC.2002.1190514`.

[65] A. A. Istratov and Eicke R. Weber. "Physics of Copper in Silicon". In: *Journal of The Electrochemical Society* 149 (Jan. 2002), G21–G30. DOI: 10.1149/1.1421348.

[66] M. A. Makeev and A.-L. Barabasi. "Ion-Induced Surface Diffusion in Ion Sputtering". In: *Applied Physics Letters* 71 (Jan. 1997). DOI: 10.1063/1.120140.

[67] A.A. Istratov and E.R. Weber. "Electrical properties and recombination activity of copper, nickel and cobalt in silicon". In: *Applied Physics A* 66.2 (Feb. 1998), pp. 123–136. DOI: 10.1007/s003390050649.

[68] M. Schnabel et al. "Monolithic Si nanocrystal/crystalline Si tandem cells involving Si nanocrystals in SiC". In: *Progress in Photovoltaics: Research and Applications* 24.9 (2016), pp. 1165–1177. DOI: 10.1002/pip.2766.

[69] R. Caballero et al. "Influence of Na on Cu(In,Ga)Se2 solar cells grown on polyimide substrates at low temperature: Impact on the Cu(In,Ga)Se2/Mo interface". In: *Applied Physics Letters* 96.9 (2010), p. 092104. DOI: 10.1063/1.3340459.

[70] P.M.P. Salomé, H. Rodriguez-Alvarez and S. Sadewasser. "Incorporation of alkali metals in chalcogenide solar cells". In: *Solar Energy Materials and Solar Cells* 143 (2015), pp. 9–20. DOI: https://doi.org/10.1016/j.solmat.2015.06.011.

[71] X. Lyu et al. "An investigation on performance enhancement for KF post deposition treated CIGS solar cells fabricated by sputtering CIGS quaternary targets". In: *Vacuum* 151 (2018), pp. 233–236. DOI: https://doi.org/10.1016/j.vacuum.2018.02.023.

[72] J. Larsen et al. "Surface modification through air annealing Cu2ZnSn(S,Se)4 absorbers". In: *Thin Solid Films* (2016). DOI: 10.1016/j.tsf.2016.08.030.

APPENDIX A

Elements Detected with SIMS

Table A.1: Overview of experimental details employed in all SIMS depth profiles presented in this thesis.

Element:	**Primary beam:**	**Species detected:**	**Included in Fig.:**
S	5 keV Cs^+	$^{32}S^{133}Cs$	5.11a, 5.3d, 5.5a
Ti	10 keV O_2^+	^{48}Ti	5.11b, 5.15b
Cu	10 keV O_2^+	^{63}Cu	5.12, 5.15a, 5.13
Cu	5 keV Cs^+	$^{63}Cu^{133}Cs$	5.3d
Zn	10 keV O_2^+	^{64}Zn	5.11c, 5.15c
Zn	5 keV Cs^+	$^{64}Zn^{133}Cs$	5.3d
Ge	5 keV Cs^+	$^{74}Ge^{133}Cs$	5.3d, 5.5a
Mo	5 keV Cs^+	$^{98}Mo^{133}Cs$	5.3d, 5.5a
Sn	5 keV Cs^+	$^{120}Sn^{133}Cs$	5.3d, 5.5a
Sn	10 keV O_2^+	^{120}Sn	5.11d

APPENDIX B

CZTS Synthesis in Tandem Fabrication

Table B.1: Overview of different parameters employed in the synthesis of CZTS absorbers on Si substrates with TOPCon structure.

Thickness:	Temperature:	Duration:	Glass:	Result:
500 nm	580 °C	13 minutes	Yes	Peeling
500 nm	580 °C	13 minutes	No	Peeling
500 nm	580 °C	1 minute	Yes	Peeling
500 nm	580 °C	1 minute	No	Peeling
500 nm	540 °C	13 minutes	Yes	Peeling
500 nm	540 °C	13 minutes	No	Peeling
300 nm	580 °C	13 minutes	No	Adhesion
300 nm	580 °C	1 minute	No	Adhesion